

UNIVERSITY OF CAMBRIDGE
DEPARTMENT OF CHEMISTRY

Microscopic Forces and Flows due to Temperature Gradients

This dissertation is submitted for the degree of Doctor of Philosophy

December 2017

Raman S. Ganti

Churchill College

Preface

The work described in this dissertation was carried out by the author in the Department of Chemistry at the University of Cambridge between January 2014 and December 2017 under the supervision of Professor Daan Frenkel.

This dissertation is the result of my own work and includes nothing which is the outcome of work done in collaboration except as declared in the Preface and specified in the text.

It is not substantially the same as any that I have submitted, or, is being concurrently submitted for a degree or diploma or other qualification at the University of Cambridge or any other University or similar institution except as declared in the Preface and specified in the text. I further state that no substantial part of my dissertation has already been submitted, or, is being concurrently submitted for any such degree, diploma or other qualification at the University of Cambridge or any other University or similar institution except as declared in the Preface and specified in the text.

It does not exceed the prescribed word limit for the relevant Degree Committee.

Raman Ganti, December 2017

Acknowledgements

This has been the most difficult experience of my entire life. I can say that with a high degree of certainty. Solving this problem or at least getting close required an immense amount of emotional and professional support, which altogether mean that there are a lot of people I need to acknowledge.

I would like to express my deepest gratitude to my supervisor Professor Daan Frenkel and my collaborator Yawei Liu for helping me to focus on the important aspects of this problem. There are too many rabbit holes. Finding the right things to be confused about is key. I gratefully acknowledge numerous discussions with Lydéric Bocquet, Mike Cates, Patrick Warren, Ignacio Pagonabarraga, Benjamin Rotenberg, and Alpha Lee. I especially want to thank Peter Wirnsberger for consistently helpful discussions, error analysis code, crucial tips on temperature gradient algorithms, and always pushing me to be as clear as possible. I am grateful to the Raymond and Beverly Sackler Foundation for funding this effort.

I want to thank my good friend Matic, for being a constant positive force and for pearls of wisdom regarding software development. Success is directly correlated with a reduction in the probability of making a mistake. Without the right computational tools, I would be nowhere.

To the Selwyn gang, I want to thank Da Da, Lukas, Oliver, and Will for showing me how to have fun instead of listening to me complain for hours. I also want to thank Julian and Nick for helping me navigate the pits of PhD life. To the rebels at Churchill, I want to thank Marija, Chiara, and Nadi for ad hoc therapy sessions and giving me much needed respite from the stress tensor. There are of course so many other friends who have helped me along the way. You know who you are.

To my partner Rashmi Potato, who has watched me grow and witnessed every moment of failure and success in this journey, thank you for never giving up on me even when I already had. Finally, to my parents and sister for making believe that I can do anything.

Microscopic Forces and Flows due to Temperature Gradients

Raman S. Ganti

Abstract

Nano-scale fluid flow is unlike transport on the macro-scale. Pressure gradients typically dominate effects on a large scale while thermal gradients contribute negligibly to the motion of fluid. The situation entirely reverses on the nano-scale. At a microscopic level, flows induced by thermal gradients are caused by forces that act on atoms or molecules near an interface. These thermo-osmotic forces cannot, at present, be derived analytically or measured experimentally.

Clearly, it would be useful to calculate these forces via molecular simulations, but direct approaches fail because in the steady-state, the average force per particle vanishes, as the thermo-osmotic force is balanced by a gradient in shear stress. In our journey to indirectly calculate the osmotic force, we met another unknown in the field of molecular theory at interfaces: the microscopic pressure tensor. The latter is an open problem since the microscopic pressure near an interface is not uniquely defined.

Using local thermodynamics theories, we relate the thermo-osmotic force to the gradient of the microscopic pressure tensor. Yet, because the pressure is not uniquely defined, we arrive at multiple answers for the thermo-osmotic force, where at most one can be correct.

To resolve the latter puzzle, we develop a direct, non-equilibrium simulation protocol to measure the thermo-osmotic force, whereby a thermal gradient is imposed and the osmotic force is measured by eliminating the shear force. Surprisingly, we find that the osmotic force cannot be derived from the gradient of well-known microscopic pressure expressions. We, therefore, derive a thermodynamic expression that gets close.

In this work, we report the first, direct calculation of the thermo-osmotic force while simultaneously showing that standard microscopic pressure expressions fail to predict pressure gradients.

Contents

1	Introduction	7
1.1	Theoretical Background	9
1.1.1	Irreversible Thermodynamics	9
1.1.2	Derjaguin	12
1.1.3	Levich	17
1.2	State of the Art	19
1.2.1	Past Experimental Work	19
1.2.2	Recent Experimental Work	23
1.2.3	Connections to Thermophoresis and Soret Effect	25
1.2.4	Molecular Simulation Studies	29
1.3	Thesis Structure	30
2	Developing Theoretical Framework	33
2.1	Gibbs Duhem Relation	33
2.2	Gibbs Adsorption Relation	37
3	Microscopic Expressions	42
3.1	Atomic Pressure Expressions	42
3.1.1	Irving-Kirkwood	42
3.1.2	Gauge Variance	47
3.1.3	Virial	52
3.2	Invariance of Surface Tension	56
3.3	Atomic Heat Current Expressions	58
4	Computational Tools	61
4.1	Velocity Verlet	61
4.2	Nosé Hoover Thermostat	63
4.3	Temperature Gradient Algorithms	65
4.3.1	RNEMD	66
4.3.2	HEX	67
4.3.3	Temperature Rescale	68

5	Indirect Approaches	70
5.1	Stress Gradient Method	70
5.2	Thermodynamic Method	75
5.3	Derjaguin Method	78
5.4	Results	80
6	Direct Approaches	97
6.1	Non-equilibrium Method	97
6.2	Results	102
6.2.1	Structured Walls	102
6.2.2	Wall Stress	105
6.2.3	Flat Wall	107
7	Surface Tension Gradients	118
7.1	Kirkwood & Buff	118
7.2	Results	120
8	Conclusion	124
8.1	Future Work	126
9	Appendix	127
9.1	Entropy Production from the Second Law	127
9.2	Mass Balance	132
9.3	Irving-Kirkwood Computational Expression	133
9.4	Microscopic Flows due to Chemical Potential Gradients	134
9.4.1	Diffusio-osmosis	135
9.4.2	Solutal Marangoni Effect	141

Chapter 1

Introduction

God made the bulk; surfaces
were invented by the devil.

Wolfgang Pauli

Nanotechnology is not just conventional technology scaled down to the nano-scale. The reason is that processes that are relatively unimportant on macroscopic scales may become dominant on the nano-scale. Case in point are phoretic flows: the movement of fluids under the influence of gradients of thermodynamic quantities such as temperature or chemical potential. On a macroscopic scale, the application of a pressure gradient or a body force is the most efficient way to move fluid through a tube. The resulting flux is proportional to the fourth power of the tube diameter. However, on a sub-micron scale, phoretic flows tend to become important because the resulting volumetric flow rates scale as the square of the tube diameter. Hence, for many problems, be they technological (e.g. nano-fluidics) or natural (e.g. fluid flow through porous networks or gels), it is becoming increasingly important to be able to predict phoretic flows.

A key feature of phoretic flows is that they are driven by forces that

only act on those parts of the fluid that interact with the confining surfaces. The range of the fluid-wall interactions is typically in the nano-meter regime, except in the case of electrolytes in contact with charged surfaces, in which case the interaction layers may have thicknesses ranging from nanometers to microns. Here we will be considering thermo-osmotic flows in non-polar fluids near a wall. For such systems, the thermo-osmotic force driving the flow is typically confined to an interfacial layer with a thickness of a few molecular diameters. The effect is therefore described as the induced slippage of fluid along an interface, due to an external temperature gradient.

Thermo-osmotic flows have been known for well over a century [39, 2], but the relevance of this phenomenon is increasing as more experiments probe transport on the nano-scale. Moreover, there is increasing evidence that large temperature gradients may exist inside eukaryotic cells [8], which is also an environment full of interfaces.

On a macroscopic scale, thermo-osmotic effects play a significant role in thermophoresis [1, 54, 75], thermodiffusion [16, 72], and the propulsion of active matter [26, 9]. Phoretic motion of colloids is driven by thermo-osmotic flows in the microscopic boundary region, where properties of the solvent are influenced by interactions with the surface (or interface) [1, 54, 75].

Clearly, it would be useful to predict thermo-osmotic slip on the basis of a molecular description of the solid-liquid interface. However, in practice this is not simple because much of the existing theoretical framework is couched in terms that assume the validity of a local continuum theory (e.g. Debye-Hückel plus the (Navier-)Stokes equation) and make drastic assumptions about the excess enthalpy density and viscosity near the surface [5]. Yet, crucially, near an interface, a continuum description of the structure or dynamics of a liquid is not allowed. More ominously, the definition of the

stress in a liquid is not unique. This non-uniqueness has no effect on the computed value of, say, the liquid-liquid surface tension [65], but it could affect the prediction of phoretic flows, where the *local* value of the stress gradient is what drives the flow. In this work, we consider this problem and explore novel ‘microscopic’ methods to predict thermo-osmotic forces and flows in a simple model system.

1.1 Theoretical Background

1.1.1 Irreversible Thermodynamics

To treat the problem of transport induced by thermal gradients, it is crucial to establish the mathematical formalism that has been conventionally used to describe non-equilibrium processes in the linear regime. Irreversible thermodynamics treats intensive state parameters such as temperature, pressure, and chemical potential as field variables. The critical step is starting with entropy balance and the second law. This must consider the entropy flux into the system and a source term that arises from irreversible responses due to gradients of the state variables. Following this line of reasoning gives an expression for the total entropy production in the system.

Using mass, energy, and entropy balance laws, De Groot and Mazur [11] derive the rate of entropy production due to all possible thermodynamic forces and chemical affinities (see Appendix 9.1). Repeated indices are summed

$$\begin{aligned}
 T\rho\dot{s} = & -\mathbf{J}_q \cdot \frac{\nabla T}{T} - \sum_{k=1}^n \mathbf{J}_k \cdot \left(T\nabla \left(\frac{\mu_k}{T} \right) - \mathbf{F}_k \right) \\
 & - \sum_{\alpha \neq \beta} \Pi^{\alpha\beta} \nabla^\beta v^\alpha - \Pi \nabla \cdot \mathbf{v} - \sum_{k=1}^n \sum_{j=1}^r \nu_{kj} \mu_k J_j \geq 0
 \end{aligned} \tag{1.1}$$

where \mathbf{J}_q is the heat flux, \mathbf{J}_k is the diffusive flux of species k , \mathbf{F}_k is an external force on k e.g. due to an electric field, $\Pi^{\alpha\beta}$ is the viscous stress tensor, $\nu_{kj}J_j$ is the production of k per unit volume in the j^{th} chemical reaction, and μ_k is the chemical potential. Note that bulk and shear viscosity contributions are separated. For an incompressible fluid, the term $-\Pi\nabla\cdot\mathbf{v}$ vanishes.

The form of Eq. (1.1) is fixed by the additional constraints that the entropy production is Galileian invariant and must vanish in equilibrium. It is clear that Eq. (1.1) satisfies these constraints. From Eq. (1.1), we can clearly see all possible sources of entropy production. The first term is heat conduction, second is diffusion of different species, third and fourth are viscous flow, and fifth is chemical reactions. It is also worth noting that the entropy production is a sum of the products of fluxes and thermodynamic forces.

Upon closer examination of the second term, De Groot and Mazur note through chain rule that the diffusive flux of different species also couples to gradients in temperature. Using the thermodynamic relation

$$Td\left(\frac{\mu_k}{T}\right) = (d\mu_k)_T - \frac{h_k}{T}dT \quad (1.2)$$

where the subscript T means the differential is taken at constant T and h_k is the partial specific enthalpy of species k , we can introduce the measurable heat flux \mathbf{J}'_q

$$\mathbf{J}'_q = \mathbf{J}_q - \sum_{k=1}^n h_k \mathbf{J}_k. \quad (1.3)$$

The difference between \mathbf{J}'_q and \mathbf{J}_q is transfer of heat due to diffusion. \mathbf{J}'_q is described as irreversible heat transfer since it is the net flux of heat that contributes to the production of entropy within the system (see Appendix 9.1). Alternatively, it is called the measurable heat flux as it is the transferred heat content that can be measured via calorimetry. Substitution of Eq. (1.3)

into Eq. (1.1) gives

$$\begin{aligned}
T\rho\dot{s} &= -\mathbf{J}'_q \cdot \frac{\nabla T}{T} - \sum_{k=1}^n \mathbf{J}_k \cdot ((\nabla\mu_k)_T - \mathbf{F}_k) \\
&\quad - \sum_{\alpha \neq \beta} \Pi^{\alpha\beta} \nabla^\beta v^\alpha - \Pi \nabla \cdot \mathbf{v} - \sum_{k=1}^n \sum_{j=1}^r \nu_{kj} \mu_k J_j \geq 0
\end{aligned} \tag{1.4}$$

where now, the contributions from different thermodynamic forces can be neatly decoupled.

Yet, the entropy production alone is not sufficient since the relationship between fluxes and thermodynamic forces is unknown. Therefore, an additional set of phenomenological equations that relate fluxes to forces must be included. Examples include Fick's Law of diffusion, Fourier's Law of thermal conductivity, and Ohm's Law of electrical conductivity. The phenomenological equations that supplement Eq. (1.4) are given by

$$\mathbf{J}'_q = -L_{qq} \frac{\nabla T}{T} - \sum_{k=1}^n L_{qk} ((\nabla\mu_k)_T - \mathbf{F}_k) \tag{1.5}$$

$$\mathbf{J}_i = -L_{iq} \frac{\nabla T}{T} - \sum_{k=1}^n L_{ik} ((\nabla\mu_k)_T - \mathbf{F}_k) \tag{1.6}$$

$$(\Pi^{\alpha\beta})_{\alpha \neq \beta} = -L(\nabla^\beta v^\alpha)_{\alpha \neq \beta} \tag{1.7}$$

$$\Pi = -l_{vv} \nabla \cdot \mathbf{v} - \sum_{m=1}^r l_{vm} \sum_{k=1}^n \nu_{km} \mu_k \tag{1.8}$$

$$J_j = -l_{jv} \nabla \cdot \mathbf{v} - \sum_{m=1}^r l_{jm} \sum_{k=1}^n \nu_{km} \mu_k. \tag{1.9}$$

The coefficients L_{qq} , L_{iq} , L_{qk} , L_{ik} are scalar quantities that describe the vectorial phenomena of heat conduction, diffusion, and cross-effects. L is the shear viscosity, which for an isotropic fluid is the same in all directions. Lastly, l_{vv} , l_{vm} , l_{jv} , l_{jm} are scalar coefficients that describe scalar processes

of bulk viscosity, chemical reactions, and their cross-effects to linear order. Due to the Curie symmetry principle, fluxes and thermodynamic forces of different tensorial character do not couple for an isotropic system. There are, for example, no cross-coefficients that relate chemical affinity to heat or mass transport.

The symmetry principle allows Eq. (1.4) to be split into three contributions which are separately positive definite

$$T\rho\dot{s}_0 = -\Pi\nabla \cdot \mathbf{v} - \sum_{k=1}^n \sum_{j=1}^r \nu_{kj} \mu_k J_j \geq 0 \quad (1.10)$$

$$T\rho\dot{s}_1 = -\mathbf{J}'_q \cdot \frac{\nabla T}{T} - \sum_{k=1}^n \mathbf{J}_k \cdot ((\nabla \mu_k)_T - \mathbf{F}_k) \geq 0 \quad (1.11)$$

$$T\rho\dot{s}_2 = - \sum_{\alpha \neq \beta} \Pi^{\alpha\beta} \nabla^\beta v^\alpha \geq 0. \quad (1.12)$$

In this work, we are primarily interested in understanding cross-effects, specifically Eq. (1.6), that relates mass diffusion to a temperature gradient. Such cross-effects have special symmetry properties. The Onsager-Casimir reciprocity theorem proves that $L_{qk} = (L_{iq})_{i=k}$, $L_{ik} = L_{ki}$, $l_{vm} = (l_{jv})_{j=m}$, and $l_{jm} = l_{mj}$, thereby reducing the number of independent unknowns. Once the thermodynamic forces are known, the relevant terms can be retained in Eq. (1.4) and Eq. (1.5)-Eq. (1.9). As we will show in the next section, the reciprocal relations prove to be useful in deriving an expression for thermo-osmotic slip.

1.1.2 Derjaguin

The ‘classical’ approach to predict thermo-osmotic slippage is based on Onsager’s reciprocity relations. Derjaguin [14] used Onsager’s theory of Lin-

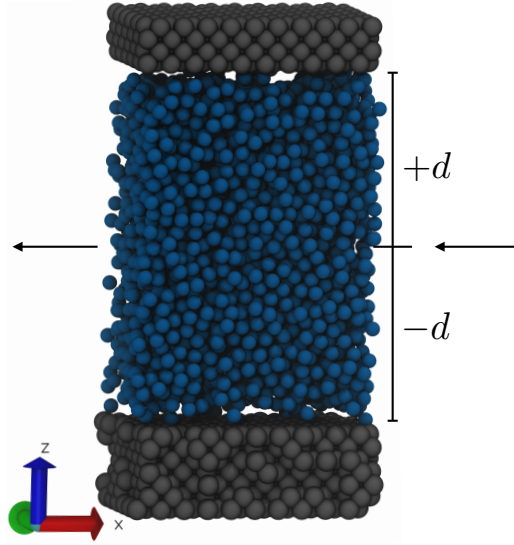


Figure 1.1: Fluid (blue) interacting with solid walls (grey) in a slit pore. $2d$ is the gap width.

ear Non-Equilibrium Thermodynamics (LNET) to derive an expression for thermo-osmotic slip.

Consider the slit pore as depicted in Fig. 1.1. A pressure and temperature gradient is maintained across the slit. Fluid flows in the $-x$ direction as depicted by the arrows. For a single-component fluid, the rate of entropy production due to vectorial phenomena can be written as

$$T\rho\dot{s} = -v_x\nabla P - J_x^{q'}\frac{\nabla T}{T} \quad (1.13)$$

where v_x is the fluid velocity (m/s) and $J_x^{q'}$ is the irreversible heat flux ($J/(m^2 \cdot s)$). Derjaguin considers ∇P as the conjugate force to the mass flux, but we can easily recover Eq. (1.11). Using the Gibbs-Duhem relation at constant temperature,

$$\nabla P = \rho\nabla_T\mu \quad (1.14)$$

Eq. (1.13) can be re-expressed as

$$T\rho\dot{s} = -J_x\nabla_T\mu - J_x^q\frac{\nabla T}{T}. \quad (1.15)$$

This is equivalent to Eq. (1.11) for a single-component system in the absence of external forces.

Eq. (1.13) implies the following phenomenological equations:

$$v_x = -\beta_{11}\nabla P - \beta_{12}\frac{\nabla T}{T} \quad (1.16)$$

$$J_x^q = -\beta_{21}\nabla P - \beta_{22}\frac{\nabla T}{T} \quad (1.17)$$

where β_{11} is the mass diffusion coefficient that describes isothermal flow due to the pressure gradient and β_{22}/T is the thermal conductivity of the fluid. The coefficient of interest here is clearly β_{12} , which describes mass transport induced by the thermal gradient. Due to Onsager's reciprocity theorem, the problem can be solved by considering instead the equivalent β_{21} , the coefficient describing heat diffusion due to hydrodynamic flow.

Consider the isothermal, irreversible heat flux across the pore in Fig. 1.1

$$J_x^q = J_x^q - h^B v_x = \frac{1}{2d} \int_{-d}^{+d} \Delta h(z) v_x(z) dz \quad (1.18)$$

where h^B is the bulk enthalpy density and $\Delta h(z)$ is the excess near the surface. Subtracting the diffusive contribution to the total heat transfer (Eq. (1.3)), J_x^q , leaves only the excess heat flux in the boundary layers. An expression for v_x due to ∇P can be derived starting with the Stokes equation while assuming the viscosity η is constant in the boundary layers,

$$\eta \frac{\partial^2 v_x}{\partial z^2} = \frac{\partial P}{\partial x}. \quad (1.19)$$

Since the pressure gradient is independent of z and $\frac{\partial v_x(z)}{\partial z} = 0$ at $z = 0$, integrating once gives

$$\eta \int_z^d \frac{\partial v_x}{\partial z'} dz' = \int_z^d z' \frac{\partial P}{\partial x} dz'. \quad (1.20)$$

Assuming no surface slip i.e. $v_x(z = d) = 0$, the expression can be integrated again to give

$$v_x(z) = -\frac{1}{2\eta} \frac{\partial P}{\partial x} (d^2 - z^2). \quad (1.21)$$

If we assume a linear velocity profile in the thin boundary layer ($\delta \ll d$) where the enthalpy is in excess, Eq. (1.21) can be expanded about the point $z = -d$ to give

$$v_x(z) = -\frac{1}{\eta} \frac{\partial P}{\partial x} d(z + d) + O(z^2). \quad (1.22)$$

Keeping the term linear in z and redefining z as the distance to the wall gives

$$v_x(z) = -\frac{dz}{\eta} \nabla P. \quad (1.23)$$

Substituting Eq. (1.23) into Eq. (1.18) and considering that only the boundary regions contribute to the integral, the excess heat current can be rewritten as

$$J_x^{q'} = -\frac{1}{\eta} \int_0^\delta \Delta h(z) z dz \nabla P \quad (1.24)$$

where $\Delta h(z)$ is the excess enthalpy density at a height z above the surface.

Referring back to the phenomenological expressions (Eq. (1.16)-Eq. (1.17)),

$$\beta_{12} = \beta_{21} = - \left(\frac{J_x^q}{\nabla P} \right)_T \quad (1.25)$$

where β_{21} is typically referred to as the ‘mechano-caloric’ coefficient and β_{12} is the ‘thermo-osmotic’ slip coefficient. Using Eq. (1.16), Eq. (1.24), and Eq. (1.25), the expression for the thermo-osmotic slip velocity is given by

$$v_s = -\frac{1}{\eta} \int_0^\delta \Delta h(z) z \, dz \frac{\nabla T}{T} \quad (1.26)$$

where δ is the extent of the thin boundary region with altered enthalpy. It should be noted that Derjaguin in his original derivation missed the factor of 1/2 in his expression for Poiseuille flow (Eq. (1.21)) leading to an error that has been propagated in numerous works [1, 52, 54, 56]. The difficulty with Eq. (1.26) is that there is a great deal of ambiguity in the microscopic definition of the local excess enthalpy $\Delta h(z)$, a quantity that is also not easy to probe in experiments [1] (see Chapter 1.2.1).

The key motivation for our work is that while a continuum approximation to Eq. (1.26) may be sufficient for interaction lengths on the order of tens of nanometers, it does not work for atomic or molecular liquids that do not contain free charges. Rather, the excess enthalpy density $\Delta h(z)$ is a function of the solvent polarity [56], liquid structure in the boundary layer [5], temperature, and pressure. Additionally, the viscosity η can vary dramatically near a (structured) surface. Our approach circumvents these issues: we argue that the numerical tools that we use can be applied to realistic models that cannot be described using continuum approaches.

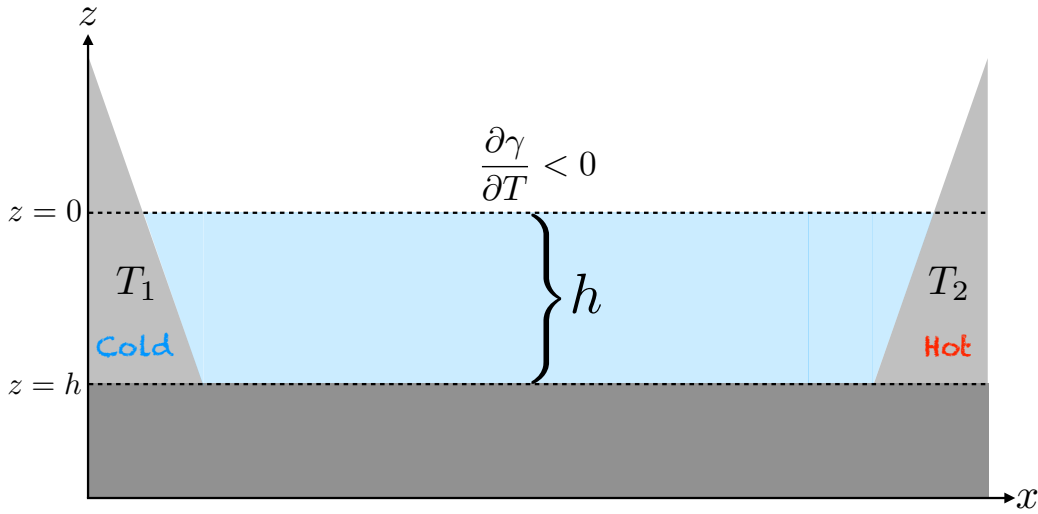


Figure 1.2: Schematic showing the vessel in Levich’s example. The fluid-air interface is located at $z = 0$ and the bottom of the pan is at $z = h$.

1.1.3 Levich

There is an intimate connection between thermo-osmosis and the thermo-capillary effect. Thermo-capillary motion was first described by Levich [38] as movement of liquid due to a surface tension gradient.

Consider as shown in Fig. 1.2 a liquid poured into a shallow pan of depth h with boundary walls kept at temperatures T_1 and T_2 where $T_2 > T_1$. Due to the thermal gradient along the fluid-air interface, the surface tension γ will vary. The resulting surface tension gradient will induce thermo-capillary convection in the fluid. If the diameter of the liquid surface D is large compared to its depth h , the Bond number, $\text{Bo} = \Delta\rho g D h / \Delta\gamma$ where $\Delta\rho = \rho_{\text{fluid}} - \rho_{\text{air}}$, will be much less than one and surface tension forces will be significant in comparison to gravitational forces. Any usual convective motion is assumed to be negligible in comparison to thermo-capillary convection.

The liquid surface is located at $z = 0$ and the bottom of the pan is at $z = h$. Typically, surface tension is a decreasing function of temperature.

Levich therefore assumes that the surface tension attains a maximum value at the colder wall and decreases linearly toward the warmer wall. Assuming also that there are no temperature or chemical potential gradients in z and no convection due to heating of the liquid, there can be no forces or flow in the z direction. Stokes' equation then simplifies to

$$\eta \left(\frac{\partial^2 v_x(z)}{\partial z^2} + \frac{\partial^2 v_x(z)}{\partial x^2} \right) = \left(\frac{\partial P}{\partial x} \right). \quad (1.27)$$

Once again, since the pan depth is small in comparison to its other dimensions, the first term in the left-hand side of Eq. (1.27) will dominate. For the same reasons, it may be assumed that the pressure is also not a function of z . Therefore, Eq. (1.27) can be re-expressed as

$$\eta \left(\frac{\partial^2 v_x(z)}{\partial z^2} \right) = \left(\frac{\partial P(x)}{\partial x} \right) \quad (1.28)$$

where pressure is only a function of x .

Because the system is enclosed with walls, flow of liquid at the surface due to the surface tension gradient is accompanied by flow in the opposite direction in the bulk. The continuity equation is then given by

$$\int_0^h v_x dz = 0. \quad (1.29)$$

With this last piece of information, it is possible to write the boundary conditions for fluid motion in the vessel. At the bottom of the vessel, the liquid velocity is given by

$$(v_x)_{z=h} = 0. \quad (1.30)$$

After fluid motion sets in, a viscous shear stress from the pan balances the

surface tension gradient

$$\eta \left(\frac{\partial v_x}{\partial z} \right)_{z=0} = \frac{\partial \gamma}{\partial T} \nabla T. \quad (1.31)$$

Integrating Eq. (1.28) with the above boundary conditions gives the thermo-capillary flow profile in the vessel

$$v_x(z) = \frac{1}{\eta} \left(\frac{\partial \gamma}{\partial x} \right) (h - z) - \frac{1}{2\eta} \left(\frac{\partial P}{\partial x} \right) (h^2 - z^2). \quad (1.32)$$

Levich's macroscopic treatment considers the surface tension gradient as independent of z . We will show in Chapter 2.2 that $\partial \gamma / \partial x$ is related to the thermo-osmotic force.

1.2 State of the Art

1.2.1 Past Experimental Work

Thermo-osmosis was first observed more than a century ago by Lippmann [39] and Aubert [2] while studying the passage of water through gelatin and pig's bladder. Because the magnitude of flow depended on water-soluble electrolytes within the membrane, the effect was thought to be electrical in origin. Denbigh [12, 13] offered a theoretical treatment on thermo-osmosis of gases. In his formulation, the flow of gas due to the thermal gradient leads to a pressure difference across the membrane which stops flow.

Dividing the phenomenological equations (Eq. (1.16)) at $\nabla T = 0$, he defined the heat of transport in the membrane

$$Q_m^* = \frac{\beta_{21}}{\beta_{11}} - H_m \quad (1.33)$$

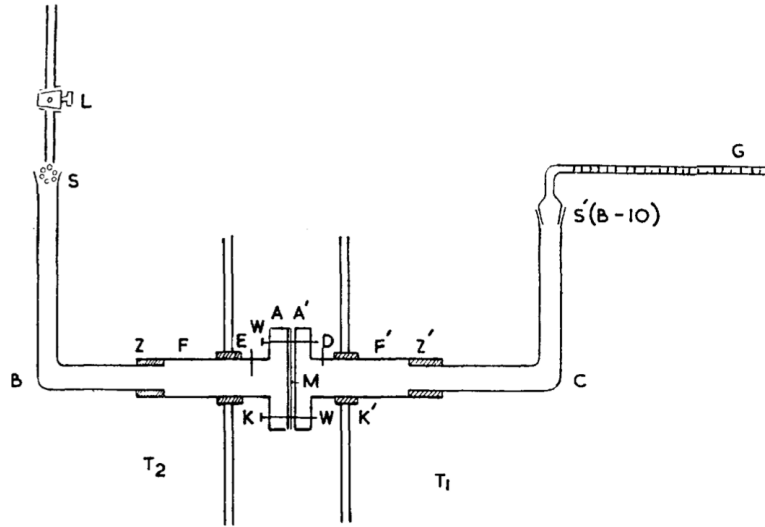


FIG. 1.—Apparatus used for the study of thermo-osmosis.

A, A', ebonite disc; B, C, Pyrex tubes; D, E, thermocouples; F, F', brass tubes; G, Pyrex capillary; K, K', rubber corks; L, stop-cock; M, membrane; S, S', standard joints; Z, Z', dental cement joints; T₁, T₂, thermostats; and W, winding screw.

Figure 1.3: Early experimental setup to measure thermo-osmosis through cellophane membranes depicted in Ref. [57].

where H_m is the partial molar enthalpy of the dissolved gas in the membrane. Q_m^* is, therefore, the amount of transported energy that exceeds the enthalpy of the gas. This quantity is related to the measurable heat flux given by Eq. (1.3). He correctly noted that Q_m^* is the quantity characterizing thermal diffusion across the membrane. The heat of transport can be equivalently given by setting $v_x = 0$ in Eq. (1.16)

$$Q_m^* = \frac{\beta_{12}}{\beta_{11}} = -T \left(\frac{\Delta P}{\Delta T} \right)_{v_x=0} \quad (1.34)$$

where ΔP is the thermo-osmotic pressure difference that stops flow. Eq. (1.34) expresses the thermo-mechanical effect, where a stationary pressure difference arises as a result of a temperature gradient [14].

Since Denbigh’s introduction of Q_m^* , there has been numerous experimental attempts to measure the heat of transport. Rastogi et. al [57] used the experimental setup shown in Fig. 1.3 to measure the thermo-osmosis coefficient of water through a cellophane membrane. The glass tubes (B, C) contain water and the cellophane was fixed between ebonite discs (A, A’). The difference in temperature was measured by thermocouples (D, E) passing through the brass tubes (F, F’) near the membrane. Water level on both sides of the membrane was kept the same via titration (L) so that $\nabla P = 0$. Fluid velocity was determined by measuring the displacement of the water column. Using the fluid velocity and temperature difference, the thermo-osmosis coefficient could be determined via Eq. (1.16).

To validate their findings [58, 59], they measured the heat of transport via Eq. (1.34) by allowing a pressure difference to develop on both sides of the membrane so that flow vanishes in the steady state. For temperatures between $319 - 327^\circ K$, they report heat of transport values ranging from $0.088 - 0.137$ cal/mol with no clear dependence on temperature. Haase et. al [29] concurrently carried out calculations of thermo-osmotic water flow through cellophane membranes. For temperatures between $284 - 350^\circ K$, they report Q_m^* values ranging from 2.43 to -0.46 cal/mol where Q_m^* decreases as a function of temperature.

Dariel and Kedem [10] pointed out that the latter studies failed to account for the thermal conductivity of the membranes, assuming therefore that the temperature difference between the bulk phases (ΔT_b) is equivalent to the actual difference across the membrane (ΔT_m). Exploiting the relationship between volumetric flow and membrane thickness, ΔT_m could be determined. For temperatures between $283 - 328^\circ K$, they measured values of Q_m^* for water across cellulose acetate membranes. Their values for Q_m^* range from 370

to 500 cal/mol, which was three orders of magnitude higher than previous studies and showed the opposite dependence of Q_m^* on temperature. While failure to correct for the actual temperature difference could account for a factor of ten discrepancy, the additional two orders of magnitude could not be explained.

Vink and Chishti [69] used magnetic stirrers to eliminate thermal gradients in the bulk liquid compartments so that the temperature difference across the membrane could be more accurately estimated. Due to thermal conductivity of the membrane, the temperature of stationary liquid layers near the membrane surfaces may be different from the bulk, an effect known as temperature polarization. Magnetic stirrers reduce thickness of the liquid layers causing them to thermalize with the bulk. The latter procedure improves estimation of the actual temperature difference across the membrane. Vink and Chishti measure heat of transport values for water across cellophane that are twice those reported by Haase [69]. The discrepancy, they explain, may be due to differences in the structural density of the membranes. In comparison with Dariel and Kedem's anomalous values, they pointed out that the latter authors do not measure the thermo-osmotic pressure directly and therefore their measurements cannot be trusted.

Mengual et al [45, 46] carried out a series of experiments to measure thermo-osmosis of water through cellulose acetate membranes. Using Vink and Chishti's method of magnetic stirring to reduce the effects of temperature polarization, they measured the thermo-osmotic permeability coefficient B , which is related to the heat of transport via $B = \rho\beta_{11}Q^*/T$, where ρ is the fluid density. They constructed three membranes of differing thicknesses by dissolving 200, 250, and 300 mg of cellulose acetate in 60 cm³ of acetone. Measurements of B increased with the magnetic stirring rate. By

extrapolating to infinite stirring rates, they introduced a correction factor to account for temperature polarization effects. The B value for the thinnest membrane was on the order of 10^{-10} mole/(m sec K) and increasing to 10^{-9} mole/(m sec K) for the thicker ones. Comparing to literature values, Dariel and Kedem [10] obtained values on the order of 10^{-9} mole/(m sec K) for dense cellulose acetate membranes whereas Haase [29] and Rastogi [59] reported values on the order of 10^{-8} and 10^{-6} mole/(m sec K), respectively, for cellophane. Overall, their measurements underestimated the thermo-osmotic permeability with respect to literature values.

Besides transport through cellulose-acetate or cellophane membranes, there have been numerous studies estimating thermo-osmotic flow through porous clay-rich media [17, 66, 28, 67]. Such measurements can improve safety assessments of nuclear-waste repositories in shale layers [7, 50, 27]. Derjaguin and Sidorenkov [15, 14] carried out the earliest experiments of thermo-osmotic water flow through porous glass. In the latter case, the presence of surface charges complicates the story and there is still no consensus on the sign of the thermo-osmosis coefficient [5].

1.2.2 Recent Experimental Work

Bregulla et. al [5] recently attempted to experimentally measure the thermo-osmosis coefficient of water interacting with a Pluronic F-127 coated surface and a glass surface. Pluronic F-127 is a nonionic triblock copolymer containing a hydrophobic block of polypropylene glycol, which attaches to the surface and two hydrophilic blocks of polyethylene glycol, which form an aqueous polymer brush.

Their experimental setup shown in Fig. 1.4 includes heating a 250nm Au nanoparticle fixed to the surface and tracing the flow field by tracking 150

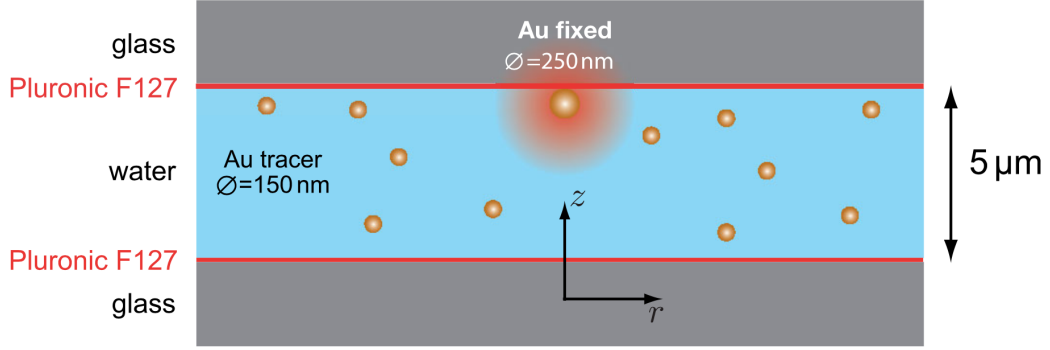


Figure 1.4: Experimental setup from Ref. [5] to measure thermo-osmosis of water in contact with glass and a polymer brush (Pluronic F-127).

nm tracer particles. By extracting the slip velocity from the flow field, they calculated β_{12} (Eq. (1.25)): $-13 \times 10^{-10} \text{ m}^2/\text{s}$ for the water-polymer and $-1.8 \times 10^{-10} \text{ m}^2/\text{s}$ for the water-glass interface.

To validate the experimental measurements, they offered a theoretical estimate of β_{12} . The enthalpy of mixing for PEG is $\Delta H = -0.66 \times 10^{-20} \text{ J/monomer}$. Treating the polymer as a rod of radius b and length d while assuming the excess enthalpy density is constant within an interaction length λ and zero beyond, $\Delta h = \Delta H/2\pi b d \lambda$. Their theoretical approximation for the thermo-osmosis coefficient is given by

$$\beta_{12} \approx \left(\frac{1}{\eta}\right) \left(\frac{\Delta H \lambda}{4\pi b d}\right) \sim -14 \times 10^{-10} \text{ m}^2/\text{s} \quad (1.35)$$

where $b = \lambda$ and $d = 3.5 \text{ \AA}$. For the water-glass interface, they use the Debye-Hückel approximation to estimate $\beta_{12} \sim -10^{-10} \text{ m}^2/\text{s}$.

While the agreement between theoretical estimates and experimental measurements seems impressive, the assumptions in deriving the former are drastic. As we will show in Chapter 5.4, even for a simple solid-liquid interface the excess enthalpy density is not constant within the interaction length.

Moreover, especially in the case of a grafted polymer brush, one would expect the viscosity near the interface to differ significantly with respect to the bulk. In the case of water interacting with glass, Debye-Hückel theory does not account for structuration of the fluid near the interface. It also fails to include the effects of thermal electrostriction $\partial\epsilon/\partial T$.

Aside from the dangerous assumptions built in to their theoretical estimates, the experimental measurements also fail to account for thermophoresis of the tracer particles due to the thermal gradient, which cannot be neglected. Clearly, thermo-osmosis demands robust numerical attention as precise experimental measurement still proves to be difficult.

1.2.3 Connections to Thermophoresis and Soret Effect

Thermo-osmotic slip is intimately related to thermophoresis, the motion of a colloidal particle under the influence of a thermal gradient. Thermophoresis is typically considered in two limiting cases: the Hückel limit and boundary layer approximation [6, 75]. In the Hückel limit, particle-solvent interactions are long-range such that $r \ll \delta$, where r is the colloid radius and δ denotes the interaction range of the colloid with solvent. In the boundary layer approximation, $r \gg \delta$ such that the particle can be treated as a flat surface interacting with the solvent via short range forces. In this case, the temperature gradient induces a local pressure gradient (see Chapter 2.1) that drives thermo-osmotic slip at the colloid surface. For a homogeneous surface, the slip velocity varies with the sign of the polar angle [75]

$$\hat{v}_s(\theta) = v_s \sin \theta \tag{1.36}$$

where v_s is the maximal value at $\theta = \pi/2$ given by Eq. (1.26). Due to momentum conservation, the resulting particle velocity will be opposite to the osmotic flow in the boundary layer. An orientational average of Eq. (1.36) over the colloidal surface gives the thermophoretic velocity [75]

$$u = -\frac{2}{3}v_s. \quad (1.37)$$

Of course, the preceding analysis greatly simplifies thermophoresis in the boundary layer approximation. Derjaguin duly notes that thermophoresis is an open problem due to difficulties involved in correctly taking into account thermal conduction and Brownian motion of small particles [14]. Heat conduction through the particle surface causes the temperature profile around the colloid to change. Thus, for a curved surface, ∇T in Eq. (1.26) will not simply be equal to the externally imposed temperature gradient.

Thermophoresis is closely related to the Soret effect, the motion of many particles suspended in fluid due to a thermal gradient. The total mass flux in such a system can be written as

$$J = -D\nabla c - cD_T\nabla T \quad (1.38)$$

where c is the particle concentration, D is the Brownian diffusion coefficient, and D_T is the thermophoretic mobility given by $-u/\nabla T$. At steady-state, flux due to Brownian diffusion cancels flux due to thermal diffusion such that J vanishes. The Soret coefficient is then given by

$$S_T = \frac{D_T}{D} = -\frac{\nabla c}{c\nabla T}. \quad (1.39)$$

If $S_T > 0$, particles move to the cold region, while the reverse occurs for

$S_T < 0$.

McNab and Meisen conducted the earliest studies of thermophoresis by observing latex spheres suspended in water and n-hexane [44]. They imposed a vertical temperature gradient by trapping a suspension of particles between horizontal parallel disks. The thermophoretic velocity was determined as the difference between the vertical displacement of particles in the thermal field and the Stokes settling velocity [14]. Their measurements showed that the phenomenon is independent of particle size, which is consistent with Eq. (1.37) [1].

Since McNab and Meisen's early work, advances in optical techniques have allowed for more accurate study of thermophoresis. Beam deflection (BD), developed by Giglio and Vendramini [25], involves focusing a laser beam onto the mid-plane of a thin mixture confined between two horizontal plates at different temperatures. Due to the temperature difference, a gradient in the refractive index (dn/dz) builds up in the fluid and the beam is deflected [25]. The angular deflection due to first thermal expansion and then a thermally induced concentration gradient allows for estimation of the Soret coefficient [54].

Piazza and Guarino [53] used BD to study thermal diffusion of charged micelles. Their experiments show that S_T scales as the square of the Debye-Hückel length, deviating from standard electro-kinetic phenomena [42]. Using a micro BD setup, Putnam and Cahill [56] measured D_T for charged polystyrene spheres. Particles with different surface chemistries exhibited a wide range of values for D_T , validating the significance of the excess enthalpy density (Eq. (1.26)) in driving transport.

Iacopini et al. [33, 34] studied the temperature dependence of S_T . They attempted to discern a threshold temperature T^* above which particles drift

to the cold region and below which the reverse motion occurs. From their experiments, the dependence of S_T on temperature could be described by the empirical fitting function

$$S_T(T) = S_T^\infty \left[1 - \exp\left(\frac{T^* - T}{T_0}\right) \right] \quad (1.40)$$

where S_T^∞ is the high- T asymptotic limit and T_0 is the exponential growth rate that determines the strength of temperature effects. The fitting function accurately described a large class of aqueous systems including protein solutions, SDS ionic micelles, and DNA [34].

Recent advances in particle-tracking methods and confocal microscopy have paved the way towards direct visualization of colloidal thermophoresis. Duhr and Braun [18, 19] use laser beam adsorption to induce localized thermal gradients within aqueous micro-fluidic cells. The concentration of fluorescent-dyed particles can be reconstructed from the fluorescence intensity. Because the dye’s emission is temperature dependent, the temperature field around the colloid can be monitored [20]. If particles are sufficiently large such that individual emission can be resolved, measurement of v_T and D_T is possible [54].

The latter “Microscale Thermophoresis” (MST) technique developed by Braun and coworkers has been used to study thermophoresis of DNA [18, 60]. Insights from these experiments have led them to suggest that thermal gradients across porous media may have provided essential non-equilibrium conditions for autonomous molecular evolution [4].

1.2.4 Molecular Simulation Studies

Most molecular simulation studies of thermal transport have dealt with calculating the Soret coefficient of atomic species [61, 62]. Typically, this involves simulating a binary mixture driven to a non-equilibrium steady state by a temperature gradient. At steady state, heat continues to flow while the mass flux stops due to an opposing concentration gradient. For a binary mixture, the Soret coefficient is given by [61]

$$S_T = -\frac{1}{n_1(1-n_1)} \left(\frac{\partial n_1}{\partial x} \right) \left(\frac{\partial T}{\partial x} \right)^{-1}$$

where n_1 is the mole fraction of species 1. For equimolar mixtures the expression reduces to

$$S_T = -4 \left(\frac{\partial n_1}{\partial x} \right) \left(\frac{\partial T}{\partial x} \right)^{-1}.$$

By simulating a temperature gradient with the RNEMD algorithm (see Chapter 4.3.1), Reith and Müller-Plathe compute the temperature and concentration gradients in the steady state and therefore the Soret coefficient for a Lennard-Jones fluid. Römer et al [62] used the Heat-Exchange (HEX) algorithm (see Chapter 4.3.2) to compute the Soret coefficient for alkali halide aqueous solutions ($Na^+/K^+ - Cl^-$).

Thermo-osmotic flow is different from the Soret effect since forces due to the density gradient balance thermodynamic forces due to the temperature gradient in the bulk. Near the surface, the force balance does not remain resulting in a local pressure gradient that drives mass flux (see Chapter 2.1). Direct molecular simulation of thermo-osmosis has practical drawbacks, as a constant temperature gradient is incompatible with the periodic boundary

conditions commonly used in simulations to minimize finite-size effects (see Fig. 6.2). As a result, indirect methods have been pursued.

Han [30] developed a mechanical approach via the microscopic pressure tensor (see Chapter 5.1). Conducting equilibrium simulations at different temperatures, he evaluated the change in transverse pressure near the surface due to the change in temperature ($\partial P_{xx}(z)/\partial T$). Using a bulk viscosity calculation, he integrated $\partial P_{xx}(z)/\partial T$ with the Stokes equation (Eq. (1.28)), while assuming no slip at the surface, and determined the thermo-osmotic slip velocity as a function of the temperature gradient. The primary shortcomings of the latter approach are the macroscopic assumptions of no slip and constant viscosity. Moreover, Han fails to validate the slip calculations with any independent approaches.

1.3 Thesis Structure

The scarcity of molecular simulations suggests that thermo-osmotic flow cannot be computed via standard approaches. In this dissertation, we develop a number of independent techniques to calculate thermo-osmotic forces and flows without making macroscopic hydrodynamic assumptions.

In Chapter 2, we introduce a theoretical framework for thermo-osmosis and thermo-capillary motion based on Local Thermal Equilibrium (LTE) approximations. Using the Gibbs-Duhem relation, we explicitly show that the external temperature gradient induces a local pressure gradient, whose magnitude is directly determined by the excess enthalpy density near the surface. Integrating the local pressure gradient via Stokes equation, we recover Derjaguin's expression for the slip velocity. For a liquid-liquid interface, we use the Gibbs-Adsorption relation to equate the integral of the local pressure

gradient to the surface tension gradient. In doing so, we clearly establish that thermo-osmotic and thermo-capillary flow are driven by the same microscopic forces.

To translate the macroscopic theory presented in Section 1.1.2 and Chapter 2 into microscopic terms, we derive the relevant expressions in Chapter 3. In the process, we show that there are ambiguities in defining the atomic pressure tensor and heat current. As we intend to use these expressions to compute thermo-osmotic forces and flows, we must be cautiously aware of how such ambiguities can affect our predictions.

As a prelude to the simulations presented in the remaining chapters, we briefly describe various molecular simulation techniques in Chapter 4. We introduce standard Molecular Dynamics integration and thermostatting schemes and conclude with algorithms for setting up temperature gradients in molecular systems.

In Chapter 5, we describe the ‘stress gradient’, ‘LTE’, and ‘Derjaguin’ methods for computing thermo-osmotic slip. Using microscopic expressions developed in Chapter 3, we evaluate the local pressure gradient via equilibrium calculations of the transverse pressure. We also offer a molecular expression for local enthalpy in order to determine the thermodynamic driving force. We then apply the mechanical and thermodynamic forces to an equilibrium system and measure the non-equilibrium flow profile. Interestingly, the methods yield different force and flow profiles near the surface, while predicting roughly the same bulk flow velocity. As an independent validation step, we compute the reciprocal ‘mechano-caloric’ coefficient by simulating a pressure gradient and evaluating the excess heat current. The slip velocity determined via the Onsager coefficient agrees well with the velocities predicted by the mechanical and thermodynamic approaches.

We pursue in Chapter 6 a direct route to compute thermo-osmotic forces in order to determine which, if any of the approaches offered in Chapter 5, predicts the correct interfacial forces. By treating the mass M of the fluid particles as a tensor in the Hamiltonian, we can eliminate the balancing shear force in a non-equilibrium simulation and therefore compute the thermo-osmotic force at simple solid-fluid interfaces. We compare the non-equilibrium force measurement with estimates of the thermo-osmotic force based on computing gradients of the microscopic pressure tensor. We find that the thermo-osmotic force as measured in our simulations cannot be derived from the most common microscopic definitions of the pressure tensor. Surprisingly, the thermodynamic force predicted by our local enthalpy expression gets extremely close to the non-equilibrium result.

In Chapter 7, we examine the failure of pressure expressions from a macroscopic perspective. By integrating the thermo-osmotic force profiles predicted by the mechanical and thermodynamic expressions, we evaluate the surface tension gradient. Interestingly, pressure gradients fail to predict the surface tension gradient for structured surfaces. If solid phase contributions to the transverse pressure are removed as is the case with a flat wall or near a de-wetting regime, the problem disappears. Based on these results, we conclude that any hydrodynamic formulation of pressure will fail to predict surface tension gradients since it will incorrectly treat solid surface contributions. As an alternative, we contend that the thermodynamic expression for surface tension gradients derived in Chapter 2 always gives the correct answer.

Finally, in Chapter 8 we summarize our results and compare with related work on microscopic flows due to chemical potential gradients. We end with a brief discussion on avenues for future research in non-equilibrium transport.

Chapter 2

Developing Theoretical Framework

Derjaguin's clever use of the Onsager reciprocal relation does not lend a clear physical explanation for the origin of the thermo-osmotic force. Furthermore, Levich's treatment of thermo-capillary motion gives no expression for the surface tension gradient. To fill in the conceptual gaps regarding thermo-osmotic and thermo-capillary motion, we consider the classical thermodynamic approach to the problem, based on the assumption of Local Thermal Equilibrium (LTE).

2.1 Gibbs Duhem Relation

We note that neither temperature gradients nor, for that matter, chemical potential gradients at constant pressure can exert a net force on a fluid element in a bulk liquid. Mechanical forces in liquids can only be caused by external forces such as gravity or pressure gradients. If a temperature gradient causes flow, it is only because a local pressure gradient is induced.

Consider flow due to a temperature gradient parallel to a hard wall in the $+x$ direction; the z coordinate measures distance perpendicular to the wall. Starting from the Gibbs-Duhem relation for an n -component mixture, we write

$$VdP = \sum_{i=1}^n N_i d\mu_i + SdT \quad (2.1)$$

Dividing through by V and differentiating with respect to x gives the following expression:

$$\frac{\partial P}{\partial x} = \left(\sum_{i=1}^n \rho_i \frac{\partial \mu_i}{\partial T} + \frac{S}{V} \right) \frac{\partial T}{\partial x} \quad (2.2)$$

The Gibbs-Duhem equation makes use of the fact that the system is homogeneous. A stratified system in equilibrium, is homogeneous in the directions parallel to the stratification, but not perpendicular to it. Hence, here and in what follows, the ‘pressure’ P refers to a component of the pressure tensor parallel to the surface (e.g. P_{xx}). In the bulk, the pressure is equalized quickly and the fluid reaches hydrostatic equilibrium.

$$\sum_{i=1}^n \rho_i^B \frac{\partial \mu_i^B}{\partial T^B} = -\frac{S^B}{V} \quad (2.3)$$

where the superscript B denotes bulk quantities. Since the bulk pressure is constant, this leads to the well-known thermodynamic relation,

$$\left(\frac{\partial \mu_i}{\partial T} \right)_P = -s_i \quad (2.4)$$

where s_i is the specific entropy of species i . As before, we can write a similar

expression for the pressure gradient at a position z above the surface:

$$\frac{\partial P_{xx}(z)}{\partial x} = \left(\sum_{i=1}^n \rho_i(z) \frac{\partial \mu_i}{\partial T} + \frac{S(z)}{V} \right) \frac{\partial T}{\partial x} \quad (2.5)$$

Using the assumption of LTE, μ_i and T do not depend on z meaning that $\mu_i(z) = \mu_i^B$ and $T(z) = T^B$. Thus, Eq. (2.5) can be rewritten as

$$\frac{\partial P_{xx}(z)}{\partial x} = \left(- \sum_{i=1}^n \rho_i(z) s_i^B + \sum_{i=1}^n \rho_i(z) s_i(z) \right) \frac{\partial T}{\partial x} \quad (2.6)$$

It may be convenient to write

$$\rho_i(z, x) = \rho_i^B e^{-\beta \Delta \mu_i^{ex}(z, x)} \quad (2.7)$$

Note that while μ_i does not depend on z , the excess chemical potential μ_i^{ex} does indeed depend on z . Eq. (2.6) can therefore be written as

$$\frac{\partial P_{xx}(z)}{\partial x} = \left(\sum_{i=1}^n \rho_i^B e^{-\beta \Delta \mu_i^{ex}(z, x)} [s_i(z) - s_i^B] \right) \frac{\partial T}{\partial x} \quad (2.8)$$

Eq. (2.8) can be simplified by noting that the expression in brackets is the difference between the specific entropy at position z and the bulk specific entropy. Since μ_i and T do not depend on z , $\mu_i = h_i - T s_i$ can be used to rewrite Eq. (2.8) so that the thermo-osmotic force is given by

$$\frac{\partial P_{xx}(z)}{\partial x} = \left(\frac{\sum_{i=1}^n \rho_i^B e^{-\beta \Delta \mu_i^{ex}(z, x)} [h_i(z) - h_i^B]}{T} \right) \frac{\partial T}{\partial x} \quad (2.9)$$

$$= \left(\frac{\Delta h(z)}{T} \right) \frac{\partial T}{\partial x} \quad (2.10)$$

where $\Delta h(z)$ is the excess enthalpy density at a distance z from the surface.

Eq. (2.9) is the key relation in this work. The remainder of this dissertation is concerned with developing numerical methods in order to compute Eq. (2.9) and the resulting flows.

To relate our expression for the thermo-osmotic force to the flow velocity, the Stokes equation given by

$$\eta \left(\frac{\partial^2 v_x(z)}{\partial z^2} \right) = \left(\frac{\partial P_{xx}(x, z)}{\partial x} \right) \quad (2.11)$$

can be integrated twice while assuming $\partial v_x / \partial z = 0$ in the bulk and no slip at the surface to give

$$v_x = -\frac{1}{\eta} \int_0^\infty dz' \int_{z'}^\infty dz \left(\frac{\Delta h(z)}{T} \right) \frac{\partial T}{\partial x} \quad (2.12)$$

far away from the surface. Using partial integration, the expression can be re-written as

$$v_x = -\frac{1}{\eta} \left(\left[z' \int_{z'}^\infty dz \left(\frac{\Delta h(z)}{T} \right) \frac{\partial T}{\partial x} \right]_0^\infty + \int_0^\infty dz' z' \left(\frac{\Delta h(z')}{T} \right) \frac{\partial T}{\partial x} \right) \quad (2.13)$$

which simplifies to give

$$v_x = -\frac{1}{\eta} \int_0^\infty dz z \left(\frac{\Delta h(z)}{T} \right) \frac{\partial T}{\partial x} \quad (2.14)$$

It is important to note here that δ can be substituted for the upper bound of the integral in Eq. (2.14) since $\Delta h(z) = 0$ outside of the boundary region. Doing so recovers Derjaguin's expression (Eq. (1.26)).

The usual definition of the 'slip' velocity is the extrapolated velocity at the interface, where the fluid density approaches zero. For a thin boundary layer, we define slip as the fluid velocity in the bulk just outside the boundary layer. In this way, thermo-osmotic slippage is the velocity of the fluid outside

of the surface interaction length.

The advantage of our LTE approach is that Eq. (2.9) gives a clear relationship between the external temperature gradient and the local pressure gradient that induces slip at the surface. The magnitude of this coupling is determined exclusively by the excess enthalpy density. In principle, a simpler approach to derive Eq. (2.9) would be to note that thermo-osmotic flow can only be induced by a mechanical force such as a pressure gradient [1]. Working backwards via partial integration of Eq. (2.11) gives

$$v_x = -\frac{1}{\eta} \int_0^\infty dz z \frac{\partial P_{xx}(x, z)}{\partial x} \quad (2.15)$$

Comparing with Eq. (1.26), we immediately recover Eq. (2.9). The advantage of the Gibbs-Duhem approach is that it shows how the pressure gradient can be equivalently related to the excess specific entropy. Furthermore, it provides additional insight that the problem can be treated with the LTE approximation.

2.2 Gibbs Adsorption Relation

We can see upon comparing Levich's approach in Chapter 1.1.3 to our derivation of thermo-osmosis in the previous section that the surface tension gradient is directly related to the local pressure gradient. The connection to thermo-capillary motion can be derived through the use of the Gibbs-Duhem and Gibbs-Adsorption relations. Consider two fluid phases meeting at a thin transition zone as shown in Fig. 2.1. While the exact location of the Gibbs dividing surface is arbitrary for a planar interface, we choose it to lie in the transition zone [51]. For a single-component system, the dividing surface is typically chosen at a point where the excess density vanishes. In the system

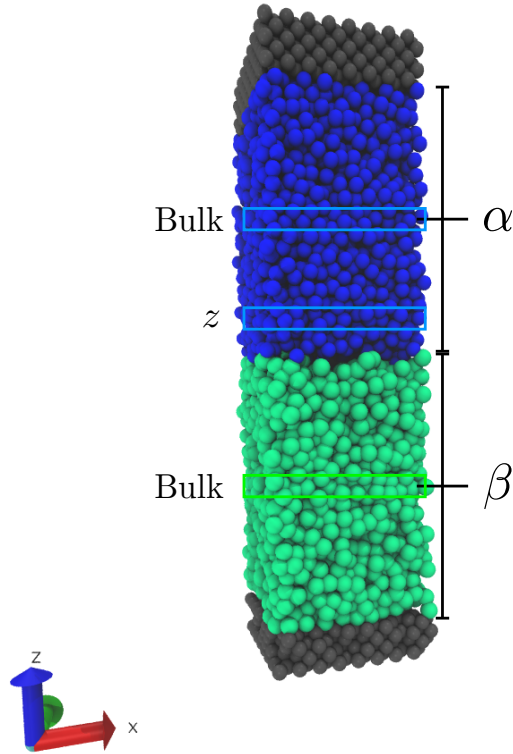


Figure 2.1: Schematic showing two interacting fluid phases α and β . The slab z denotes a volume element in the interfacial region where the number of atoms and entropy is either deficient or in excess with respect to the same size volume element in the bulk phases.

considered here, there is no point at the interface where the latter statement is true [63]. The dividing surface is defined such that $\rho_i^\alpha(z \geq 0) = \rho_i^\alpha$ while below it, $\rho_i^\alpha(z < 0) = 0$; $\rho_i^\beta(z < 0) = \rho_i^\beta$ and $\rho_i^\beta(z \geq 0) = 0$.

We once again write the Gibbs-Duhem relation for the bulk phases α and β . When referring to the bulk, we consider a slab of thickness dz denoted

‘Bulk’ in Fig. 2.1.

$$V^\alpha dP = \sum_i^n N_i^\alpha d\mu_i + S^\alpha dT \quad (2.16)$$

$$V^\beta dP = \sum_i^n N_i^\beta d\mu_i + S^\beta dT \quad (2.17)$$

A temperature gradient in the $+x$ direction leads to an opposing density gradient such that the bulk phases remain hydrostatic.

$$\frac{\partial P}{\partial x} = 0 = \left(\sum_i^n \rho_i^\alpha \left(\frac{\partial \mu_i}{\partial T} \right) + \frac{S^\alpha}{V^\alpha} \right) \left(\frac{\partial T}{\partial x} \right) \quad (2.18)$$

$$\frac{\partial P}{\partial x} = 0 = \left(\sum_i^n \rho_i^\beta \left(\frac{\partial \mu_i}{\partial T} \right) + \frac{S^\beta}{V^\beta} \right) \left(\frac{\partial T}{\partial x} \right) \quad (2.19)$$

Since α and β are in mechanical and thermal equilibrium in the z direction, T and μ_i are independent of z . However, $\partial\mu_i/\partial T$ can change across the dividing surface. Eq. (2.18) and Eq. (2.19) reduce to

$$\left(\frac{\partial \mu_i}{\partial T} \right)_P^\alpha = -s_i^\alpha \quad (2.20)$$

$$\left(\frac{\partial \mu_i}{\partial T} \right)_P^\beta = -s_i^\beta \quad (2.21)$$

We therefore define the bulk specific entropy of species i as

$$s_i^B(z) = \begin{cases} s_i^\beta, & z < 0 \\ s_i^\alpha, & z \geq 0. \end{cases} \quad (2.22)$$

Now, consider the Gibbs-Adsorption relation in its general form

$$Ad\gamma + S^s dT + \sum_i^n N_i^s d\mu_i = 0 \quad (2.23)$$

where the superscript s denotes excess quantities

$$N_i^s = N_i - (N_i^\alpha + N_i^\beta) \quad (2.24)$$

$$S^s = S - (S^\alpha + S^\beta). \quad (2.25)$$

For a temperature gradient in the $+x$ direction, Eq. (2.23) becomes

$$\frac{\partial\gamma}{\partial x} = -\frac{1}{A} \left(S^s + \sum_{i=1}^n N_i^s \left(\frac{\partial\mu_i}{\partial T} \right) \right) \left(\frac{\partial T}{\partial x} \right). \quad (2.26)$$

Dividing Eq. (2.24) and Eq. (2.25) by the volume V and substituting for Eq. (2.20), Eq. (2.26) can be re-expressed as

$$\begin{aligned} \frac{\partial\gamma}{\partial x} = & - \int_{-\infty}^{\infty} dz \sum_{i=1}^n \left(\rho_i(z) s_i(z) - (\rho_i^\alpha \Theta(z) s_i^\alpha + \rho_i^\beta \tilde{\Theta}(-z) s_i^\beta) \right. \\ & \left. - (\rho_i(z) - (\rho_i^\alpha \Theta(z) + \rho_i^\beta \tilde{\Theta}(-z))) s_i^B(z) \right) \left(\frac{\partial T}{\partial x} \right) \end{aligned} \quad (2.27)$$

where

$$\Theta(n) = \begin{cases} 0, & n < 0 \\ 1, & n \geq 0 \end{cases} \quad (2.28)$$

and

$$\tilde{\Theta}(n) = \begin{cases} 0, & n \leq 0 \\ 1, & n > 0 \end{cases} \quad (2.29)$$

Using Eq. (2.22), the expression simplifies to

$$\frac{\partial \gamma}{\partial x} = - \int_{-\infty}^{\infty} dz \sum_{i=1}^n \rho_i(z) (s_i(z) - s_i^B(z)) \left(\frac{\partial T}{\partial x} \right) \quad (2.30)$$

which again using $\mu_i = h_i - T s_i$ can be written as

$$\frac{\partial \gamma}{\partial x} = - \int_{-\infty}^{\infty} dz \left(\frac{\Delta h(z)}{T} \right) \left(\frac{\partial T}{\partial x} \right). \quad (2.31)$$

Substituting Eq. (2.9), the surface tension gradient can be related to the thermo-osmotic force

$$\frac{\partial \gamma}{\partial x} = - \int_{-\infty}^{\infty} dz \frac{\partial P_{xx}(z)}{\partial x}. \quad (2.32)$$

Thus, the physical origin of thermo-osmotic flow is equivalent to that of the thermo-capillary or thermal Marangoni effect. In the case of a fluid-fluid interface, it is conventionally described as flow due to a surface tension gradient.

We note that Ruckenstein [64] postulated a connection between the thermal Marangoni effect and thermophoresis by using an analogous derivation of the electrophoretic velocity in terms of the interfacial tension gradient. Würger [74], in a hydrodynamic treatment of thermophoresis, showed that the surface tension gradient serves as the slip boundary condition that drives colloid transport.

Chapter 3

Microscopic Expressions

In Chapters 1 and 2, we derived expressions for thermo-osmotic slip using both linear non-equilibrium thermodynamics and local thermal equilibrium approximations. In the process, we established that the temperature gradient induces a local pressure gradient, which drives thermo-osmotic flow. Our motivation is to translate the macroscopic picture of the problem into microscopic terms where both fluid and solid are explicitly treated as atoms. To do so, we must examine closely the relevant microscopic expressions.

3.1 Atomic Pressure Expressions

3.1.1 Irving-Kirkwood

A mechanical expression for the pressure tensor in terms of pair distribution functions and pairwise potentials was formulated by Irving and Kirkwood [36]. The derivation that follows is the approach by Ono and Kondo in their comprehensive formulation of the molecular theory of surface tension in liquids [51].

Consider an artificial surface element $d\mathbf{S}$ located at \mathbf{r} that divides the

fluid into two parts as shown in Fig. 3.1. The volume of fluid into which the vector $d\mathbf{S}$ points is the outer fluid, while the volume that the vector points away from is the inner fluid. The force between pairs of molecules acts across $d\mathbf{S}$ when the straight line that connects the centers of the molecules passes through $d\mathbf{S}$. Thus, the force can only act on $d\mathbf{S}$ when the molecules are on opposite sides of the surface element.

A molecule at \mathbf{r}' in the inner fluid feels a force $(\mathbf{R}/R)\phi'(R)$ from a molecule at $\mathbf{r}' + \mathbf{R}$ in the outer fluid, where \mathbf{R} is the relative displacement between the molecules. Following the description above, the intermolecular force acts across $d\mathbf{S}$ if the vector $\mathbf{r}' + \lambda\mathbf{R}$ terminates on $d\mathbf{S}$ for a value of λ between zero and one. If \mathbf{R} is fixed, the volume element over which the vector $\mathbf{r}' + \lambda\mathbf{R}$ terminates on $d\mathbf{S}$ for λ between λ and $\lambda + d\lambda$ is $d\mathbf{S} \cdot \mathbf{R}d\lambda$. The probability of finding a molecule in this volume element and another at $\mathbf{r}' + \mathbf{R}$ ranging over a volume $d\mathbf{R}$ is given by

$$\rho^{(2)}(\mathbf{r}', \mathbf{r}' + \mathbf{R})(d\mathbf{S} \cdot \mathbf{R}d\lambda)d\mathbf{R} = \rho^{(2)}(\mathbf{r} - \lambda\mathbf{R}, \mathbf{r} - \lambda\mathbf{R} + \mathbf{R})(d\mathbf{S} \cdot \mathbf{R}d\lambda)d\mathbf{R} \quad (3.1)$$

where $\rho^{(2)}$ is referred to as the pair distribution function defined as

$$\rho^{(2)}(\mathbf{r} - \lambda\mathbf{R}, \mathbf{r} - \lambda\mathbf{R} + \mathbf{R}) = \left\langle \sum_{i,j}^N \delta(\mathbf{r} - \lambda\mathbf{R} - \mathbf{r}_i)\delta(\mathbf{r} - \lambda\mathbf{R} + \mathbf{R} - \mathbf{r}_j) \right\rangle. \quad (3.2)$$

The total force acting across $d\mathbf{S}$ on the inner fluid is obtained by multiplying Eq. (3.2) by $(\mathbf{R}/R)\phi'(R)$ and integrating over the outer volume

$$\mathbf{F}^{(\phi)}dS = d\mathbf{S} \cdot \int_{\mathbf{R} \cdot d\mathbf{S} > 0} d\mathbf{R} \left[\int_0^1 \frac{\mathbf{R}\mathbf{R}}{R} \phi'(R) \rho^{(2)}(\mathbf{r} - \lambda\mathbf{R}, \mathbf{r} - \lambda\mathbf{R} + \mathbf{R}) d\lambda \right]. \quad (3.3)$$

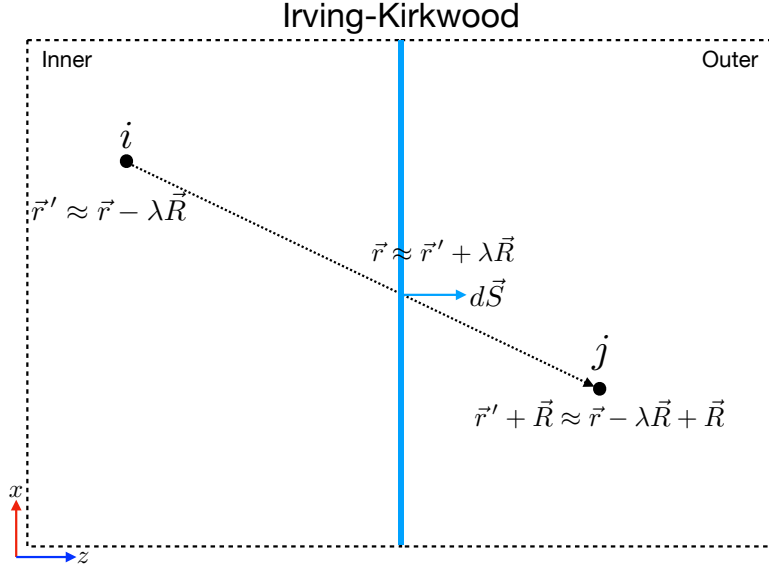


Figure 3.1: Schematic showing the IK definition of the potential contribution to the pressure.

Newton's third law means that

$$\int_0^1 \frac{\mathbf{R}\mathbf{R}}{R} \phi'(R) \rho^{(2)}(\mathbf{r} - \lambda\mathbf{R}, \mathbf{r} - \lambda\mathbf{R} + \mathbf{R}) d\lambda = \quad (3.4)$$

$$\int_0^1 \frac{\mathbf{R}\mathbf{R}}{R} \phi'(R) \rho^{(2)}(\mathbf{r} - \lambda\mathbf{R} + \mathbf{R}, \mathbf{r} - \lambda\mathbf{R}) d\lambda. \quad (3.5)$$

Therefore, Eq. (3.3) can be re-expressed as

$$\mathbf{F}^{(\phi)} dS = \frac{1}{2} d\mathbf{S} \cdot \int d\mathbf{R} \left[\int_0^1 \frac{\mathbf{R}\mathbf{R}}{R} \phi'(R) \rho^{(2)}(\mathbf{r} - \lambda\mathbf{R}, \mathbf{r} - \lambda\mathbf{R} + \mathbf{R}) d\lambda \right] \quad (3.6)$$

where now the integration with respect to \mathbf{R} extends over all space.

The pressure tensor consists of both kinetic and potential contributions. The kinetic term is momentum flux per unit area due to thermal motion of

the particles. This is given by

$$P_{\alpha\beta}^K(\mathbf{r}, t) = \left\langle \sum_{i=1}^N \frac{p_i^\alpha p_i^\beta}{m_i} \delta(\mathbf{r} - \mathbf{r}_i) \right\rangle = \rho(\mathbf{r}) k_B T \quad (3.7)$$

where the equipartition theorem is used in the last equality. In the case of the Irving-Kirkwood pressure expression, the potential contribution is the force acting across dS due to molecules interacting on opposite sides of the surface. This is given by dividing Eq. (3.6) by $-dS$

$$P_{\alpha\beta}^\phi(\mathbf{r}) = -\frac{1}{2} \int d\mathbf{R} \left[\int_0^1 \frac{R^\alpha R^\beta}{R} \phi'(R) \rho^{(2)}(\mathbf{r} - \lambda\mathbf{R}, \mathbf{r} - \lambda\mathbf{R} + \mathbf{R}) d\lambda \right]. \quad (3.8)$$

Essentially, the Irving-Kirkwood definition of pressure gives the force per unit area that separates two molecules.

Eq. (3.8) can be re-expressed for systems with the dividing surface as a (x, y) plane and z axis normal to the surface. Because fluid in such a system is homogeneous in the directions parallel to the interface, the pair distribution function can be expressed as $\rho^{(2)}(z - \lambda Z, z - \lambda Z + \mathbf{R})$. The pressure tensor near a planar interface can be expressed as

$$P_{\alpha\beta}(z) = P_T(z)(\hat{x}\hat{x} + \hat{y}\hat{y}) + P_N(z)\hat{z}\hat{z}. \quad (3.9)$$

Substituting Eq. (3.2), Eq. (3.7) and Eq. (3.8) into Eq. (3.9), the pressure

tensor simplifies to

$$P_T(z) = \rho(z)k_B T - \frac{1}{2} \left\langle \sum_{i,j}^N \int \frac{x_{ij}^2}{r_{ij}} \phi'(r_{ij}) \times \int_0^1 \delta(z - \lambda Z - \mathbf{r}_i) \delta(z - \lambda Z + \mathbf{R} - \mathbf{r}_j) d\lambda d\mathbf{R} \right\rangle \quad (3.10)$$

$$P_N(z) = \rho(z)k_B T - \frac{1}{2} \left\langle \sum_{i,j}^N \int \frac{z_{ij}^2}{r_{ij}} \phi'(r_{ij}) \times \int_0^1 \delta(z - \lambda Z - \mathbf{r}_i) \delta(z - \lambda Z + \mathbf{R} - \mathbf{r}_j) d\lambda d\mathbf{R} \right\rangle. \quad (3.11)$$

Since $P_T = P_{xx} = P_{yy}$ for the planar geometry, the transverse component can equivalently be expressed as

$$P_T(z) = \rho(z)k_B T - \frac{1}{4} \left\langle \sum_{i,j}^N \int \frac{x_{ij}^2 + y_{ij}^2}{r_{ij}} \phi'(r_{ij}) \times \int_0^1 \delta(z - \lambda Z - \mathbf{r}_i) \delta(z - \lambda Z + \mathbf{R} - \mathbf{r}_j) d\lambda d\mathbf{R} \right\rangle. \quad (3.12)$$

Because the fluid is in mechanical equilibrium, P_N must equal the bulk hydrostatic pressure and therefore will be constant for all z .

Irving and Kirkwood add a crucial footnote regarding Eq. (3.6) in that the definition of the force acting across dS is arbitrary. As we will show in the next section, the arbitrariness is reflected in the shape of the contour joining the centers of i and j . Irving and Kirkwood choose a straight line. However, another contour would lead to a different expression for the pressure tensor. From a mesoscopic point of view, integration over a domain large compared with the range of intermolecular forces causes these differences to wash out.

Yet, since we are interested in computing the forces on atoms near the surface, the domain in which we intend to evaluate the pressure is smaller

than the range of intermolecular forces. Therefore, the ambiguity in the definition of the microscopic pressure must be addressed.

3.1.2 Gauge Variance

Schofield and Henderson [65] first related the ambiguity in the microscopic pressure tensor to a gauge variance. Consider a system of interacting particles within a volume. The total linear momentum is given by

$$\mathbf{p}(t) = \sum_{i=1}^N \mathbf{p}_i(t) = \int d\mathbf{r} \mathbf{J}(\mathbf{r}, t) \quad (3.13)$$

where \mathbf{J} is the momentum density which can be expressed in terms of a delta function as

$$\mathbf{J}(\mathbf{r}, t) = \sum_{i=1}^N \mathbf{p}_i(t) \delta(\mathbf{r} - \mathbf{r}_i). \quad (3.14)$$

The force on the volume is defined as the rate of change of the linear momentum on the material given by

$$\dot{\mathbf{J}}(\mathbf{r}, t) = -\nabla_{\mathbf{r}} \cdot \sum_{i=1}^N \mathbf{p}_i(t) \dot{\mathbf{r}}_i \delta(\mathbf{r} - \mathbf{r}_i) + \sum_{i=1}^N \dot{\mathbf{p}}_i(t) \delta(\mathbf{r} - \mathbf{r}_i). \quad (3.15)$$

The first term in Eq. (3.15) when inserted into Eq. (3.13) can be expressed as the divergence of a second-rank tensor

$$\sigma_{\alpha\beta}^K(\mathbf{r}, t) = - \sum_{i=1}^N \frac{p_i^\alpha p_i^\beta}{m_i} \delta(\mathbf{r} - \mathbf{r}_i). \quad (3.16)$$

Once again, using the equipartition theorem this quantity is equivalent to the kinetic contribution to the momentum flux.

Assuming the mass does not change with time and neglecting any external

forces, the second term in Eq. (3.15) can be expressed as

$$\sum_{i=1}^N \dot{\mathbf{p}}_i(t) \delta(\mathbf{r} - \mathbf{r}_i) = - \sum_{i=1}^N \nabla_{\mathbf{r}_i} \phi(\mathbf{r}_i) \delta(\mathbf{r} - \mathbf{r}_i) \quad (3.17)$$

where $\phi(\mathbf{r}_i)$ is the interaction potential between particles. Using the fact that the inter-particle potential is translationally invariant, under the transformation $\mathbf{r}_i \rightarrow \mathbf{r}_i + \mathbf{a}$

$$\sum_{i=1}^N \nabla_{\mathbf{r}_i} \phi(\mathbf{r}_i) = 0. \quad (3.18)$$

Due to translational invariance and considering pair-wise additive potentials where $\mathbf{r}_{ij} = \mathbf{r}_j - \mathbf{r}_i$, the right-hand side of Eq. (3.17) can be expressed as

$$\sum_{i=1}^N \nabla_{\mathbf{r}_i} \phi(\mathbf{r}_i) \delta(\mathbf{r} - \mathbf{r}_i) = \frac{1}{2} \sum_{i \neq j} \mathbf{r}_{ij} \frac{\phi'(r_{ij})}{r_{ij}} [\delta(\mathbf{r} - \mathbf{r}_i) - \delta(\mathbf{r} - \mathbf{r}_j)] \quad (3.19)$$

$$= \frac{1}{2} \sum_{i \neq j} \mathbf{r}_{ij} \frac{\phi'(r_{ij})}{r_{ij}} \delta(\mathbf{r} - \mathbf{l}) \Big|_{\mathbf{r}_j}^{\mathbf{r}_i} \quad (3.20)$$

$$= -\frac{1}{2} \sum_{i \neq j} \mathbf{r}_{ij} \frac{\phi'(r_{ij})}{r_{ij}} \nabla_{\mathbf{r}} \cdot \oint_{C_{ij}} d\mathbf{l} \delta(\mathbf{r} - \mathbf{l}) \quad (3.21)$$

where the contour integral runs from \mathbf{r}_i to \mathbf{r}_j . From Eq. (3.21), it is clear that the second term in Eq. (3.15) can also be expressed as the divergence of a second rank tensor

$$\sigma_{\alpha\beta}^{\phi}(\mathbf{r}, t) = \frac{1}{2} \sum_{i,j} r_{ij}^{\alpha} \frac{\phi'(r_{ij})}{r_{ij}} \oint_{C_{ij}} dl^{\beta} \delta(\mathbf{r} - \mathbf{l}). \quad (3.22)$$

This contribution is momentum flux due to inter-particle forces acting along the contour connecting particles i and j . Upon substitution of Eq. (3.16)

and Eq. (3.22) into Eq. (3.15), momentum balance is recovered

$$\dot{\mathbf{J}}(\mathbf{r}, t) = \nabla \cdot \sigma_{\alpha\beta}(\mathbf{r}, t). \quad (3.23)$$

This expression defines the stress tensor, though not uniquely, since any $\delta\sigma_{\alpha\beta}$ can be added to Eq. (3.23)

$$\dot{\mathbf{J}}(\mathbf{r}, t) = -\nabla \cdot (\sigma_{\alpha\beta}(\mathbf{r}, t) + \delta\sigma_{\alpha\beta}(\mathbf{r}, t)) \quad (3.24)$$

such that

$$\nabla \cdot \delta\sigma_{\alpha\beta}(\mathbf{r}, t) = 0. \quad (3.25)$$

The gauge variance in $\sigma_{\alpha\beta}$ is reflected in the contour C_{ij} chosen in Eq. (3.22). Consider the following contour connecting \mathbf{r}_i to \mathbf{r}_j :

$$\mathbf{l}(\mathbf{r}_i, \mathbf{r}_j) = \mathbf{r}_i + \hat{\mathbf{l}}(\mathbf{r}_{ij}); \quad 0 \leq \hat{\mathbf{l}} \leq \mathbf{r}_{ij} \quad (3.26)$$

Eq. (3.22) then becomes

$$\begin{aligned}
\sigma_{\alpha\beta}^{\phi}(\mathbf{r}, t) &= \frac{1}{2} \sum_{i,j}^N r_{ij}^{\alpha} \frac{\phi'(r_{ij})}{r_{ij}} \oint_{C_{ij}} d\hat{l}^{\beta} \delta(\mathbf{r} - \mathbf{r}_i - \hat{\mathbf{l}}) \\
&= \frac{1}{2} \int d\mathbf{R} \sum_{i,j}^N r_{ij}^{\alpha} \frac{\phi'(r_{ij})}{r_{ij}} \oint_{C_{ij}} d\hat{l}^{\beta} \delta(\mathbf{r} - \mathbf{r}_i - \hat{\mathbf{l}}) \delta(\mathbf{R} - \mathbf{r}_{ij}) \\
&= \frac{1}{2} \int d\mathbf{R} \sum_{i,j}^N r_{ij}^{\alpha} \frac{\phi'(r_{ij})}{r_{ij}} \oint_{C_{ij}} d\hat{l}^{\beta} \delta(\mathbf{r} - \hat{\mathbf{l}} - \mathbf{r}_i) \delta(\mathbf{r}_i + \mathbf{R} - \mathbf{r}_j) \\
&= \frac{1}{2} \int d\mathbf{R} \sum_{i,j}^N r_{ij}^{\alpha} \frac{\phi'(r_{ij})}{r_{ij}} \oint_{C_{ij}} d\hat{l}^{\beta} \delta(\mathbf{r} - \hat{\mathbf{l}} - \mathbf{r}_i) \delta(\mathbf{r} - \hat{\mathbf{l}} + \mathbf{R} - \mathbf{r}_j) \\
&= \frac{1}{2} \int d\mathbf{R} \sum_{i,j}^N r_{ij}^{\alpha} \frac{\phi'(r_{ij})}{r_{ij}} \oint_{C_{ij}} d\hat{l}^{\beta} \delta(\mathbf{r} - \hat{\mathbf{l}} - \mathbf{r}_i) \delta(\mathbf{r} - \hat{\mathbf{l}} + \mathbf{R} - \mathbf{r}_j)
\end{aligned} \tag{3.27}$$

where \mathbf{R} is the separation vector between points \mathbf{r}_i and \mathbf{r}_j . The pressure tensor is the ensemble average of the negative of the stress tensor

$$P_{\alpha\beta}(\mathbf{r}) = -\langle \sigma_{\alpha\beta}(\mathbf{r}, t) \rangle. \tag{3.28}$$

We may, therefore, re-write Eq. (3.27) as

$$\begin{aligned}
P_{\alpha\beta}^{\phi}(\mathbf{r}) &= -\frac{1}{2} \int d\mathbf{R} R^{\alpha} \frac{\phi'(R)}{R} \oint_{C_R} d\hat{l}^{\beta} \left\langle \sum_{i,j}^N \delta(\mathbf{r} - \hat{\mathbf{l}} - \mathbf{r}_i) \delta(\mathbf{r} - \hat{\mathbf{l}} + \mathbf{R} - \mathbf{r}_j) \right\rangle \\
&= -\frac{1}{2} \int d\mathbf{R} R^{\alpha} \frac{\phi'(R)}{R} \oint_{C_R} d\hat{l}^{\beta} \rho^{(2)}(\mathbf{r} - \hat{\mathbf{l}}, \mathbf{r} - \hat{\mathbf{l}} + \mathbf{R}).
\end{aligned} \tag{3.29}$$

Choosing a straight line contour (Fig. 3.1),

$$\hat{\mathbf{l}}(\mathbf{r}_{ij}) = \lambda \mathbf{r}_{ij} \tag{3.30}$$

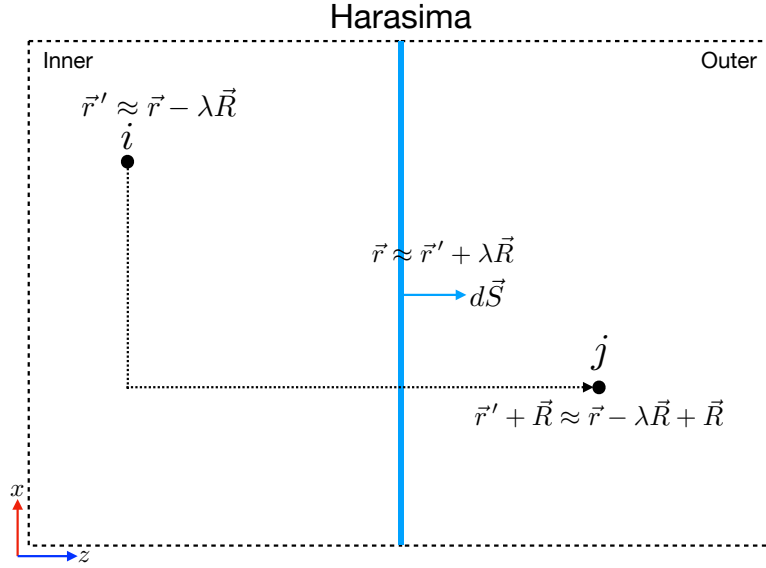


Figure 3.2: Schematic showing the Harasima definition of the potential contribution to the pressure.

we immediately recover the Irving-Kirkwood expression (Eq. (3.8))

$$P_{\alpha\beta}^{\phi}(\mathbf{r}) = -\frac{1}{2} \int d\mathbf{R} \frac{R^{\alpha} R^{\beta}}{R} \phi'(R) \int_0^1 d\lambda \rho^{(2)}(\mathbf{r} - \lambda\mathbf{R}, \mathbf{r} - \lambda\mathbf{R} + \mathbf{R}) \quad (3.31)$$

which reduces to Eq. (3.10) and Eq. (3.11) for a planar geometry.

While a straight line between i and j is the simplest option, it may not be the correct one for an inhomogeneous fluid [65]. For a planar vapor-liquid interface, Harasima derived a different expression for pressure by choosing an asymmetrical contour, $\hat{\mathbf{l}}(\mathbf{r}_{ij})$, that first runs parallel to the interface from \mathbf{r}_i to (x_j, y_j, z_i) and then along the perpendicular to \mathbf{r}_j as shown in Fig. 3.2. The transverse and normal components of the Harasima pressure tensor are

given by

$$P_{xx}(z) = \rho(z)k_B T - \frac{1}{2} \left\langle \sum_{i,j}^N \int \frac{x_{ij}^2}{r_{ij}} \phi'(r_{ij}) \delta(z - \mathbf{r}_i) \delta(z + \mathbf{R} - \mathbf{r}_j) d\mathbf{R} \right\rangle \quad (3.32)$$

$$P_{zz}(z) = \rho(z)k_B T - \frac{1}{2} \left\langle \sum_{i,j}^N \int d\mathbf{R} \frac{z_{ij}^2}{r_{ij}} \phi'(r_{ij}) \times \int_0^1 \delta(z - \lambda Z - \mathbf{r}_i) \delta(z - \lambda Z + \mathbf{R} - \mathbf{r}_j) d\lambda \right\rangle. \quad (3.33)$$

The Irving-Kirkwood and Harasima pressure tensor are two standard expressions derived from momentum balance (Eq. (3.23)). In principle, any contour with arbitrary rotation (Eq. (3.25)) can be chosen resulting in a different microscopic pressure tensor. For an isotropic fluid, choice of the contour is irrelevant since pressure is the same at all points. In Chapter 5, we will show numerically for an inhomogeneous fluid near an interface that the gauge variance does indeed matter.

3.1.3 Virial

The Irving-Kirkwood and Harasima pressure tensors developed in the previous sections are derived from momentum balance (Eq. (3.23)) and therefore ought to be referred to as hydrodynamic expressions. In principle, we should be able to derive a statistical mechanical expression that is consistent with the hydrodynamic expressions. A statistical mechanical expression for pressure can be derived directly from differentiating the free energy with respect to a volume expansion [63]

$$P = - \left(\frac{\partial F}{\partial V} \right)_{T,N}. \quad (3.34)$$

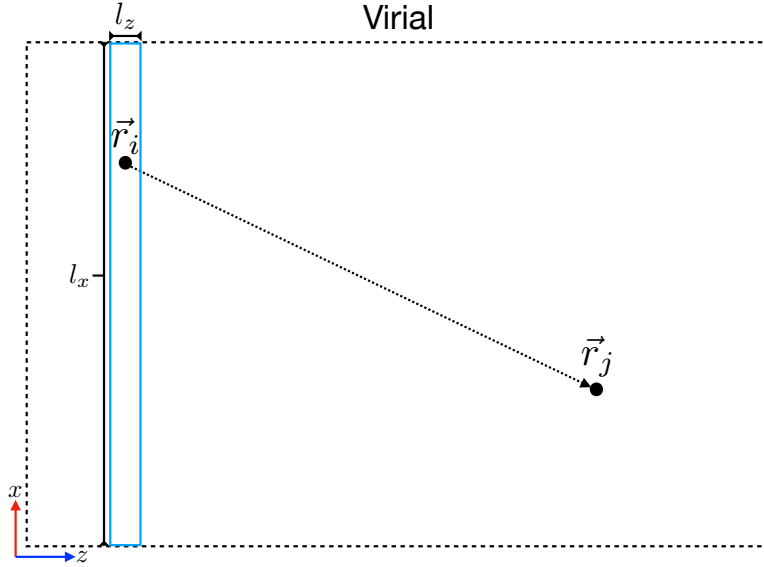


Figure 3.3: Schematic showing the virial definition of the potential contribution to the pressure.

Consider a system of fluid particles contained in a rectangular box with dimensions l_x, l_y, l_z as shown in Fig. 3.3. We introduce the scaled coordinates \mathbf{s}^N by

$$\mathbf{r}_i = l_x \mathbf{s}_{ix} + l_y \mathbf{s}_{iy} + l_z \mathbf{s}_{iz} \quad (3.35)$$

for $i = 1, 2, 3, \dots, N$ meaning that each coordinate s_{ix}, s_{iy}, s_{iz} for any particle i ranges between 0 and 1 within the box.

Inserting scaled coordinates into the expression for the canonical partition function gives

$$Q(N, V, T) = \frac{(l_x l_y l_z)^N}{\Lambda^{3N} N!} \int_0^1 \dots \int_0^1 d\mathbf{s}^N \exp[-\beta U((l_x \mathbf{s}_x)^N, (l_y \mathbf{s}_y)^N, (l_z \mathbf{s}_z)^N)]. \quad (3.36)$$

To obtain the P_{xx} component of pressure, we can differentiate the free energy

with respect to a volume expansion in x

$$P_{xx} = - \left(\frac{\partial F}{\partial l_x} \right)_{l_y, l_z, T, N} \left(\frac{\partial V}{\partial l_x} \right)^{-1}. \quad (3.37)$$

Given that $V = l_x l_y l_z$,

$$P_{xx} = \frac{k_B T}{l_y l_z} \left(\frac{\partial \ln Q}{\partial l_x} \right). \quad (3.38)$$

The first term in the derivative is the kinetic contribution to the pressure

$$P_{xx}^K = \frac{k_B T}{l_x l_y l_z Q} \left(\frac{N V^N}{\Lambda^{3N} N!} \int_0^1 \dots \int_0^1 d\mathbf{s}^N \exp[-\beta U((l_x \mathbf{s}_x)^N, (l_y \mathbf{s}_y)^N, (l_z \mathbf{s}_z)^N)] \right) \quad (3.39)$$

$$= \frac{N k_B T}{V}. \quad (3.40)$$

The second term gives the potential contribution

$$P_{xx}^\phi = - \frac{\beta k_B T}{l_y l_z Q} \left(\frac{V^N}{\Lambda^{3N} N!} \int_0^1 \dots \int_0^1 d\mathbf{s}^N \left(\frac{\partial U}{\partial l_x} \right) \exp[-\beta U] \right). \quad (3.41)$$

Since

$$\frac{\partial}{\partial l_x} = \sum_{i=1}^N \frac{\partial \mathbf{x}_i}{\partial l_x} \cdot \frac{\partial}{\partial \mathbf{x}_i} \quad (3.42)$$

and

$$\mathbf{x}_i = l_x \mathbf{s}_{ix} \quad (3.43)$$

we can write

$$\frac{\partial U}{\partial l_x} = \sum_{i=1}^N \mathbf{s}_{ix} \cdot \frac{\partial U}{\partial \mathbf{x}_i}. \quad (3.44)$$

Therefore, the potential contribution to the pressure can be expressed as

$$P_{xx}^\phi = -\frac{1}{VQ} \left(\frac{V^N}{\Lambda^{3N} N!} \int_0^1 \cdots \int_0^1 d\mathbf{s}^N \sum_{i=1}^N \mathbf{x}_i \cdot \frac{\partial U}{\partial \mathbf{x}_i} \exp[-\beta U] \right) \quad (3.45)$$

$$= \frac{1}{V} \left\langle \sum_{i=1}^N x_i f_i^x \right\rangle. \quad (3.46)$$

Using the fact that

$$\sum_{i=1}^N x_i f_i^x = \frac{1}{2} \sum_{i,j} x_{ij} f_{ij}^x \quad (3.47)$$

the transverse component of the virial pressure for a volume element at position z is given by

$$P_{xx}(z) = \rho(z)k_B T + \frac{1}{V} \left\langle \frac{1}{2} \sum_{i,j} x_{ij} f_{ij}^x \right\rangle. \quad (3.48)$$

For an isotropic fluid, the same procedure can be applied to a volume expansion in z to give the normal component

$$P_{zz}(z) = \rho(z)k_B T + \frac{1}{V} \left\langle \frac{1}{2} \sum_{i,j} z_{ij} f_{ij}^z \right\rangle. \quad (3.49)$$

Eq. (3.48) and Eq. (3.49) can be re-expressed in the form

$$P_{xx}(z) = \rho(z)k_B T - \frac{1}{2} \left\langle \sum_{i,j} \int \frac{x_{ij}^2}{r_{ij}} \phi'(r_{ij}) \delta(z - \mathbf{r}_i) \delta(z + \mathbf{R} - \mathbf{r}_j) d\mathbf{R} \right\rangle \quad (3.50)$$

$$P_{zz}(z) = \rho(z)k_B T - \frac{1}{2} \left\langle \sum_{i,j} \int \frac{z_{ij}^2}{r_{ij}} \phi'(r_{ij}) \delta(z - \mathbf{r}_i) \delta(z + \mathbf{R} - \mathbf{r}_j) d\mathbf{R} \right\rangle. \quad (3.51)$$

Interestingly, in the case of a planar geometry, the transverse component of the virial pressure is equivalent to the transverse component of the Harasima pressure (Eq. (3.32)). The virial expressions for pressure are acceptable with a caveat. The fluid must be homogeneous in the direction of volume expansion. For a slab near an interface, the fluid is homogeneous in x and y but not in z . Thus, in a region where the fluid is inhomogeneous, the transverse component (Eq. (3.48)) is a legitimate expression whereas the normal component (Eq. (3.49)) is not.

3.2 Invariance of Surface Tension

As elucidated in the previous sections, the ambiguity in defining the pressure only becomes a significant issue once knowledge of the microscopic details near an interface is required. From a mesoscopic point of view, all pressure expressions should give the same surface tension. In most cases, when determining the coexistence and stability of interacting phases, knowledge of the surface tension is sufficient and therefore, the ambiguity is typically ignored [48]. We follow the derivation given by Ono and Kondo [51].

The expression for surface tension of a planar interface is given by

$$\gamma = \int_{-\infty}^{\infty} P_N(z) - P_T(z) dz. \quad (3.52)$$

Introducing

$$\rho_{ij}(z - \lambda Z, z - \lambda Z + \mathbf{R}) = \delta(z - \lambda Z - \mathbf{r}_i) \delta(z - \lambda Z + \mathbf{R} - \mathbf{r}_j) \quad (3.53)$$

we may substitute Eq. (3.10) and Eq. (3.11) into Eq. (3.52) giving

$$\gamma = \frac{1}{2} \left\langle \sum_{i,j}^N \int_{-\infty}^{\infty} dz \int d\mathbf{R} \int_0^1 \frac{x_{ij}^2 - z_{ij}^2}{r_{ij}} \phi'(r_{ij}) \rho_{ij}(z - \lambda Z, z - \lambda Z + \mathbf{R}) d\lambda \right\rangle. \quad (3.54)$$

The order of integration with respect to λ and z can be switched such that

$$\int_{-\infty}^{\infty} dz \int_0^1 \rho_{ij}(z - \lambda Z, z - \lambda Z + \mathbf{R}) d\lambda = \int_0^1 d\lambda \int_{-\infty}^{\infty} \rho_{ij}(z - \lambda Z, z - \lambda Z + \mathbf{R}) dz. \quad (3.55)$$

Since

$$\int_0^1 d\lambda \int_{-\infty}^{\infty} \rho_{ij}(z - \lambda Z, z - \lambda Z + \mathbf{R}) dz = \int_0^1 d\lambda \int_{-\infty}^{\infty} \rho_{ij}(z, z + \mathbf{R}) dz, \quad (3.56)$$

that is to say integration of the pair distribution function over all z is invariant to whether atom i is located at $z - \lambda Z$ or z . Therefore, Eq. (3.55) simplifies to

$$\int_0^1 d\lambda \int_{-\infty}^{\infty} \rho_{ij}(z - \lambda Z, z - \lambda Z + \mathbf{R}) dz = \int_{-\infty}^{\infty} \rho_{ij}(z, z + \mathbf{R}) dz. \quad (3.57)$$

The surface tension can be re-expressed in terms of the new pair distribution function

$$\gamma = \frac{1}{2} \left\langle \sum_{i,j}^N \int_{-\infty}^{\infty} dz \int \frac{x_{ij}^2 - z_{ij}^2}{r_{ij}} \phi'(r_{ij}) \rho_{ij}(z, z + \mathbf{R}) d\mathbf{R} \right\rangle. \quad (3.58)$$

The connection to the virial pressure can be observed more clearly. Substituting Eq. (3.50) and Eq. (3.51) into Eq. (3.52) immediately recovers Eq. (3.58).

In short, the surface tension is invariant with respect to the definition of microscopic pressure because upon integration over all z , it is irrelevant where the potential contribution is assigned. For the latter reason, we also expect that from a mesoscopic standpoint, the surface tension gradient induced by the thermal gradient should be the same regardless of the pressure expression.

3.3 Atomic Heat Current Expressions

The ambiguity in defining the potential contribution to the pressure (Section 3.1.2) also extends to heat currents. The microscopic expression for heat transport can be derived from the law of energy conservation

$$\frac{\partial E}{\partial t} + \nabla \cdot [E\mathbf{v} + \mathbf{J}_q - v^\alpha \sigma^{\alpha\beta}] = 0 \quad (3.59)$$

where E is the energy density, $E\mathbf{v}$ is the convective energy current, \mathbf{J}_q is the heat current, and $\sigma^{\alpha\beta}$ is the stress tensor.

Following Irving and Kirkwood's approach [36], the heat current is given by

$$\mathbf{J}_q(\mathbf{r}, t) = \mathbf{J}_q^K(\mathbf{r}, t) + \mathbf{J}_q^\phi(\mathbf{r}, t) \quad (3.60)$$

where \mathbf{J}_q^K is the heat current due to transport of kinetic energy

$$\mathbf{J}_q^K(\mathbf{r}, t) = \sum_{i=1}^N \frac{m}{2} \left\langle \left| \frac{\mathbf{p}_i}{m} - \mathbf{v} \right|^2 \left(\frac{\mathbf{p}_i}{m} - \mathbf{v} \right) \delta(\mathbf{r} - \mathbf{r}_i) \right\rangle \quad (3.61)$$

and \mathbf{J}_q^ϕ is heat transport due to molecular interactions

$$\begin{aligned} \mathbf{J}_q^\phi(\mathbf{r}, t) &= \frac{1}{2} \sum_{i,j} \int \left[\phi(r_{ij}) - \frac{\mathbf{r}_{ij}\mathbf{r}_{ij}}{r_{ij}} \phi'(r_{ij}) \right. \\ &\times \left. \left\{ 1 - \frac{1}{2} \mathbf{r}_{ij} \cdot \nabla + \dots + \frac{1}{n!} (-\mathbf{r}_{ij} \cdot \nabla)^{n-1} + \dots \right\} \right] \\ &\times \left\langle \left(\frac{\mathbf{P}_i}{m} - \mathbf{v} \right) \rho_{ij}(\mathbf{r}, \mathbf{r} + \mathbf{R}) \right\rangle d\mathbf{R}. \end{aligned} \quad (3.62)$$

From the Appendix in [36], the expansion in Eq. (3.62) can be re-expressed as

$$\begin{aligned} \mathbf{J}_q^\phi(\mathbf{r}, t) &= \frac{1}{2} \sum_{i,j} \int \phi(r_{ij}) \left\langle \left(\frac{\mathbf{P}_i}{m} - \mathbf{v} \right) \rho_{ij}(\mathbf{r}, \mathbf{r} + \mathbf{R}) \right\rangle d\mathbf{R} \\ &- \frac{1}{2} \int \frac{\mathbf{r}_{ij}\mathbf{r}_{ij}}{r_{ij}} \phi'(r_{ij}) \int_0^1 \left\{ 1 - \lambda \mathbf{r}_{ij} \cdot \nabla + \dots + \frac{\lambda^{n-1}}{(n-1)!} (-\mathbf{r}_{ij} \cdot \nabla)^{n-1} + \dots \right\} \\ &\times \left\langle \left(\frac{\mathbf{P}_i}{m} - \mathbf{v} \right) \rho_{ij}(\mathbf{r}, \mathbf{r} + \mathbf{R}) \right\rangle d\lambda d\mathbf{R}. \end{aligned} \quad (3.63)$$

This can be further simplified to

$$\begin{aligned} \mathbf{J}_q^{\phi, IK}(\mathbf{r}, t) &= \frac{1}{2} \sum_{i,j} \left[\int \phi(r_{ij}) \left\langle \left(\frac{\mathbf{P}_i}{m} - \mathbf{v} \right) \rho_{ij}(\mathbf{r}, \mathbf{r} + \mathbf{R}) \right\rangle d\mathbf{R} \right. \\ &\left. - \int \frac{\mathbf{r}_{ij}\mathbf{r}_{ij}}{r_{ij}} \phi'(r_{ij}) \int_0^1 \left\langle \left(\frac{\mathbf{P}_i}{m} - \mathbf{v} \right) \rho_{ij}(\mathbf{r} - \lambda \mathbf{R}, \mathbf{r} - \lambda \mathbf{R} + \mathbf{R}) \right\rangle d\lambda d\mathbf{R} \right]. \end{aligned} \quad (3.64)$$

The second term in the brackets is $P_{\alpha\beta}^\phi(\mathbf{r})$ (Eq. (3.8)) multiplied by the fluid velocity in the center of momentum frame. This term is equivalent to the work done per unit time of particle i on j due to net displacement of the fluid.

We can clearly see how the ambiguity discussed in Section 3.1.2 also arises in the heat current. Irving and Kirkwood consider the work that particle i does on j as acting along a straight line that connects their centers. Instead

of distributing the work along the contour, we can instead use the virial expression for pressure to re-express the potential contribution to the heat current as

$$\begin{aligned} \mathbf{J}_q^{\phi,V}(\mathbf{r}, t) = & \frac{1}{2} \sum_{i,j} \left[\int \phi(r_{ij}) \left\langle \left(\frac{\mathbf{P}_i}{m} - \mathbf{v} \right) \rho_{ij}(\mathbf{r}, \mathbf{r} + \mathbf{R}) \right\rangle d\mathbf{R} \right. \\ & \left. - \int \frac{\mathbf{r}_{ij} \mathbf{r}_{ij}}{r_{ij}} \phi'(r_{ij}) \left\langle \left(\frac{\mathbf{P}_i}{m} - \mathbf{v} \right) \rho_{ij}(\mathbf{r}, \mathbf{r} + \mathbf{R}) \right\rangle d\mathbf{R} \right]. \end{aligned} \quad (3.65)$$

The virial expression for heat transport can alternatively be derived from the virial theorem [21] or from taking the first term in the expansion shown in Eq. (3.63). The work that particle j does on i is now assigned at the position of i . For a planar geometry, Eq. (3.65) reduces to

$$\begin{aligned} \mathbf{J}_q^{\phi,V}(z, t) = & \frac{1}{2} \sum_{i,j} \left[\int \phi(r_{ij}) \left\langle \left(\frac{\mathbf{P}_i}{m} - \mathbf{v} \right) \rho_{ij}(z, z + \mathbf{R}) \right\rangle d\mathbf{R} \right. \\ & \left. - \int \frac{\mathbf{r}_{ij} \mathbf{r}_{ij}}{r_{ij}} \phi'(r_{ij}) \left\langle \left(\frac{\mathbf{P}_i}{m} - \mathbf{v} \right) \rho_{ij}(z, z + \mathbf{R}) \right\rangle d\mathbf{R} \right]. \end{aligned} \quad (3.66)$$

Of course, the ambiguity in defining the microscopic heat current vanishes upon integration over a domain large compared with the range of intermolecular forces since it no longer matters where the work is done.

Chapter 4

Computational Tools

In this chapter, we briefly discuss various algorithms used to carry out the calculations presented in Chapters 5-7. All simulations are carried out using standard Molecular Dynamics (MD) methods. The algorithms have been implemented in the Large-scale Atomic/Molecular Massively Parallel Simulator (LAMMPS) developed by Plimpton and co-workers [55].

4.1 Velocity Verlet

There are several ways of integrating Newton's equations of motion to generate an MD trajectory [22]. The conventional Verlet algorithm estimates new positions of molecules with an error of $\mathcal{O}(\Delta t^4)$. The expression for velocity is only accurate to $\mathcal{O}(\Delta t^2)$. The total energy during the trajectory is conserved. The Leap Frog algorithm is a variation of the Verlet scheme that gives rise to identical trajectories. Yet, the velocities are not defined at the same time as the positions, rendering a computation of the total energy at each time-step infeasible. In order to cast the Verlet algorithm in a form that computes positions and velocities simultaneously, we use the velocity Verlet

algorithm. The algorithm starts with a Taylor expansion of the coordinates in the same way as the standard Verlet:

$$r(t + \Delta t) = r(t) + v(t)\Delta t + \frac{f(t)}{2m}\Delta t^2 \quad (4.1)$$

Yet, the update of the velocities changes to

$$v(t + \Delta t) = v(t) + \frac{f(t + \Delta t) + f(t)}{2m}\Delta t. \quad (4.2)$$

In this algorithm, new velocities can be computed only after new positions are computed. From the new positions, $f(t + \Delta t)$ can be computed.

The standard implementation of the algorithm splits integration of positions and velocities into half steps. In the first half-step,

$$v_x\left(t + \frac{\Delta t}{2}\right) = v_x(t) + \frac{f_x(t)}{2m}\Delta t \quad (4.3)$$

$$v_y\left(t + \frac{\Delta t}{2}\right) = v_y(t) + \frac{f_y(t)}{2m}\Delta t \quad (4.4)$$

$$v_z\left(t + \frac{\Delta t}{2}\right) = v_z(t) + \frac{f_z(t)}{2m}\Delta t \quad (4.5)$$

$$x(t + \Delta t) = x(t) + v_x\left(t + \frac{\Delta t}{2}\right)\Delta t \quad (4.6)$$

$$y(t + \Delta t) = y(t) + v_y\left(t + \frac{\Delta t}{2}\right)\Delta t \quad (4.7)$$

$$z(t + \Delta t) = z(t) + v_z\left(t + \frac{\Delta t}{2}\right)\Delta t. \quad (4.8)$$

In the second half-step,

$$v_x(t + \Delta t) = v_x \left(t + \frac{\Delta t}{2} \right) + \frac{f_x(t + \Delta t)}{2m} \Delta t \quad (4.9)$$

$$v_y(t + \Delta t) = v_y \left(t + \frac{\Delta t}{2} \right) + \frac{f_y(t + \Delta t)}{2m} \Delta t \quad (4.10)$$

$$v_z(t + \Delta t) = v_z \left(t + \frac{\Delta t}{2} \right) + \frac{f_z(t + \Delta t)}{2m} \Delta t. \quad (4.11)$$

4.2 Nosé Hoover Thermostat

In order to produce a sampling of the canonical phase space distribution, we use the extended phase approaches developed in detail by Nosé [49], Hoover [32] and Martyna et al [43]. These methods extend phase space by introducing variables that mimic the effect of a heat bath. Nosé’s original approach introduces a Maxwell daemon that checks if the kinetic energy is higher or lower than the target temperature and then scales the velocities [68]. The addition of a coordinate variable s and its conjugate momentum p_s to the Hamiltonian allows the agent to scale the kinetic energy. For a system with physical coordinates $\mathbf{r}_1, \dots, \mathbf{r}_N$, and momenta $\mathbf{p}_1, \dots, \mathbf{p}_N$, the Nosé Hamiltonian is given by

$$\mathcal{H}_N = \sum_{i=1}^N \frac{\mathbf{p}_i^2}{2m_i s^2} + U(\mathbf{r}_1, \dots, \mathbf{r}_N) + \frac{p_s^2}{2Q} + gkT \ln s \quad (4.12)$$

where Q is a parameter that determines the time scale on which the daemon acts. The fudge factor $gkT \ln s$ is chosen so that a micro-canonical distribution of phase space given by \mathcal{H}_N yields a canonical distribution in phase space. While the equations of motion generated by the Nosé Hamiltonian samples the canonical distribution, presence of the scaling variable s makes it difficult to implement them in algorithmic form.

Hoover [32] introduced a non-canonical change of variables to remove the scaling variable [68]. The Nosé-Hoover Hamiltonian is then given by

$$\mathcal{H}'(\mathbf{r}, \eta, \mathbf{p}, p_\eta) = \mathcal{H}(\mathbf{r}, \mathbf{p}) + \frac{p_\eta^2}{2Q} + dNkT\eta \quad (4.13)$$

where η is related to s . The equations of motion generated by \mathcal{H}' is given by

$$\begin{aligned} \dot{\mathbf{r}}_i &= \frac{\mathbf{p}_i}{m_i} \\ \dot{\mathbf{p}}_i &= \mathbf{F}_i - \frac{p_\eta}{Q} \mathbf{p}_i \\ \dot{\eta} &= \frac{p_\eta}{Q} \\ \dot{p}_\eta &= \sum_{i=1}^N \frac{\mathbf{p}_i^2}{m_i} - dNkT. \end{aligned}$$

The Nosé-Hoover equations of motion generate the canonical distribution when \mathcal{H}' is the only conserved quantity. However, with additional conservation laws like Newton's third law,

$$\sum_{i=1}^N \mathbf{F}_i = 0 \quad (4.14)$$

the Nosé-Hoover equations do not generate the correct distribution.

Martyna et al. [43] found that failure of the Nosé-Hoover equations is due to an insufficient number of variables in the extended phase space to offset restrictions imposed by additional conservation laws. The momentum variable of the thermostat p_η must also obey Maxwell-Boltzmann statistics. This can be accomplished by coupling p_η to its own Nosé-Hoover thermostat, which introduces new variables η' and its conjugate momentum $p_{\eta'}$. Of course, the new thermostat will also need to couple to another thermostat so that $p_{\eta'}$

obeys the Maxwell-Boltzmann distribution. This chain of thermostats can continue indefinitely though typically a chain length of 3 or 4 is sufficient for the equations of motion to accurately generate the canonical distribution. The Nosé-Hoover chain equations are given by

$$\begin{aligned}
\dot{\mathbf{r}}_i &= \frac{\mathbf{p}_i}{m_i} \\
\dot{\mathbf{p}}_i &= \mathbf{F}_i - \frac{p_{\eta_1}}{Q_1} \mathbf{p}_i \\
\dot{\eta}_j &= \frac{p_{\eta_j}}{Q_j} & j = 1, \dots, M \\
\dot{p}_{\eta_1} &= \left[\sum_{i=1}^N \frac{\mathbf{p}_i^2}{m_i} - dNkT \right] - \frac{p_{\eta_2}}{Q_2} p_{\eta_1} \\
\dot{p}_{\eta_j} &= \left[\frac{p_{\eta_{j-1}}^2}{Q_{j-1}} - kT \right] - \frac{p_{\eta_{j+1}}}{Q_{j+1}} p_{\eta_j} & j = 2, \dots, M-1 \\
\dot{p}_{\eta_M} &= \left[\frac{p_{\eta_{M-1}}^2}{Q_{M-1}} - kT \right].
\end{aligned}$$

All simulations were thermostatted using the Nosé-Hoover chain equations with chain length $M = 3$. A standard implementation of the algorithm can be found in Ref [22].

4.3 Temperature Gradient Algorithms

In Chapter 6, we develop a protocol to directly measure thermo-osmotic forces via explicit simulation of a temperature gradient. To create a steady-state temperature profile, we describe here a variety of algorithms offered in the literature.

4.3.1 RNEMD

Muller-Plathe [47] developed an algorithm for setting up a temperature gradient by reversing the cause and effect picture: a heat flux is imposed leading to a temperature gradient in the simulation. He, therefore, called it a Reverse Non-equilibrium Molecular Dynamics (RNEMD) approach to simulate a thermal gradient. The algorithm was originally developed as a way to measure thermal conductivity since the Green Kubo route via calculation of the heat flux converges slowly.

The protocol is straightforward. Assuming periodic boundary conditions, the simulation box is divided into N slabs of identical thickness perpendicular to the x -direction. The instantaneous temperature in slab k is given by the equipartition theorem:

$$T_k = \frac{1}{3N_k k_B} \sum_i^{N_k} m_i v_i^2 \quad (4.15)$$

where N_k is the number of atoms in the slab. Slab 0 is the cool region and $N/2$ is the hot region.

A heat flux is generated by exchanging the velocity vector of the hottest atom in the cold region with that of the coldest atom in the hot region so that the temperature in the hot region increases while the temperature of the cold region decreases. Energy transfer from the cold to hot regions results in a temperature gradient in the intervening regions. The swapping rate of velocity vectors determines the magnitude of the imposed heat flux and therefore the temperature gradient.

It can be shown that the RNEMD algorithm conserves total linear momentum, kinetic energy, and total energy. The main drawback is that it is difficult to know a priori the resulting magnitude of the temperature gradient without knowing the thermal conductivity of the fluid.

4.3.2 HEX

The Heat Exchange algorithm (HEX) [35, 3] is similar to the RNEMD approach in that a heat flux is imposed leading to a temperature gradient. Once again, the simulation box is divided into N regions of identical thickness. While energy exchange in RNEMD is carried out by swapping velocity vectors between hot and cold regions, HEX adds and removes energy from regions via rescaling of particle velocities by a factor R . R is chosen in such a way that the non-translational kinetic energy of a region k [73]

$$\mathcal{K}_k = \sum_i^{N_k} \frac{m_i v_i^2}{2} - \frac{m_{cm,k} v_{cm,k}^2}{2} \quad (4.16)$$

changes by ΔE_k while the center of mass velocity $v_{cm,k}$ remains the same.

Within k , rescaling is accomplished by adding an integration step to the velocity Verlet algorithm (see Section 4.1):

$$v_i^{(k)} = R v_i^{(k)} + (1 - R) v_{cm}^{(k)} \quad (4.17)$$

where the rescaling factor R is given by

$$R = \sqrt{1 + \frac{\Delta E_k}{\mathcal{K}_k}} \quad (4.18)$$

If energy is removed from k , $\Delta E_k < 0$ whereas if energy is added, $\Delta E_k > 0$. As the same amount of energy ΔE removed from the “cold” region is added to the “hot” region, the total energy should remain constant. In the steady state, the heat flux between the two regions is given by

$$J_x^q = \frac{\Delta E}{2\Delta t L_z L_y} \quad (4.19)$$

where the factor of two accounts for periodic boundary conditions since half of the heat flows to the hot reservoir in the reference box while the other half flows to the image reservoir.

Wirnsberger et al. [73] pointed out that HEX exhibits a pronounced energy drift over long simulation times. It can be shown that the drift is due to truncation of higher order terms in the Trotter factorization of the Liouville operator. By adding a coordinate integration step to the original algorithm, the enhanced version (eHEX) exhibits no long term energy drift.

4.3.3 Temperature Rescale

Yet, perhaps the most convenient route for imposing a thermal gradient is to rescale the velocities of fluid atoms in different regions of the simulation box. Simply put, slab 0 is thermostatted at a value lower (T_{low}) than the average temperature, while slab $N/2$ is thermostatted at a value higher (T_{high}) than the average temperature. The resulting heat flux sets up the thermal gradient. At each time-step, the velocities of fluid atoms in the T_{high} and T_{low} regions are rescaled using the following algorithm:

$$v_x(t + \Delta t) = v_x(t) \sqrt{\frac{T_{target}}{T(t)}} \quad (4.20)$$

$$v_y(t + \Delta t) = v_y(t) \sqrt{\frac{T_{target}}{T(t)}} \quad (4.21)$$

$$v_z(t + \Delta t) = v_z(t) \sqrt{\frac{T_{target}}{T(t)}} \quad (4.22)$$

While the temperature rescale algorithm may not be as rigorous as the other approaches in regards to energy conservation, it is the simplest method for controlling the magnitude of the temperature gradient, a critical conve-

nience for the non-equilibrium calculations presented in Chapter 6.

Chapter 5

Indirect Approaches

The analytical theory presented in Chapters 1 and 2 does not provide a molecular description of thermo-osmosis. The viscosity η is not constant near the interface and there is yet no molecular expression for the excess enthalpy density $\Delta h(z)$. To avoid making continuum assumptions, we aim to use the molecular expressions derived in Chapter 3 to compute thermo-osmotic slip. The work presented in this chapter describes in detail what has been published in Ref [24].

5.1 Stress Gradient Method

We first use a mechanical route, i.e. by computing the thermo-osmotic force on a volume element directly from the gradient of the microscopic pressure tensor. In essence, we compute the left-hand side of Eq. (2.9) written here for convenience

$$\frac{\partial P_{xx}(z)}{\partial x} = \left(\frac{\Delta h(z)}{T} \right) \frac{\partial T}{\partial x}. \quad (5.1)$$

Yet, such an approach could be problematic due to non-uniqueness of the definition of the microscopic pressure (see Chapter 3.1).

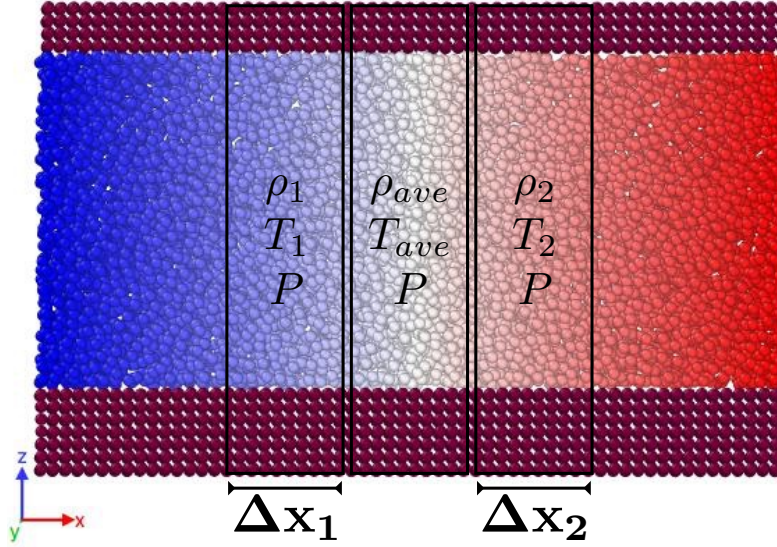


Figure 5.1: A thermal gradient is imposed on fluid interacting with a structured solid surface. Δx_1 and Δx_2 are local equilibrium reservoirs at (ρ_1, T_1, P) and (ρ_2, T_2, P) respectively.

Han [30] postulated a similar approach using local equilibrium approximations. If the temperature gradient is sufficiently slowly varying, the liquid states may still be close to equilibrium. Fig. 5.1 shows that for a slowly varying temperature profile, fluid within a region Δx is locally in thermal equilibrium. Using the fact that P_{xx} depends on x , only through T ,

$$P_{xx}(x, z) \approx P_{xx}^{eq}(x, z) + \mathcal{O}(\nabla T) \quad (5.2)$$

where the superscript *eq* denotes the pressure evaluated at equilibrium. The higher order states can be determined by evaluating the pressure in a system out of equilibrium. The pressure gradient is given by

$$\frac{\partial P_{xx}(z)}{\partial x} \approx \frac{P_{xx}^{eq}(T(x_2), z) - P_{xx}^{eq}(T(x_1), z)}{x_2 - x_1} + \mathcal{O}((\nabla T)^2). \quad (5.3)$$

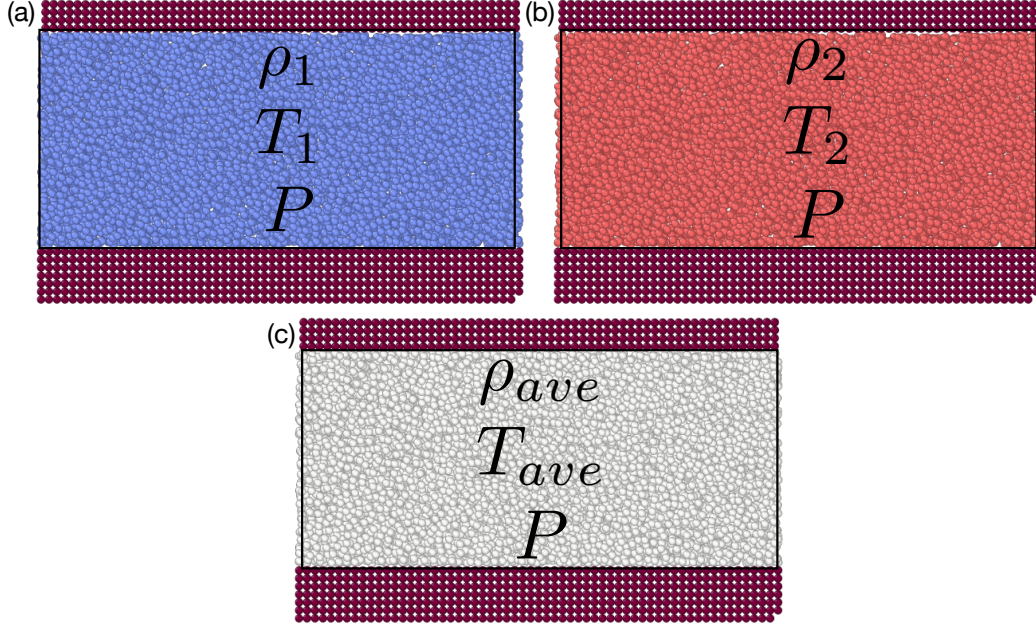


Figure 5.2: Fluid at equilibrium interacting with a structured solid surface. (a) corresponds to local equilibrium state Δx_1 , (b) to Δx_2 , and (c) to the state in between as shown in Fig. 5.1.

Assuming that fluid states are close to equilibrium, we may neglect the higher order term. Since the variation in pressure is solely due to the temperature gradient, Eq. (5.3) can be re-expressed as

$$\frac{\partial P_{xx}(z)}{\partial x} \approx \frac{P_{xx}^{eq}(T_2, z) - P_{xx}^{eq}(T_1, z)}{T_2 - T_1} \left(\frac{\partial T}{\partial x} \right). \quad (5.4)$$

Eq. (5.4) is consistent with the local equilibrium approximations used to derive Eq. (5.1).

Eq. (5.4) is powerful since it provides a simple method for computing the thermo-osmotic force. Because pressure is intensive, $P_{xx}(z)$ within the local equilibrium reservoirs denoted Δx_1 and Δx_2 (Fig. 5.1) will be equivalent to $P_{xx}^{eq}(z)$ in equilibrium systems under the same thermodynamic conditions. Therefore, we may instead consider the systems shown in Fig. 5.2.

To evaluate Eq. (5.4), we equilibrate a system at (ρ_1, T_1, P) (Fig. 5.2(a)) and compute $P_{xx}^{eq}(T_1, z)$ from $z = 0$, where the solid-fluid interface is located, to $z = 10$, where the fluid density approaches the bulk value ρ_1 . We then increase the temperature in such a way that the change in pressure is linear with respect to the change in temperature. The system is then allowed to equilibrate to (ρ_2, T_2, P) . Note that the bulk pressure is kept constant. We now compute the transverse pressure profile $P_{xx}^{eq}(T_2, z)$ for the system at T_2 . Using these pressure calculations, $\Delta P_{xx}/\Delta T$ is determined, and for any $\partial T/\partial x$, the pressure gradient can be computed via Eq. (5.4).

The procedure above gives the average thermo-osmotic force at T_{ave} . The reason is that $\Delta P_{xx}/\Delta T$ also depends on T . Therefore, the entire procedure must be repeated to evaluate the force at a different temperature. To compute the flow profile, we carry out an additional non-equilibrium simulation at $T = T_{ave}$ where we apply the force profile computed via Eq. (5.4) as an artificial body force to the fluid. In practice, because it is difficult to apply a force per unit volume, we divide by the local density profile $\rho(T_{ave}, z)$ to calculate the force per particle

$$f_x^P(z) = -\frac{1}{\rho(T_{ave}, z)} \left(\frac{P_{xx}^{eq}(T_2, z) - P_{xx}^{eq}(T_1, z)}{T_2 - T_1} \right) \left(\frac{\partial T}{\partial x} \right). \quad (5.5)$$

After applying $f_x^P(z)$ to fluid particles, we wait for the system to approach a steady velocity. The resulting thermo-osmotic flow profile is computed. Using the bulk velocity measurement from the non-equilibrium simulation, the thermo-osmosis coefficient β_{12} is given by Eq. (1.16)

$$\beta_{12} = \left(\frac{v_s}{\nabla T/T} \right)_P. \quad (5.6)$$

Note that the bulk pressure is kept constant in the non-equilibrium simula-

tion.

The calculation as described above is complicated by the fact that the pressure tensor in an inhomogeneous fluid is not uniquely defined (see Chapter 3.1). Irving and Kirkwood (IK) [36] derived an expression by integrating the total momentum flux acting across a virtual surface element (see Chapter 3.1.1). This approach gives the appropriate mechanical force balance normal to the interface, that is, P_{zz} is independent of z . However, we want to compute the thermo-osmotic force acting on atoms, rather than the force on a fictitious surface of a volume element. This would suggest that the atom-based virial (V) expression for pressure might be preferable. Yet as discussed in Chapter 3.1.3, the normal component of the virial pressure near the interface will be sensitive to inhomogeneities of fluid density. Deviations from the bulk hydrostatic pressure incorrectly imply a mechanical force imbalance normal to the interface.

In order to determine if the choice of pressure affects the computed thermo-osmosis coefficient, we calculated P_{xx} in Eq. (5.5) using both the V and IK expressions. The V pressure is given by [31] (see Chapter 3.1.3 for derivation)

$$P_{xx}^V(z) = \langle \rho(z) \rangle k_B T - \frac{1}{2V(z)} \left\langle \sum_i^{N(z)} \sum_{j \neq i} \frac{x_{ij}^2}{r_{ij}} \phi'(r_{ij}) \right\rangle \quad (5.7)$$

where r_{ij} is the distance between atoms i and j , x_{ij} is the distance in x , $\phi(r_{ij})$ is the interaction potential between the atoms, $V(z)$ and $N(z)$ are the bin volume and number of atoms in the bin at position z . The IK pressure (see

Chapter 3.1.1 for derivation) can be expressed as [70] (see Appendix 9.3)

$$P_{xx}^{IK}(z) = \langle \rho(z) \rangle k_B T - \frac{1}{2A} \left\langle \sum_i^N \sum_{j \neq i} \frac{x_{ij}^2 \phi'(r_{ij})}{r_{ij} |z_{ij}|} \Theta \left(\frac{z - z_i}{z_{ij}} \right) \Theta \left(\frac{z_j - z}{z_{ij}} \right) \right\rangle. \quad (5.8)$$

5.2 Thermodynamic Method

The mechanical approach suffers from the ambiguity in defining where the potential contribution to the pressure acts. An alternative approach is to evaluate the right-hand side of Eq. (5.1). In Chapter 1, we contended that there exists no molecular expression for evaluating the excess enthalpy density. The reason is that the local specific enthalpy $h(z)$ near an interface is ill-defined. In the bulk, the specific enthalpy is simply given by

$$h^B = u^B + P/\rho^B \quad (5.9)$$

where u^B is the bulk specific internal energy, P is the thermodynamic pressure, and ρ^B is the bulk density. All of these quantities are uniquely defined in the bulk where fluid is homogeneous and isotropic. The difficulty in defining $h(z)$ is that $P_T \neq P_N$ near the interface. Thus, there is an ambiguity in deciding whether the normal or transverse component of the pressure tensor should enter.

Consider Derjaguin's expression for isothermal heat transfer due to a pressure gradient (Eq. (1.18)). The microscopic expression for heat flux in a one component system is

$$\mathbf{J}_q = \frac{1}{V} \left[\sum_{i=1}^N u_i \mathbf{v}_i + \frac{1}{2} \sum_{i,j}^N \mathbf{r}_{ij} (\mathbf{v}_i \cdot \mathbf{f}_{ij}) \right] \quad (5.10)$$

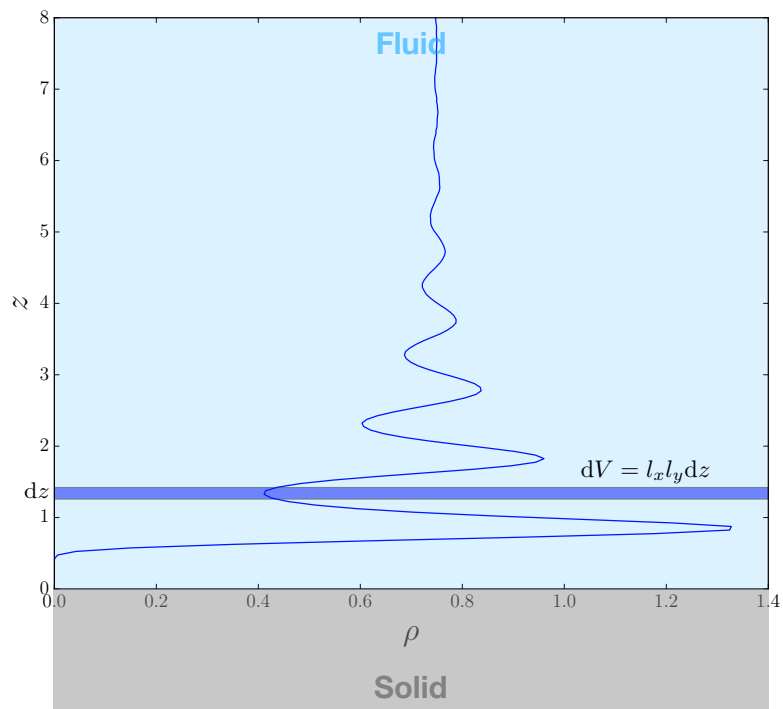


Figure 5.3: Sample density profile of a Lennard-Jones fluid interacting with a solid surface. Within a slab dV , fluid is in local thermal equilibrium. If the slab is near the interface, fluid density is homogeneous in the x and y directions, but inhomogeneous in the z direction.

where u_i is the instantaneous internal energy of particle i , $\mathbf{r}_{ij} = \mathbf{r}_i - \mathbf{r}_j$ is the vectorial distance between particles i and j , \mathbf{v}_i is the velocity of particle i , and \mathbf{f}_{ij} is the intermolecular force acting between particles i and j .

To calculate the Onsager reciprocal coefficient via Derjaguin's approach, we evaluate the excess heat flux (Eq. (1.18)) at a height z above the surface due to a steady flow field parallel to the interface. Recalling Eq. (1.3), if flow due to the pressure gradient is in the x direction, the measurable heat flux is given by

$$\begin{aligned} \langle J'_{q,x}(z) \rangle &= \rho(z)v_x(z)(u(z) - \langle u^B \rangle) \\ &+ \frac{1}{2V} \langle v_x(z) \rangle \sum_{i,j} (x_{ij} f_{ij}^x(z) - \langle x_{ij} f_{ij}^x(\text{bulk}) \rangle) \end{aligned} \quad (5.11)$$

where u is the specific internal energy. As expected, in the bulk, there is no heat transfer. According to Eq. (5.11), the measurable heat flux is equivalent to the excess enthalpy flux provided that the virial contribution to the local enthalpy contains only the transverse component.

The preceding analysis can explain why the transverse component of the pressure enters the local enthalpy. Yet, we should proceed with caution since as described in Chapter 3.3, we can equivalently consider the IK expression for heat transfer (Eq. (3.64)) in formulating Eq. (5.11). Doing so would suggest that the transverse component of the IK pressure ought to enter the local enthalpy.

To resolve the latter ambiguity, consider the fluid shown in Fig. 5.3. If the entire fluid is in equilibrium, then we can choose a volume element near the surface $dV = l_x l_y dz$, which is also in equilibrium. The enthalpy is a thermodynamic state function depending on the internal energy, pressure

and volume of the element. Therefore, the pressure that enters is given by

$$P = - \left(\frac{\partial F}{\partial V} \right)_{T,N}. \quad (5.12)$$

Yet as shown in Chapter 3.1.3, Eq. (5.12) only holds for a volume expansion in x and y , the directions in which the fluid is homogeneous. Due to symmetry, $P_{xx} = P_{yy}$ for all z . Therefore, in order for pressure to reflect the thermodynamic state of the volume element $P = P_{xx} = P_{yy}$ and it is the transverse component of the virial pressure tensor that must enter the expression for local enthalpy.

Using the latter argument, we express the local specific enthalpy as

$$h(z) = u(z) + \frac{P_{xx}^V(z)}{\rho(z)}, \quad (5.13)$$

where the virial expression for pressure enters since it is derived from differentiating the free energy (Chapter 3.1.3). The thermo-osmotic force per particle is then given by

$$f_x^P(z) = - \frac{(h(z) - h^B)}{T} \left(\frac{\partial T}{\partial x} \right). \quad (5.14)$$

We refer to the force computed via Eq. (5.14) as the *LTE* approach. We can compute Eq. (5.14) in a simulation thermostatted at T_{ave} (Fig. 5.2(c)) and apply it as a body force in the same vein as Eq. (5.5).

5.3 Derjaguin Method

The arguments (Eq. (5.10)-Eq. (5.11)) used in constructing an expression for the local enthalpy suggest another approach for computing thermo-osmotic

slip. Because it is difficult to directly calculate the fluid flow due to a thermal gradient, we consider the Onsager reciprocal coefficient that describes the excess heat flux due to hydrodynamic flow. As derived in Chapter 1.1.2, β_{21} , the ratio of isothermal excess heat transfer to an externally imposed pressure gradient, is given by

$$\beta_{21} = - \left(\frac{J_x^q - h^B v_x}{\nabla P} \right)_T. \quad (5.15)$$

Substituting Eq. (5.10) into Eq. (5.15) gives

$$\beta_{21} = \left(\frac{\frac{1}{V} \left[\sum_i^N (p_i^2/2m + \sum_{i<j} \phi_{ij}) v_i^x - 1/2 \sum_{i<j} (x_{ij}^2/r_{ij}) \phi'(r_{ij}) (v_i^x + v_j^x) - \sum_i^N h^B v_i^x \right]}{\nabla P} \right)_T. \quad (5.16)$$

We must note that because the excess heat current is integrated over the entire fluid domain, choice of the heat current expression (see Chapter 3.3) is irrelevant. We pick the virial expression since it is most convenient to compute.

A pressure gradient can be easily introduced as an artificial body force on the fluid

$$f_x^P(z) = - \frac{\nabla P}{\rho(z)} \quad (5.17)$$

where $\rho(z)$ is the density profile at T_{ave} . We can then compute β_{21} via Eq. (5.16). The mechanical and thermodynamic approaches for computing β_{12} and the ‘Derjaguin’ method for calculating β_{21} should be equivalent if the temperature and pressure gradients are small enough to ensure that the resulting response is linear. Indeed, we can test if transport is in the linear regime by applying pressure gradients of different magnitude and checking if β_{21} remains constant. Unlike the other methods, the ‘Derjaguin’ method does not give a flow profile. It can only predict the slip velocity.

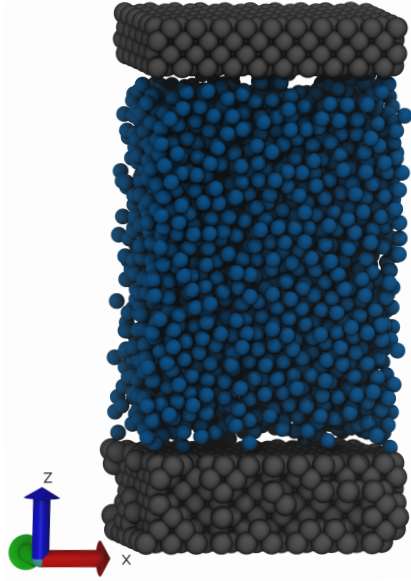


Figure 5.4: Atomic fluid (blue) interacting with solid walls (grey) in a slit pore.

5.4 Results

All Molecular Dynamics simulations reported here were performed using the LAMMPS package [55]. The simulation setup is depicted in Fig. 5.4. The system consists of $N = 2640$ fluid atoms interacting with other fluid atoms and solid atoms via a truncated and shifted Lennard-Jones potential

$$V_{\text{trunc}}(r) = \begin{cases} 4\epsilon \left[\left(\frac{\sigma}{r}\right)^{12} - \left(\frac{\sigma}{r}\right)^6 \right] - V(r_c) & r \leq r_c \\ 0 & r > r_c. \end{cases} \quad (5.18)$$

where $r_c = 4\sigma$, $\sigma_{\text{fluid-fluid}} = \sigma_{\text{solid-fluid}} = \sigma$ and $\epsilon_{\text{fluid-fluid}} = \epsilon$. Two different wall-fluid interactions were investigated: a less attractive Lennard-Jones potential where $\epsilon_{\text{solid-fluid}} = 0.55\epsilon$ and a purely repulsive Weeks-Chandler-Andersen potential [71] such that $r_c = 2^{1/6}\sigma$ for solid-fluid interactions.

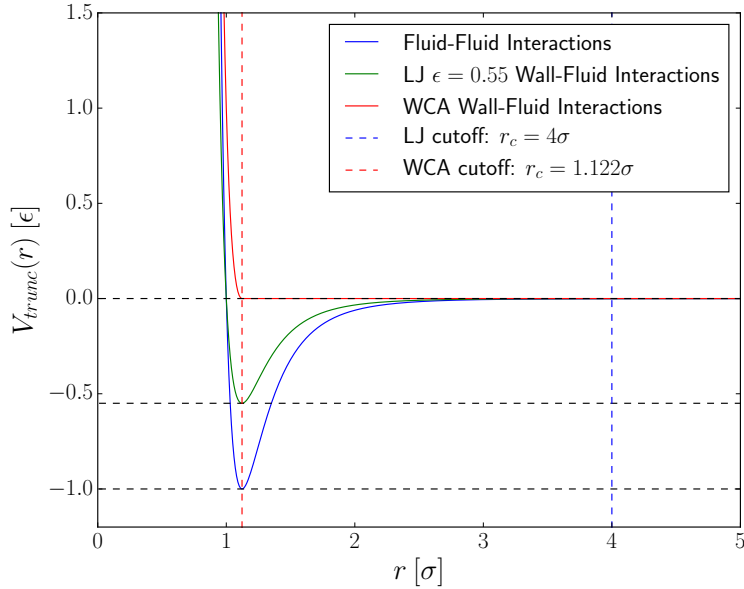


Figure 5.5: Interaction potentials used in the simulations.

Fig. 5.5 shows all possible intermolecular potentials describing fluid-fluid and wall-fluid interactions.

Solid atoms are bonded via a harmonic potential to nearest neighbors in an fcc lattice of density $0.9\sigma^{-3}$

$$V_{\text{bond}}(r) = \frac{1}{2}k(r - r_{\text{eq}})^2 \quad (5.19)$$

where the spring constant $k = 5000\epsilon/\sigma^2$ and equilibrium rest length $r_{\text{eq}} = 1.1626\sigma$. The fluid is in contact with the $\{001\}$ face of the crystal lattice. All computed quantities are expressed in Lennard-Jones reduced units.

NVT dynamics with a time-step $\Delta t = 0.001\tau$ were run to equilibrate the system. This was accomplished using a Nosé-Hoover thermostat (see Chapter 4.2) for 100,000 MD steps. For an additional 100,000 steps, the

system was barostatted at $P_{ext} \approx 0.122$ by applying a downward force to the top wall atoms

$$f_z^p = -\frac{P_{ext}l_xl_y}{N_{top}}. \quad (5.20)$$

Fluid density profiles at $T = 0.8, 0.9, 1.0$ for the different surfaces are shown in Figs. 5.6 and 5.7. The density profile is given by

$$\rho(z) = \rho^B e^{-\beta\Delta\mu^{ex}(z)} \quad (5.21)$$

where $\Delta\mu^{ex}(z)$ is the difference between the excess chemical potential at a distance z from the wall and its value in the bulk. For Lennard-Jones wall-fluid interactions, the density profile resembles the pair correlation function of an isotropic Lennard-Jones fluid. However, for WCA interactions, the density monotonically increases as a function of z . For the WCA wall, the system is close to a de-wetting regime where a vapor phase exists between the solid surface and the liquid.

To calculate the thermo-osmotic force via the ‘stress gradient’ method, the V (Eq. (5.7)) and IK (Eq. (5.8)) transverse pressure profiles were computed within slabs of thickness $dz = 0.05$ for 3×10^7 time-steps. In order to determine the temperature dependence of the thermo-osmotic force, the pressure was calculated for a range of temperatures $T \approx 0.75 - 1.05$. Figs. 5.8 and 5.9 show V and IK pressure profiles near the purely repulsive surface while Figs. 5.10 and 5.11 show those near the Lennard-Jones wall. At the Lennard-Jones surface, the fluid density is significantly more inhomogeneous (Fig. 5.6) causing large fluctuations in the transverse pressure.

As temperature increases in both cases, the difference in fluid density with respect to the bulk decreases, causing the anisotropy in the transverse pressure to also decrease. In the bulk, all profiles converge to the hydrostatic

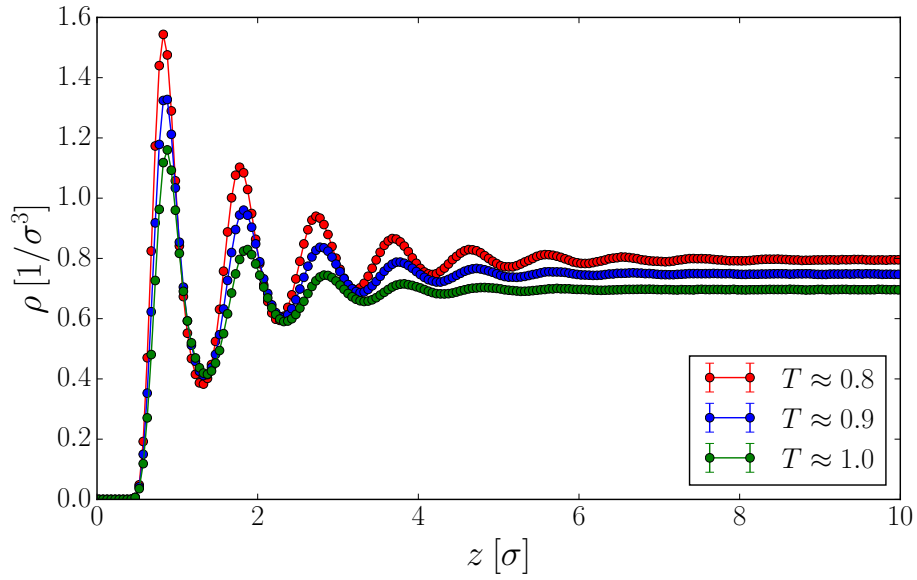


Figure 5.6: Density profiles for Lennard-Jones wall-fluid interactions. The solid wall is located at $z \sim 0$.

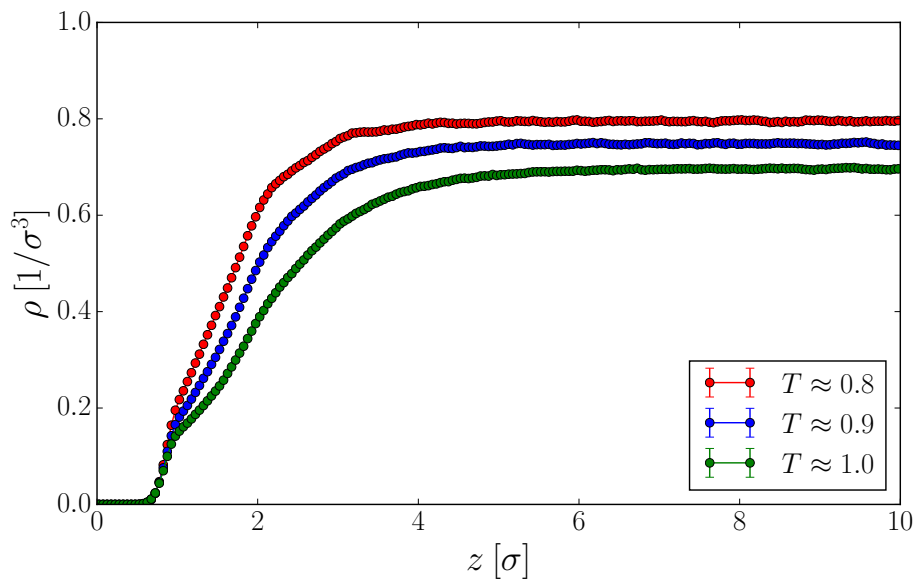


Figure 5.7: Density profiles for WCA wall-fluid interactions. The solid wall is located at $z \sim 0$.

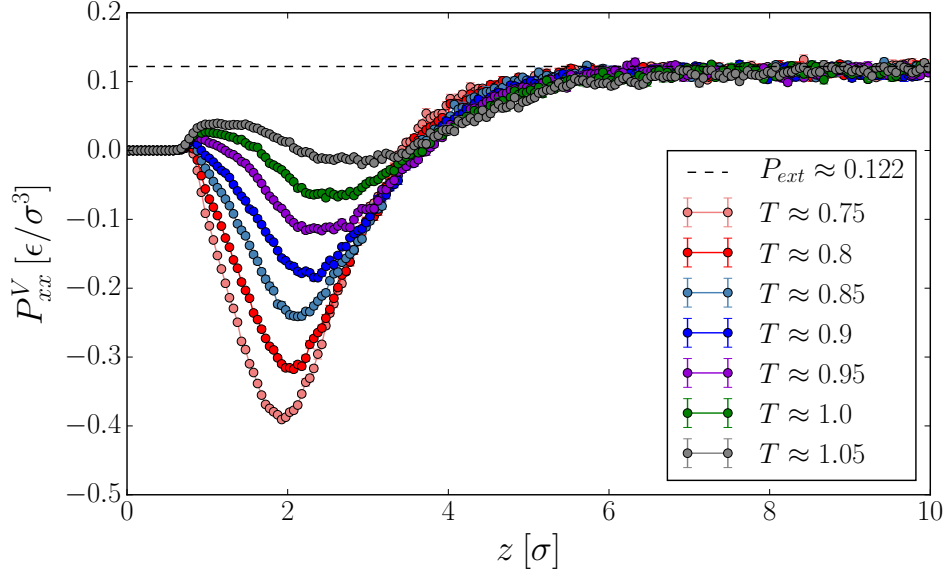


Figure 5.8: Transverse virial pressure profiles for WCA wall-fluid interactions.

pressure $P \approx 0.122$ as expected.

Using the pressure profiles in Figs. 5.8-5.11, $\Delta P_{xx}(z)/\Delta T$ was computed for $T = 0.8, 0.9, 1.0$ and shown in Figs. 5.12-5.13(a, b). As an example, the profile for $T = 0.9$ is computed by taking the difference in P_{xx} at $T = 0.95$ and 0.85 in Figs. 5.8-5.11 and dividing by $\Delta T = 0.1$. Interestingly, for WCA wall-fluid interactions, choice of the pressure tensor does not seem to make an appreciable difference.

To calculate the thermo-osmotic force via the ‘thermodynamic’ method, we first compute $u(z)$ in Eq. (5.13). At constant temperature, the specific kinetic energy is uniform everywhere and therefore given by $(3/2)k_B T$. For $T = 0.8, 0.9$, and 1.0 , the specific potential energy profiles were spatially averaged in z using a slab thickness $dz = 0.05$. Fig. 5.14 shows the sum of the specific kinetic and potential energy profiles as a function of z . Di-

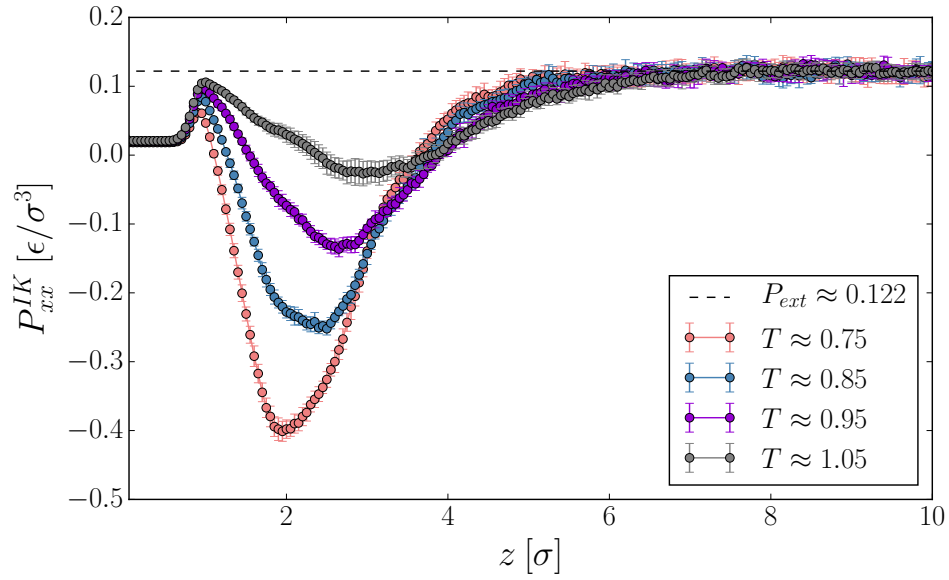


Figure 5.9: Transverse Irving-Kirkwood pressure profiles for WCA wall-fluid interactions.

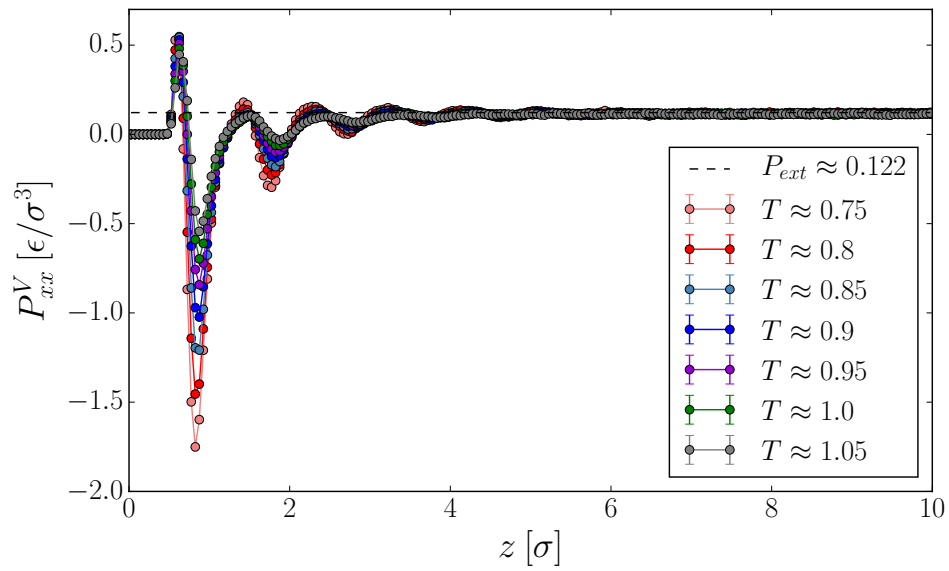


Figure 5.10: Transverse virial pressure profiles for LJ wall-fluid interactions.

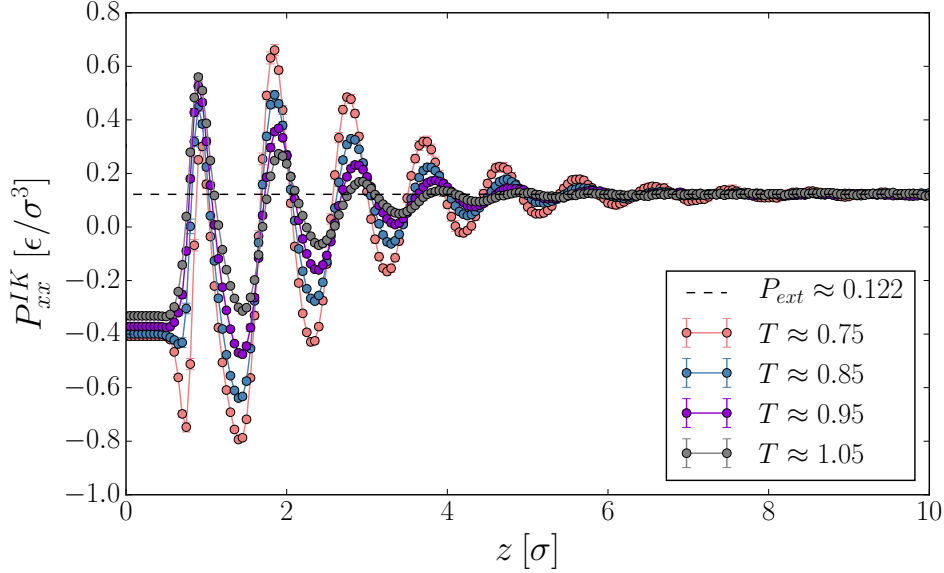


Figure 5.11: Transverse Irving-Kirkwood pressure profiles for LJ wall-fluid interactions.

viding the profiles of P_{xx}^V at the same temperatures (Figs. 5.8 and 5.10) by the corresponding density profiles in Figs. 5.6-5.7 and adding them to $u(z)$ (Fig. 5.14) gives the specific enthalpy $h(z)$. The bulk specific enthalpy h^B is calculated by taking the average value of $h(z)$ from $z = 6$ to $z = 10$. Finally, $\Delta h(z)/T$ was computed via Eq. (5.13) and Eq. (5.14). Profiles are shown in Figs. 5.12-5.13(c).

We note that the IK and V expressions (Figs. 5.12-5.13(a,b)) and LTE quantity (Figs. 5.12-5.13(c)) show similar qualitative behavior. The force profiles flatten and shift outward as the temperature increases, while vanishing in the bulk.

The body force per particle $f_x^P(z)$ can be computed by dividing the profiles in Figs. 5.12-5.13(a-c) by the corresponding density profiles $\rho(z)$ (Figs. 5.6-5.7) and multiplying by a sufficiently small gradient such that the

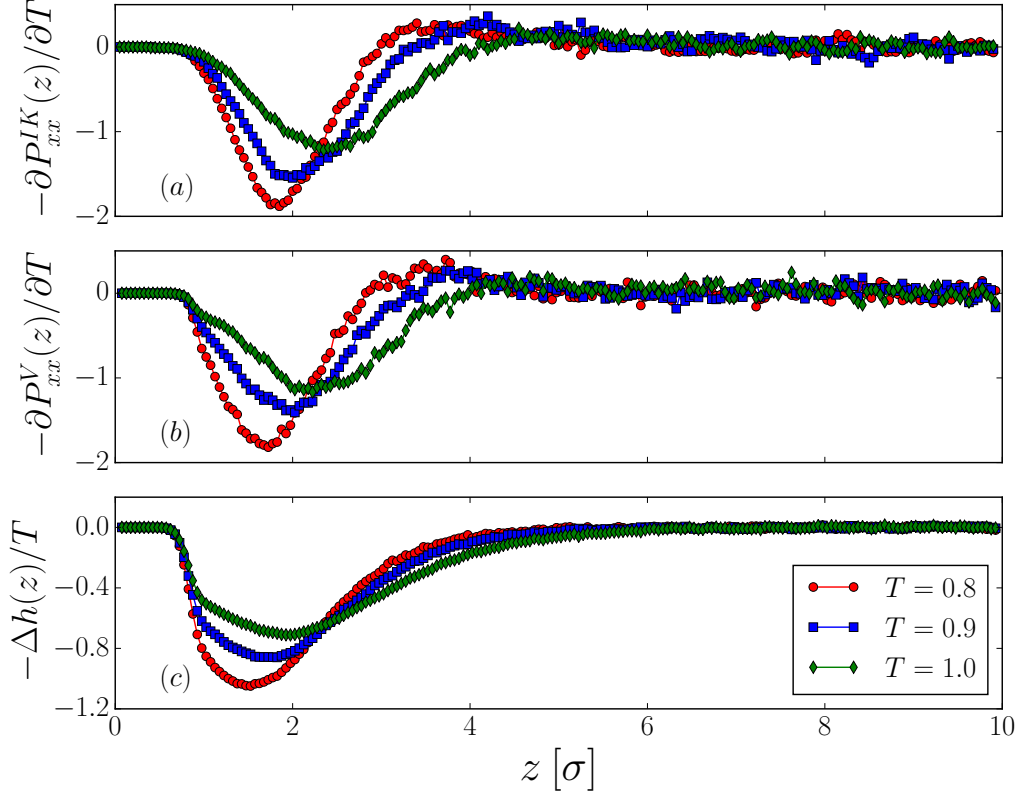


Figure 5.12: WCA wall-fluid interactions: $-\Delta P_{xx}(z)/\Delta T [k_B/\sigma^3]$ computed using the (a) IK and (b) V pressure tensor. (c) Purely repulsive interactions significantly exclude volume and thereby create a large enthalpy difference at the surface.

resulting transport is in the linear regime. We choose $\nabla T = 0.0005$ for the WCA and $\nabla T = 0.003$ for the Lennard-Jones surface. To compute the slip velocity, non-equilibrium simulations were carried out by applying these forces to the equilibrated systems. To obtain reasonable statistics, the forces were applied for 10^8 steps until the fluid approached a steady velocity. The slip was then computed for an additional 2×10^8 steps. Figs. 5.15(a,b) show calculations of the slip velocity. Interestingly, although the mechanical and LTE approaches give different force profiles (Figs. 5.12-5.13), they predict similar slip velocities far away from the surface. We offer an explanation for

the latter finding in Chapter 7.

To compute the Onsager reciprocal coefficient, β_{21} , a uniform pressure gradient was simulated by applying a force per particle $f_x^P(z) = -\nabla P/\rho(z)$ to all fluid atoms. Fig. 5.16 shows the force profile for different values of ∇P at $T = 0.9$ for the WCA surface. Body forces were applied for 10^8 steps and the excess heat flux given by Eq. (5.11) was computed for 2×10^8 steps. Fig. 5.17 shows calculations of β_{21} via Eq. (5.16) at a WCA surface for each force profile shown in Fig. 5.16.

For sufficiently small gradients, β_{21} remains constant, indicating that transport is in the linear regime. Within this regime, the Onsager reciprocal relations hold. Beyond $\nabla P = 0.0001$, β_{21} increases, indicating entrance into a nonlinear regime. In the bulk, the excess heat current vanishes as long as the response is linear.

The flow profiles computed at $T = 0.9$ (Fig. 5.18(a)) shows that for WCA wall interactions the velocity decreases monotonically, indicating that the viscosity remains constant close to the surface. Interestingly, the flow profile is effectively the same for all methods. For a less attractive Lennard-Jones surface (Fig. 5.18(b)), the viscosity and forces are clearly not constant, showing significant departure from (Navier-)Stokes and Derjaguin’s result (Eq. (1.26)). Moreover, the thermo-osmotic flow profile in the latter case depends strongly on the method. The slip velocity predicted by the ‘Derjaguin method’ is shown in red and agrees well with both the stress gradient and LTE approaches.

To clearly compare our approaches for different temperatures, β_{12} was computed via Eq. (5.6) using the slip calculations shown in Fig. 5.15. Fig. 5.19 shows reasonable agreement among all four methods. For $T \sim 96 - 120$ K in Argon units, the thermo-osmosis coefficient ranges from $0.85 - 3.8 \times 10^{-8} \text{m}^2/\text{s}$

for less attractive Lennard-Jones and $4.2 - 5.6 \times 10^{-6} \text{m}^2/\text{s}$ for WCA walls. As expected, the slip velocities for solely repulsive wall-fluid interactions are considerably larger than those for surface forces with an attractive component. Furthermore, both cases demonstrate an approximately linear dependence of the thermo-osmosis coefficient with respect to temperature.

Previous molecular simulation studies of thermal transport have dealt with the Soret coefficient of atomic species [61][62]. One cannot directly compare the Soret coefficient S_T with our computed values of the thermo-osmosis coefficient β_{12} since there is no distinction between excess and bulk enthalpy density if all particles have the same size. In a poly-disperse system, it may be possible to relate the excess enthalpy density to the solvation free energy of larger particles. Yet, even in this Hückel limit, the mechanism of transport is different from what we have explored here [6].

As a rough comparison, given that $S_T = (\beta_{12}/T)/D_{Ar}$, taking the average of our computed values of β_{12} for $T = 0.8$ and 0.9 and using $D_{Ar} \simeq 2.47 \times 10^{-5} \text{cm}^2\text{s}^{-1}$ as reported in Ref. [61], we compute $S_T \sim 0.047 \text{K}^{-1}$, which is the same order of magnitude as their value for $S_T \sim 0.014 \text{K}^{-1}$ at $T = 0.85$.

The key results reported in this chapter are encouraging and surprising: for certain wall-fluid interactions, the thermo-osmotic flow profile does not monotonically depend on the distance from the surface, indicating that the viscosity and forces near the surface are not constant. Furthermore, we find that all methods yield results for the thermo-osmosis coefficient that do not differ significantly. None of these methods assume that macroscopic thermodynamics or hydrodynamics holds close to an interface.

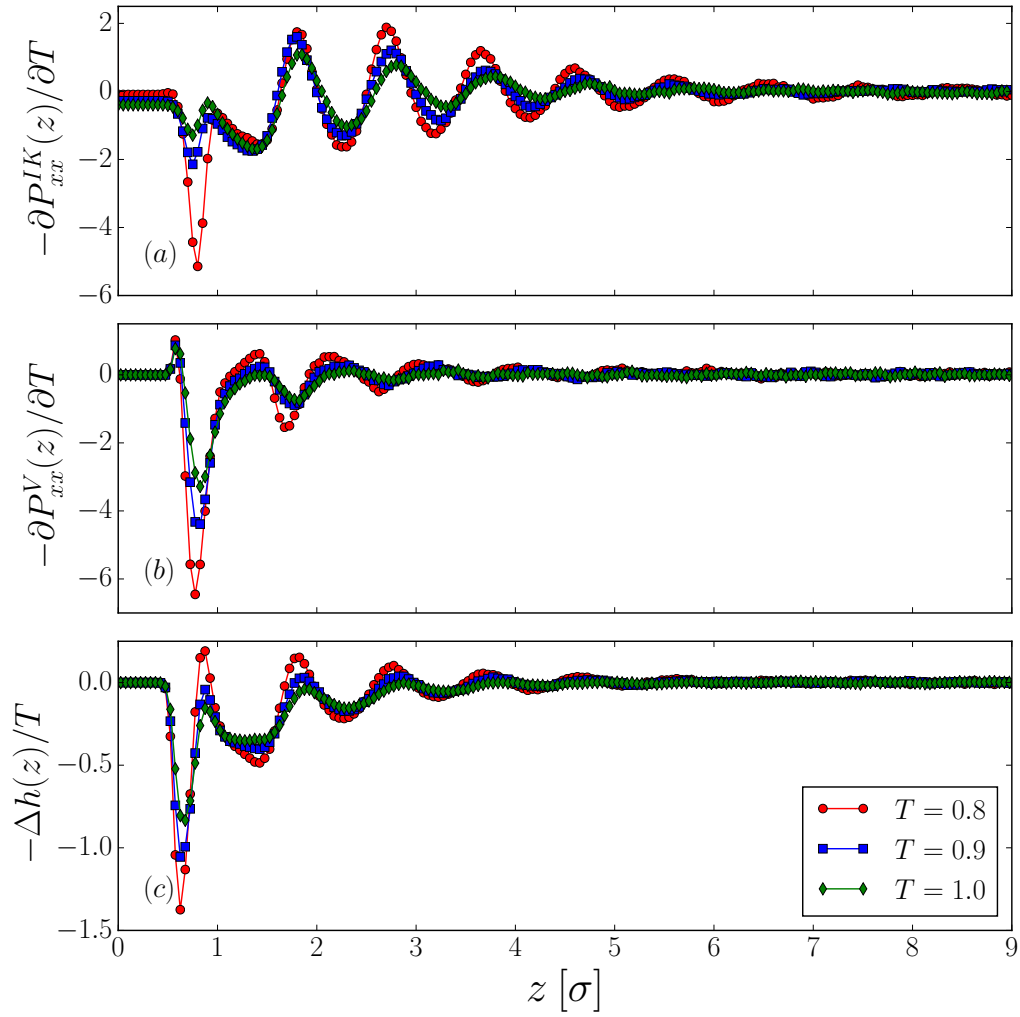


Figure 5.13: LJ wall-fluid interactions: $-\Delta P_{xx}(z)/\Delta T$ [k_B/σ^3] computed using the (a) IK and (b) V pressure tensor. (c) Calculation of thermodynamic force using the local enthalpy expression.

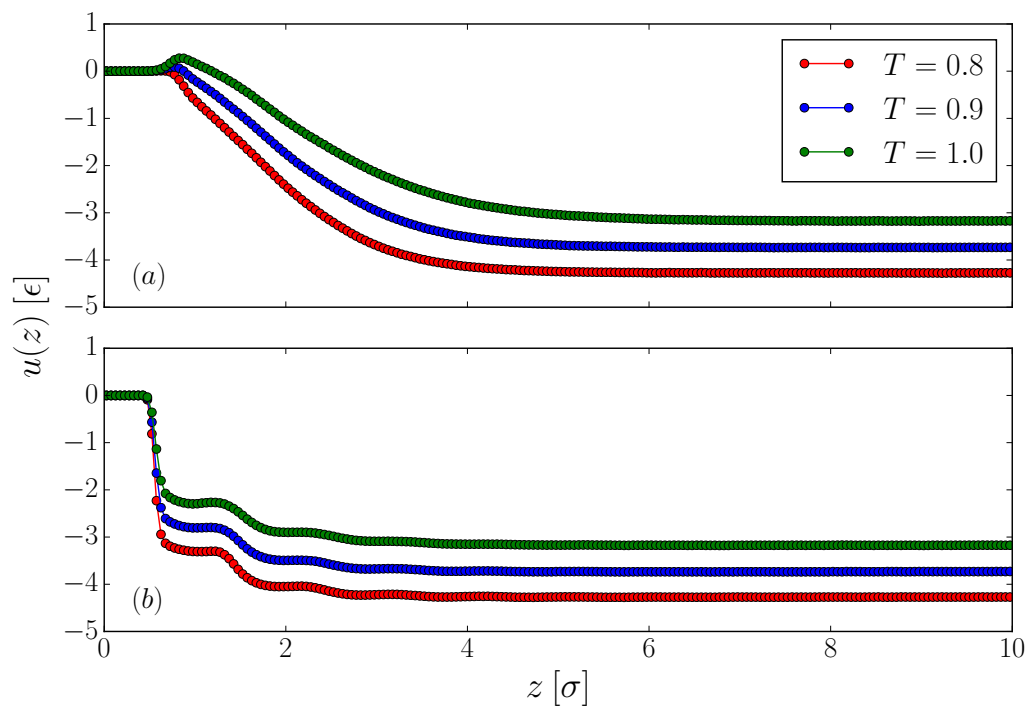


Figure 5.14: Specific internal energy profiles for (a) WCA and (b) Lennard-Jones wall-fluid interactions.

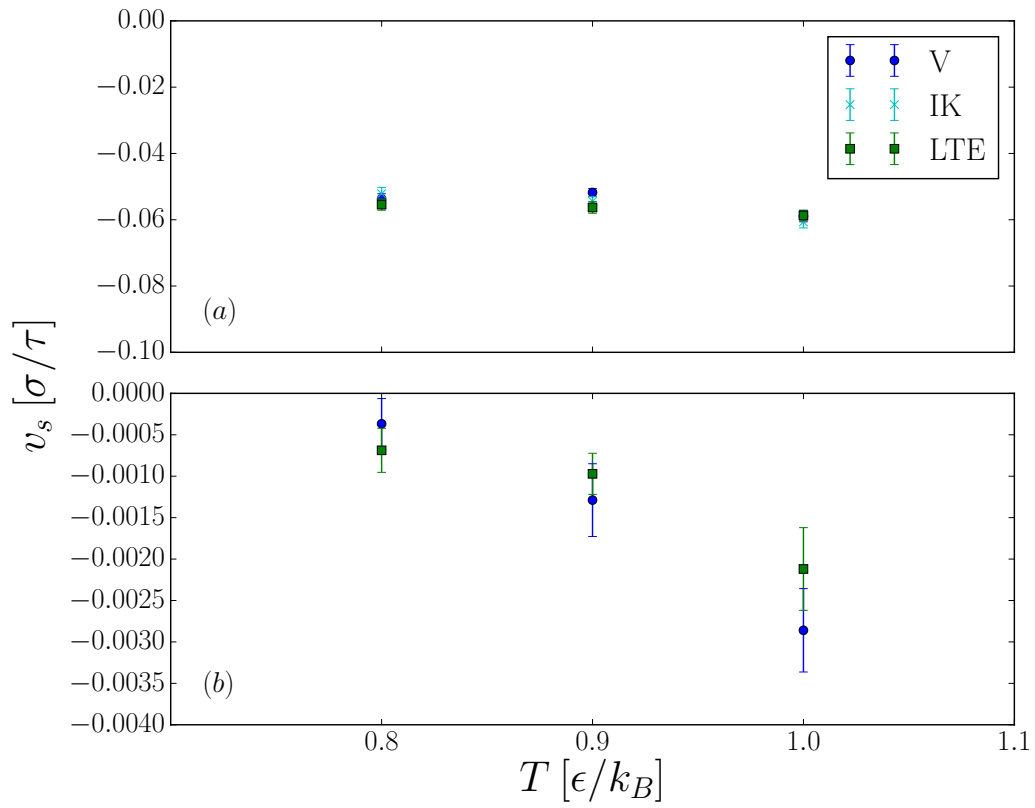


Figure 5.15: Slip velocity as a function of temperature for different wall-fluid interactions: (a) WCA at $\nabla T = 0.0005$ and (b) Lennard-Jones ($\epsilon_{wf} = 0.55\epsilon$) at $\nabla T = 0.003$.

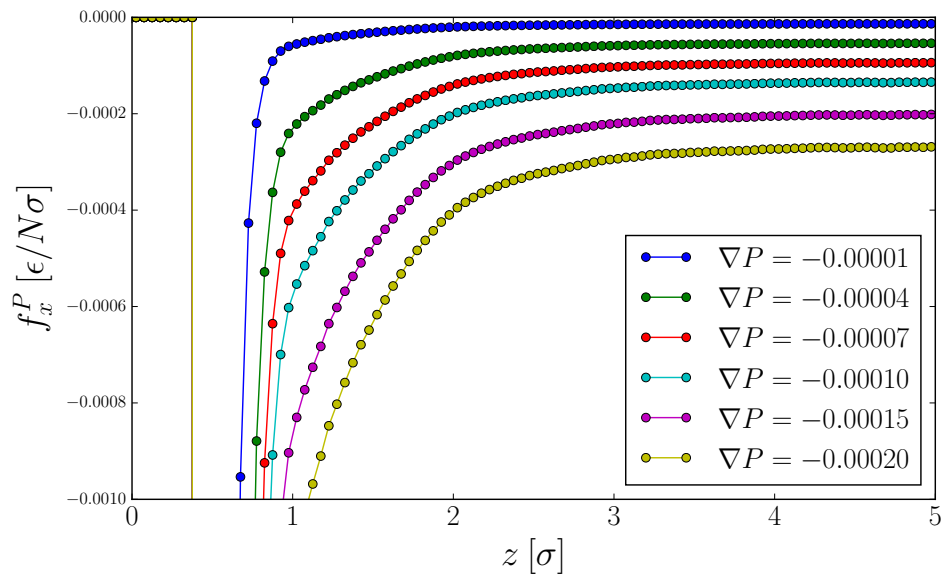


Figure 5.16: Shows the force per particle that must be applied near the WCA surface in order to simulate a uniform ∇P . A range of pressure gradients was tested in separate simulations to determine the extent of the linear regime.

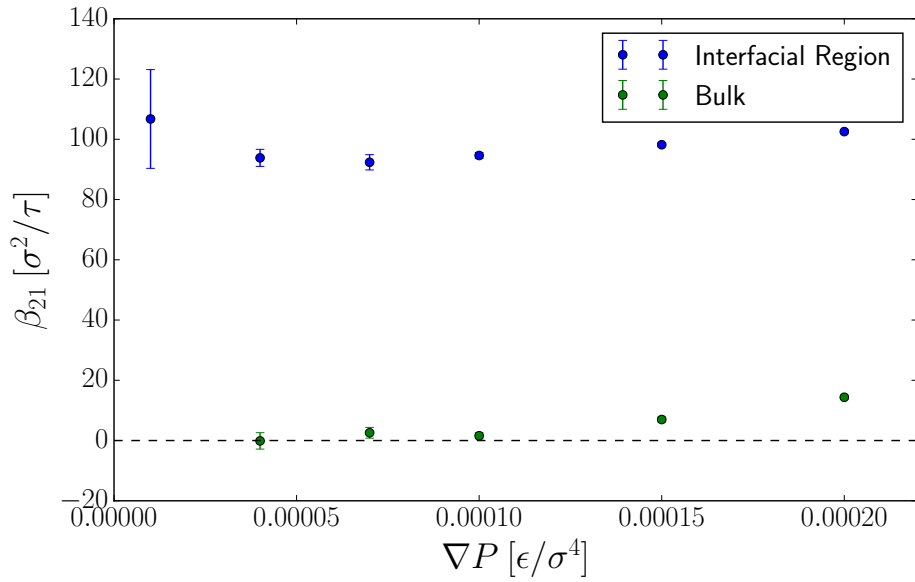


Figure 5.17: Values of the mechano-caloric coefficients β_{21} computed for the gradients shown in 5.16. Blue dots correspond to integration of the excess heat flux from the surface ($z \approx 0$) into the bulk ($z \approx 6$). Within the linear regime, $\beta_{21} \approx 92 - 95$. Green dots correspond to evaluation of Eq. (5.16) in the bulk where, as expected, it is approximately zero.

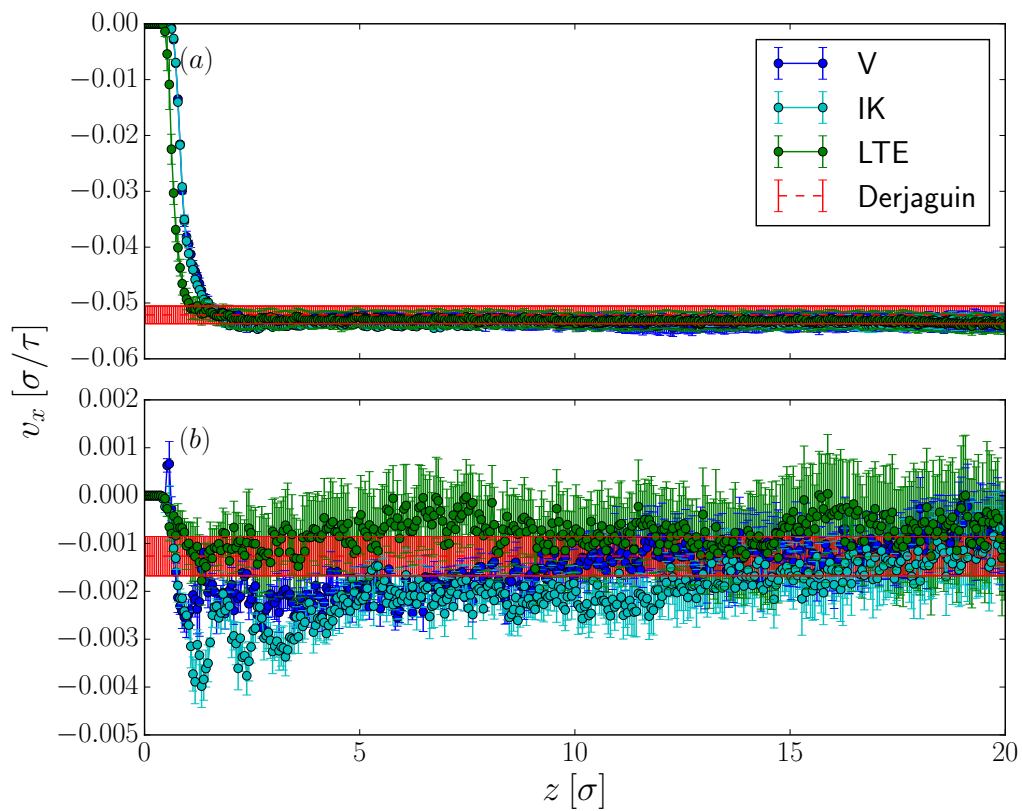


Figure 5.18: Flow profile for (a) WCA wall-fluid interactions at $\nabla T = 0.0005$ and (b) Lennard-Jones ($\epsilon_{wf} = 0.55\epsilon$) wall-fluid interactions at $\nabla T = 0.003$. The flow profiles are computed at $T = 0.9$.

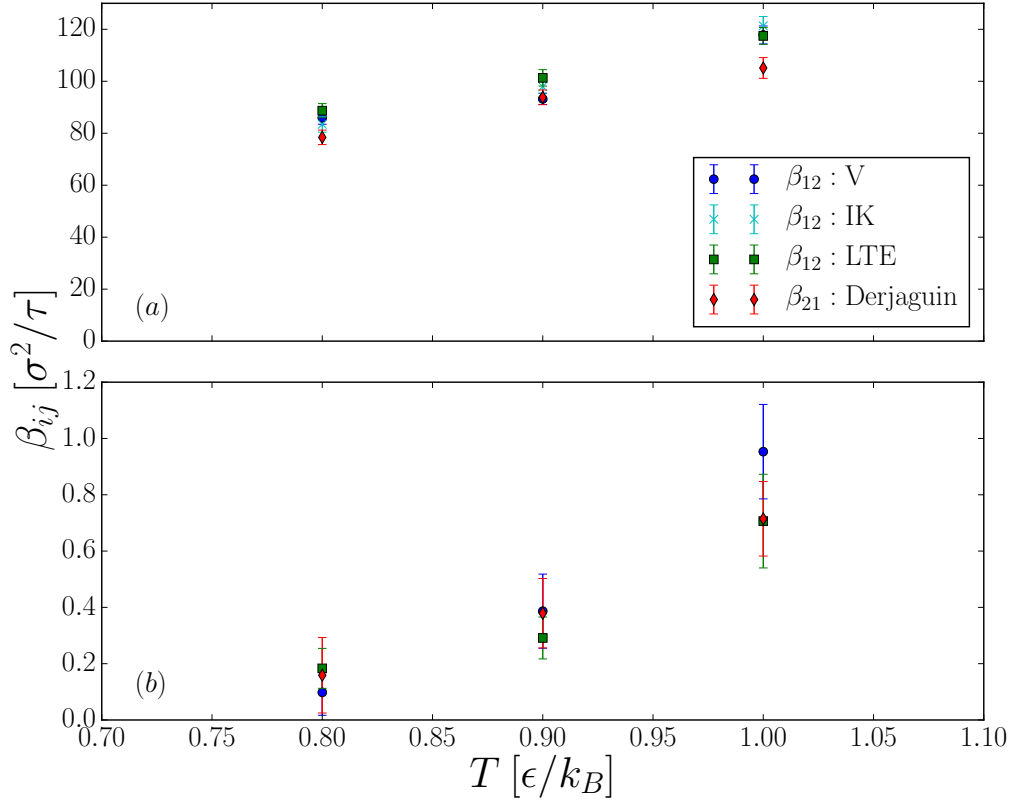


Figure 5.19: Comparison of Onsager reciprocal relations, β_{12} computed via our ‘stress gradient’ (circles, crosses) and LTE (squares) approaches and β_{21} calculated by following Derjaguin’s LNET method (diamonds). Thermo-osmosis coefficients are computed for (a) WCA ($\nabla T = 0.0005$, $\nabla P = 0.00004$) and (b) Lennard-Jones ($\nabla T = 0.003$, $\nabla P = 0.0005$) interactions.

Chapter 6

Direct Approaches

While the method of choice may not matter in regards to calculating the slip velocity, it is clear from Fig. 5.13 that the microscopic pressure expressions and the thermodynamic approach predict significantly different thermo-osmotic force profiles. The question then becomes which, if any, is correct? In this chapter, we formulate a non-equilibrium protocol to answer the preceding question. The work presented in this chapter describes in detail what was published in Ref [23].

6.1 Non-equilibrium Method

As described in Chapter 3, the microscopic pressure expressions suffer from the ambiguity in defining where the potential contribution acts. While the IK expression recovers mechanical force balance normal to the interface, the pressure is formulated by considering the force acting across an artificial plane. The gradient of the IK pressure gives the thermo-osmotic force on the plane. Yet, we are interested in computing the real atomic forces that act on the fluid. Therefore, we expect the gradient of the V pressure to give the cor-

rect answer. The thermodynamic expression is formulated from arguments of local equilibrium and irreversible thermodynamics. As there appears to be no mathematically rigorous derivation of local enthalpy, we cannot conclude that the thermodynamic expression predicts the right answer.

The obvious way to resolve the puzzle is to compute the thermo-osmotic force in a steady-state, non-equilibrium simulation. However, such an approach cannot work, because in steady state the average force on all fluid particles must necessarily vanish: the flow induced by the temperature gradient causes a gradient in shear stress that cancels the thermo-osmotic force [1]

$$\frac{\partial \sigma_{xz}(z)}{\partial z} = -\frac{\partial \sigma_{xx}(z)}{\partial x} \quad (6.1)$$

$$\frac{\partial \sigma_{xx}(z)}{\partial x} = \left(\frac{\partial \sigma_{xx}(z)}{\partial T} \right) \frac{\partial T}{\partial x}. \quad (6.2)$$

Eq. (6.2) is related to Eq. (5.4) by noting that the $\sigma_{\alpha\beta} = -P_{\alpha\beta}$.

To eliminate the shear stress in a non-equilibrium simulation, such that only the thermo-osmotic force remains, we propose the following non-equilibrium simulation technique: first, the system shown in Fig. 6.1 is equilibrated to an NPT ensemble ($T \approx 0.9, P \approx 0.122$) by using a Nosé-Hoover thermostat and applying a downward force to the top wall. In short, the system is equilibrated to the same thermodynamic conditions described in Chapter 5.4.

After equilibration, the thermostat is switched off so that the system now samples an NPH ensemble. Next, we impose a periodic temperature gradient along x using the temperature rescale algorithm (see Chapter 4.3.3). We thermostat the left-most part of the simulation box ($x = 0.0 - 1.644$) at a temperature lower than the average ($T = 0.9$) while also thermostating the middle of the simulation box ($x = 24.66 - 26.31$) at a temperature higher

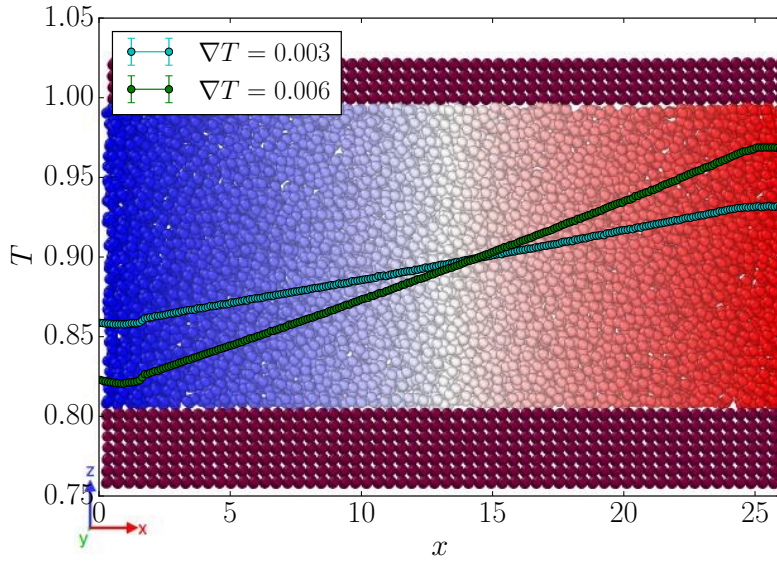


Figure 6.1: Simulation box used for non-equilibrium force calculation where fluid near the bottom interacts with a structured wall. Temperature profiles for the simulation are plotted over the box.

than the average. The resulting heat current sets up the thermal gradient as shown in Fig. 6.2.

After the system has reached steady-state, we change the equations of motion for the fluid atoms: in particular, we now treat the mass M of the fluid particles as a tensor in the Hamiltonian, and consider the limit where $M_{yy} = M_{zz} = M$, the original mass of the particles, whilst $M_{xx} \rightarrow \infty$. The Velocity Verlet integration (see Chapter 4.1) changes in the following way:

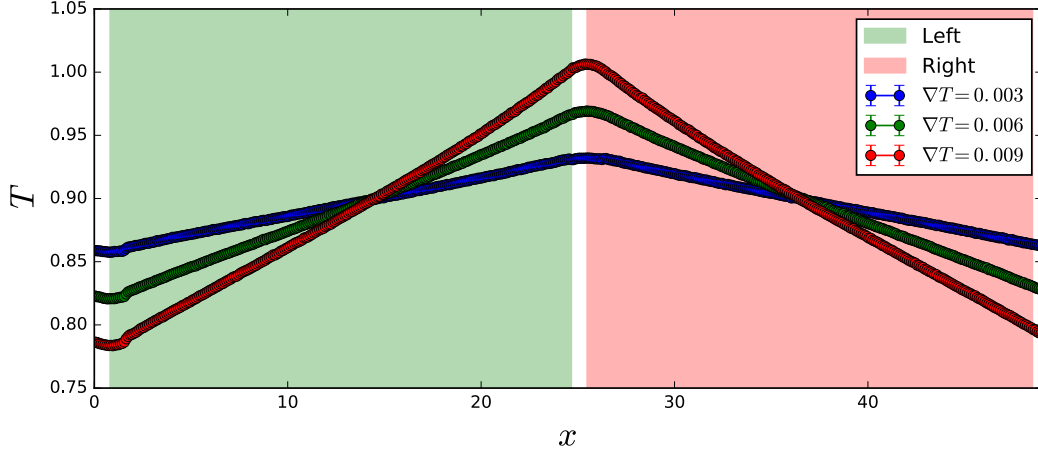


Figure 6.2: Temperature profiles computed from the non-equilibrium simulations. Since particle motion is only constrained in x , the temperature gradient is left unchanged. Left ($x = 0.82207 - 24.6621$) and Right ($x = 25.48417 - 48.50213$) denote sampling regions where the thermo-osmotic force is measured. The bounds for these regions are chosen so that they coincide with the lattice positions of solid atoms.

In the first half-step,

$$\begin{aligned}
 v_x \left(t + \frac{\Delta t}{2} \right) &= 0 \\
 v_y \left(t + \frac{\Delta t}{2} \right) &= v_y(t) + \frac{f_y(t)}{2M_{yy}} \Delta t \\
 v_z \left(t + \frac{\Delta t}{2} \right) &= v_z(t) + \frac{f_z(t)}{2M_{zz}} \Delta t \\
 x(t + \Delta t) &= x(t) \\
 y(t + \Delta t) &= y(t) + v_y \left(t + \frac{\Delta t}{2} \right) \Delta t \\
 z(t + \Delta t) &= z(t) + v_z \left(t + \frac{\Delta t}{2} \right) \Delta t
 \end{aligned}$$

In the second half-step,

$$\begin{aligned}
v_x(t + \Delta t) &= 0 \\
v_y(t + \Delta t) &= v_y\left(t + \frac{\Delta t}{2}\right) + \frac{f_y(t + \Delta t)}{2M_{yy}}\Delta t \\
v_z(t + \Delta t) &= v_z\left(t + \frac{\Delta t}{2}\right) + \frac{f_z(t + \Delta t)}{2M_{zz}}\Delta t
\end{aligned}$$

Transforming the Hamiltonian in this way changes the dynamics of the system, but static properties such as inter-molecular interactions remain the same. As temperature remains finite, $v_x \rightarrow 0$ for all fluid atoms:

$$v_x = \sqrt{\frac{k_B T}{M_{xx}}}, \quad (6.3)$$

In other words, we have switched off the shear flow, whilst maintaining the temperature gradient.

Yet, fluid atoms are still diffusing in the y and z directions. In equilibrium, equipartition would still hold in this model system: hence, the average kinetic energy associated with motion in the x direction is still $k_B T/2$. As shown in Fig. 6.2, the temperature gradient is invariant to changing the equations of motion. In this stationary system, the bulk serves as a reservoir of atoms so that fluid near the surface can rearrange to the local-equilibrium density profiles. As the gradient in shear stress $\partial\sigma_{xz}(z)/\partial z$ now vanishes, only the thermo-osmotic force will remain.

Note, that the density profile, $\rho(x)$, for the stationary system will greatly depend on the instantaneous density profile before setting $v_x = 0$. Thus, in order for each reservoir Δx_i along x to sample an NPT ensemble, we must average the force calculation over at least 100 different initial configurations. As shown in Fig. 6.3, ensemble averaging will cause the density profile in

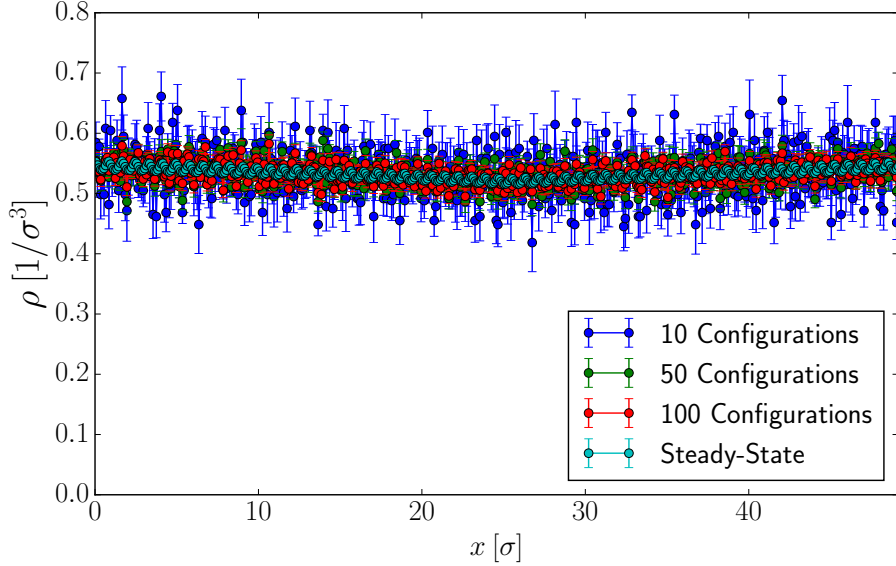


Figure 6.3: Density profiles for $\nabla T = 0.003$ (blue in Fig. 6.2) of the constrained system averaged over 10 (blue), 50 (green), 100 (red) different initial configurations. Ensemble averaging over more configurations causes the density profile in the system where $v_x \rightarrow 0$ to approach the steady-state profile (cyan).

the system where $v_x \rightarrow 0$ to approach the steady-state density profile in the unconstrained system.

6.2 Results

6.2.1 Structured Walls

In the direct, non-equilibrium measurement discussed in Section 6.1, we consider a fluid consisting of $N = 7920$ atoms interacting via a truncated and shifted Lennard-Jones potential given by Eq. (5.18). The fluid is in contact with the same surfaces discussed in Chapter 5.4: a structured wall interacting with fluid through a less attractive Lennard-Jones potential and another in-

interacting via a purely repulsive Weeks-Chandler-Andersen (WCA) potential as shown in Fig. 6.1. The Lennard-Jones parameters determining fluid-fluid, fluid-solid, and solid-solid interactions are described in Chapter 5.4.

Fig. 6.1 shows a simulation cell of length $\langle L_x \rangle = 49.32\sigma$ and $\langle L_y \rangle = 9.86\sigma$ containing fluid that interacts with a structured wall. To ensure that $P = 0.122$ in the bulk, the top wall acts as a piston that is free to move in the x - and z -directions. When comparing the directly computed thermo-osmotic force in the non-equilibrium simulation with the force predicted by the ‘stress gradient’ and LTE methods, we should note that the direct calculation will only include the gradient of the potential contribution to the pressure tensor

$$f_x^{P,\phi}(z) = -\frac{1}{\rho(z)} \left(\frac{\partial P_{xx}^\phi(z)}{\partial T} \right) \left(\frac{\partial T}{\partial x} \right) \quad (6.4)$$

since the force computation will simply be a summation over all pairwise forces.

Yet, as discussed in Chapter 3.1, the non-uniqueness of microscopic pressure arises due to different definitions of the *potential* contribution not the kinetic. The kinetic pressure gradient is given by

$$f_x^{P,k}(z) = -\frac{1}{\rho(z)} \left(\frac{\rho(z, T_2)k_B T_2 - \rho(z, T_1)k_B T_1}{T_2 - T_1} \right) \left(\frac{\partial T}{\partial x} \right) \quad (6.5)$$

We can use equilibrium measurements of the kinetic contribution to the pressure at different temperatures to compute Eq. (6.5). Fig. 6.4(a, b) shows calculations of the kinetic pressure and the gradient at $T = 0.9$, respectively. Adding the kinetic pressure gradient to the direct calculation should give the full thermo-osmotic force.

Using the method described in Section 6.1, we compute the force per particle in the system where $M_{xx} \rightarrow \infty$ and $v_x \rightarrow 0$. The force profile is

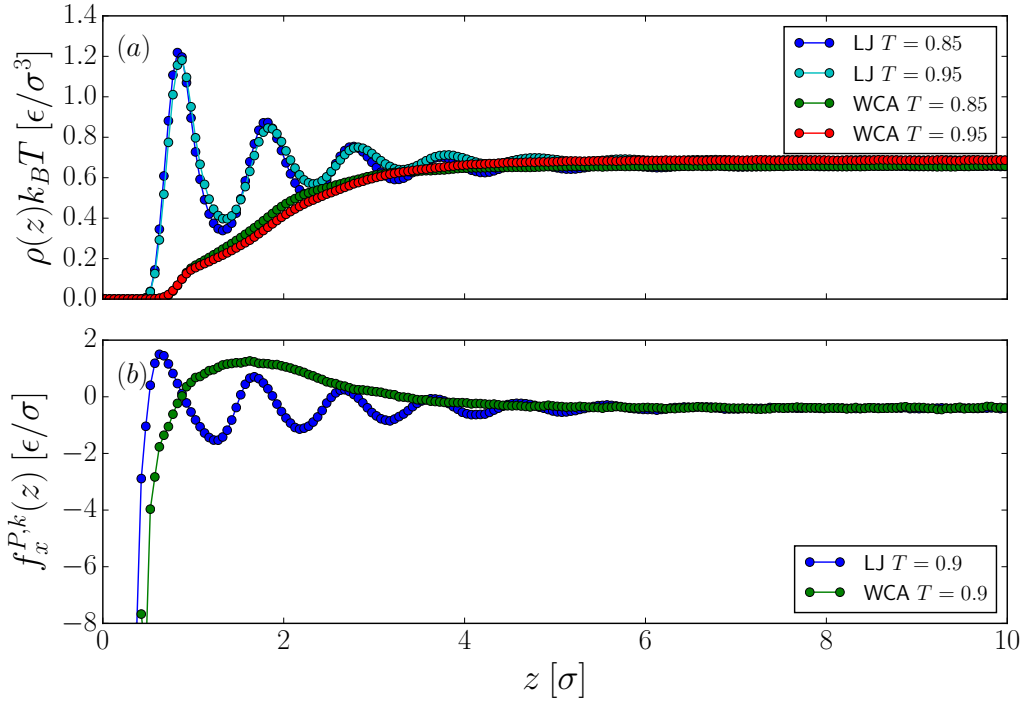


Figure 6.4: (a) Ideal contribution to the pressure at $T = 0.85$ and $T = 0.95$ for Lennard-Jones and WCA walls are used to compute the (b) kinetic force per particle given by Eq. (6.5) at $\nabla T = 1$.

measured in the left (green in Fig. 6.2) where $\nabla T > 0$ and right region (red in Fig. 6.2) where $\nabla T < 0$. Figs. 6.5 and 6.6 show direct calculations of the force near Lennard-Jones and WCA surfaces, respectively. Encouragingly, the force profiles in the left and right regions are mirror images of each other. Moreover, it is clear from Fig. 6.6 that doubling the temperature gradient doubles the force.

To improve statistics, the non-equilibrium forces from the left and right regions shown in Figs. 6.5 and 6.6 were averaged. Adding the profiles of $f_x^{P,\phi}(z)$ to $f_x^{P,k}(z)$ (Fig. 6.4(b)) at the corresponding ∇T gives the total thermo-osmotic force. The total force is shown by the blue curves in Figs. 6.7 and 6.8. As expected, the thermo-osmotic force is a monotonically increasing

function of the gradient.

Figs. 6.7 and 6.8 compare the force per particle predicted by the stress gradient (cyan, red) and LTE methods (green) with those computed directly via the non-equilibrium technique (blue). Surprisingly, in all cases, both the V (red) and IK (cyan) pressure gradients fail to predict the thermo-osmotic force (blue). Perhaps more significantly, the LTE approach (green) gets extremely close, but still differs from the non-equilibrium result (blue). It is possible that this discrepancy is due to deviation of the non-equilibrium result from the local thermal equilibrium approximation. Encouragingly, all methods agree in predicting zero net force in the bulk, consistent with the theory (Eq. (2.9)).

6.2.2 Wall Stress

The failure of both pressure expressions is surprising and demands further analysis. In the previous section, we assume that the structure of the confining solid does not depend on temperature. Symmetry then implies that, on average, a flat solid wall exerts zero net transverse force on a fluid atom, suggesting that the wall potential should not contribute to the thermo-osmotic force. Yet, the mechanical expressions contradict the latter conjecture. Consider Eq. (5.7) while separating fluid-fluid and wall-fluid atomic interactions

$$P_{xx}^{V,\phi}(z) = -\frac{1}{2V(z)} \left(\left\langle \sum_i^{N(z)} \sum_{j \neq i}^{N_f} \frac{x_{ij}^2}{r_{ij}} \phi'_{ff}(r_{ij}) \right\rangle + \left\langle \sum_i^{N(z)} \sum_{j \neq i}^{N_w} \frac{x_{ij}^2}{r_{ij}} \phi'_{wf}(r_{ij}) \right\rangle \right) \quad (6.6)$$

where the subscripts f and w denote fluid and wall atoms, $\phi_{ff}(r_{ij})$ and $\phi_{wf}(r_{ij})$ are the fluid-fluid and wall-fluid interaction potentials. Differentiat-

ing the term containing $\phi'_{wf}(r_{ij})$ with respect to T gives

$$\frac{\partial P_{xx}^{V,\phi_{wf}}(z)}{\partial T} = \frac{\partial}{\partial T} \left(-\frac{1}{2V(z)} \left\langle \sum_i^{N(z)} \sum_{j \neq i}^{N_w} \frac{x_{ij}^2}{r_{ij}} \phi'_{wf}(r_{ij}) \right\rangle \right). \quad (6.7)$$

The first summation over $N(z)$ is equivalent to the density of fluid atoms at height z . Clearly, the fluid density will change when the temperature changes. The second summation over N_w will certainly not change since the number of wall atoms stays constant. Yet, due to the temperature dependence of the first summation, substituting Eq. (6.7) into Eq. (5.5) results in an unexpected force contribution from the wall. The same analysis applies equally well to the IK pressure. In that case, the gradient in momentum flux per unit area from the wall across an artificial plane will be non-zero.

Rather than summing over all intermolecular interactions to compute the force, Fig. 6.9(b) shows the resulting force if only wall-fluid interactions ϕ_{wf} in the Right region (Fig. 6.2) are summed. As a test case, the same force was measured in equilibrium simulations (blue circles) while $v_x \rightarrow 0$. Surprisingly, from $z = 0.8 - 1.4$, there appears to be a significant force exerted by the wall on the fluid that scales linearly with the gradient. Below $z = 0.8$, the signal becomes poor and the calculation needs to be averaged over many more initial configurations. To account for the unexpected wall forces shown in Fig. 6.9(b), we consider the possibility that due to the density gradient induced by the thermal gradient, the average center-of-mass x -position (Fig. 6.9(a)) of a fluid atom (red spheres) in each slab dz is asymmetric with respect to the lattice positions of the solid atoms (yellow spheres) below. Fig. 6.9(a) shows the average x -position of an atom as a function of z in the equilibrium (blue circles) and non-equilibrium simulations (green, red, cyan circles).

As expected, in equilibrium, the center-of-mass position of a fluid atom in the Right region ($x = 25.48 - 48.50$) is located at the center of the region $x = 36.99$, also the lattice position of a solid atom. Out of equilibrium, the average position shifts away from the center in a way that scales linearly with the gradient and breaks symmetry. The force profile in Fig. 6.9(b) is consistent with the position shift shown in Fig. 6.9(a), as the fluid atom experiences a negative force where it is shifted right ($z = 0.8 - 1.0$), zero force at $z = 1.075$ where there is no shift, and a small positive force where it is shifted left ($z = 1.1 - 1.4$). As expected, the wall force decays extremely quickly. Perhaps surprisingly, the potential stress gradient shown in Fig. 6.9(c) predicts wall forces that are opposite in sign to the actual values (Fig. 6.9(b)) and decay slowly. It seems that wall contributions to the pressure gradient given by Eq. (6.7) (Fig. 6.9(c)) predict excess forces that in reality do not exist (Fig. 6.9(b)).

In the case of a surface that attracts some of the fluid, wall contributions to the stress gradient are significant. It is likely in the case of a WCA surface, fluid will on average be sufficiently far away such that the wall force will become exceedingly small.

6.2.3 Flat Wall

Based on the findings in the previous section, perhaps the pressure expressions can predict the correct answer if transverse force contributions from the wall were removed, that is, if $\partial\phi_{wf}/\partial x = 0$ in Eq. (6.7). The simplest way to test this idea is to consider fluid interacting with a flat, unstructured surface at $z = 0$ as shown in Fig. 6.10. This wall simply flips the sign of v_z if fluid atoms attempt to cross the surface. Fig. 6.11(a) shows that the equilibrium density profile monotonically increases from the surface into the

bulk, similar to the case of a WCA surface (Fig. 5.7). Yet, because fluid may still cross the surface, the density at $z = 0$ is non-zero.

As before, the force per particle is computed via the stress gradient (see Chapter 5.1) and thermodynamic (see Chapter 5.2) methods and shown in Fig. 6.11(b). Consistent with our previous results, the mechanical and thermodynamic approaches predict different answers for the thermo-osmotic force.

Using the direct, non-equilibrium approach described in Chapter 6.1, we can measure the thermo-osmotic force near the reflective surface. Fig. 6.12(a) shows evaluation of Eq. (6.4) via the direct method. As expected, the profiles are approximately mirror images of each other across the z - plane. Surprisingly, Fig. 6.12(b) shows that the V (red) and IK (cyan) pressure gradients fail to predict the thermo-osmotic force (blue) even in the case of a flat surface, while the thermodynamic approach (green) gets close. Therefore, failure of the pressure gradient route cannot simply be attributed to wall contributions to the thermo-osmotic force given by Eq. (6.7) and shown in Fig. 6.9(c). The results for a flat surface point to a different explanation on why pressure expressions fail.

In related work, there was consistent numerical evidence indicating that pressure gradients fail to predict microscopic Marangoni [40] and diffusio-osmotic [41] forces (see Appendix 9.4). Therefore, we have shown in multiple cases that near an interface, microscopic forces cannot be expressed as the gradient of the pressure tensor.

We attempt to explain the failure of the pressure gradient route by revisiting the assumptions made in formulating the atomic pressure expressions. In deriving the transverse virial pressure (see Chapter 3.1.3), we differentiate the free energy of a thin slab with respect to volume expansion in x as

shown in Fig. 3.3. In doing so, we carry out the volume expansion of the slab while fixing the remaining volume in the system. Within a slab in the bulk fluid, intermolecular forces are isotropic so that it makes no difference whether we differentiate the free energy of the entire system or the slab with respect to a volume expansion. Inside a slab near the surface, forces are anisotropic, which may indeed make a significant difference. In regards to Irving-Kirkwood, the IK pressure gradient yields forces on artificial surfaces rather than on atoms. Therefore, it is difficult to determine how the non-equilibrium calculation, which measures forces on atoms, can be derived from the IK expression. Additionally, we should note that because the virial and Harasima expressions for the transverse pressure are equivalent (see Chapter 3.1.2), simply choosing a different contour does not resolve the problem.

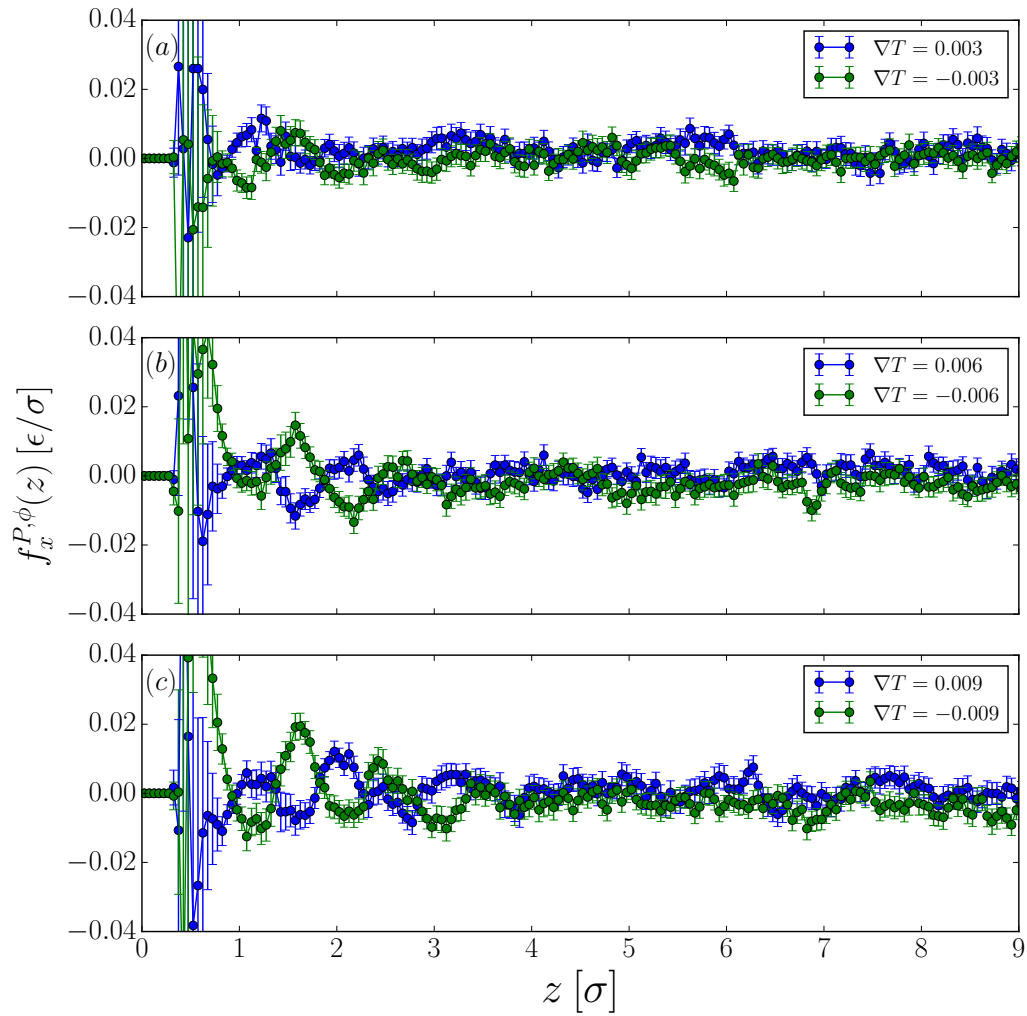


Figure 6.5: Direct calculation of the potential contribution to the pressure gradient (Eq. (6.4)) near a Lennard-Jones surface. Measurements are carried out for (a) $\nabla T = 0.003$ (b) $\nabla T = 0.006$ and (c) $\nabla T = 0.009$.

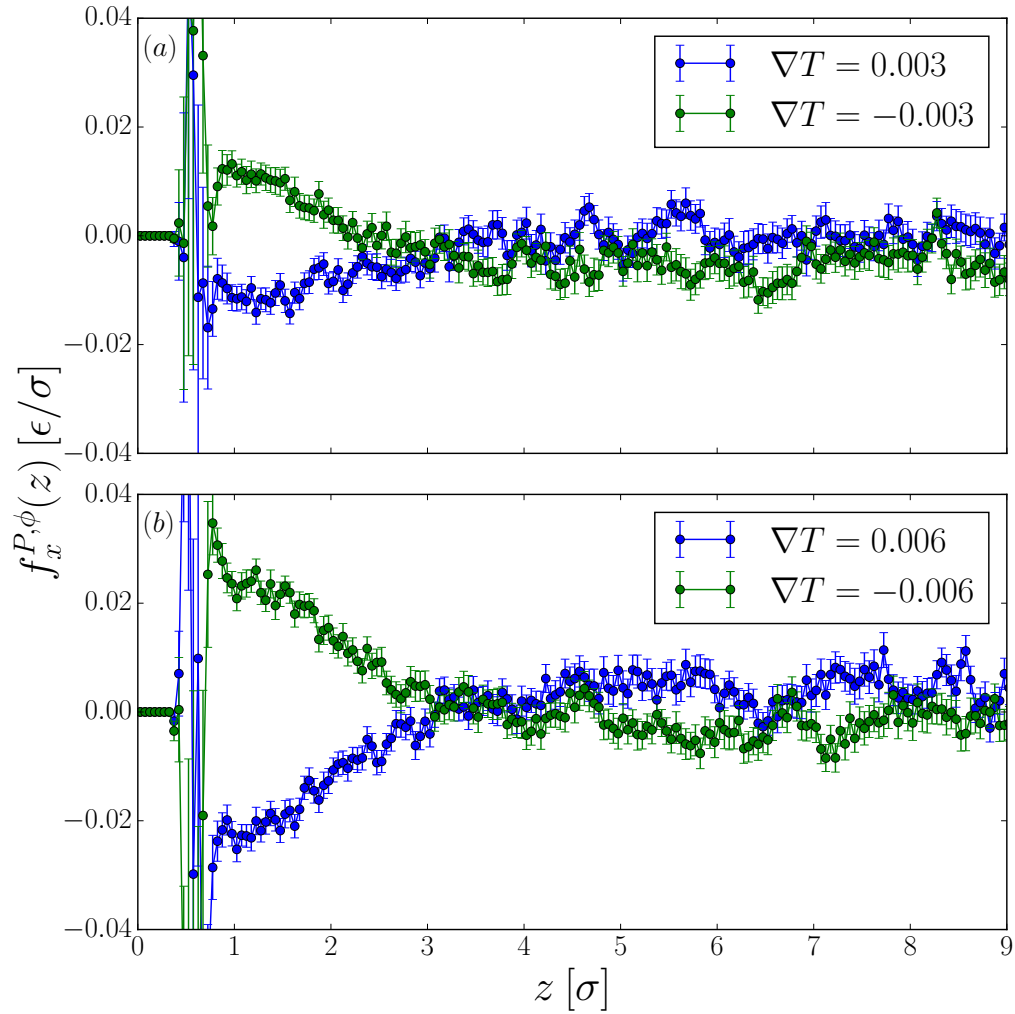


Figure 6.6: Direct calculation of the potential contribution to the pressure gradient (Eq. (6.4)) near a WCA surface. Measurements are carried out for (a) $\nabla T = 0.003$ and (b) $\nabla T = 0.006$.

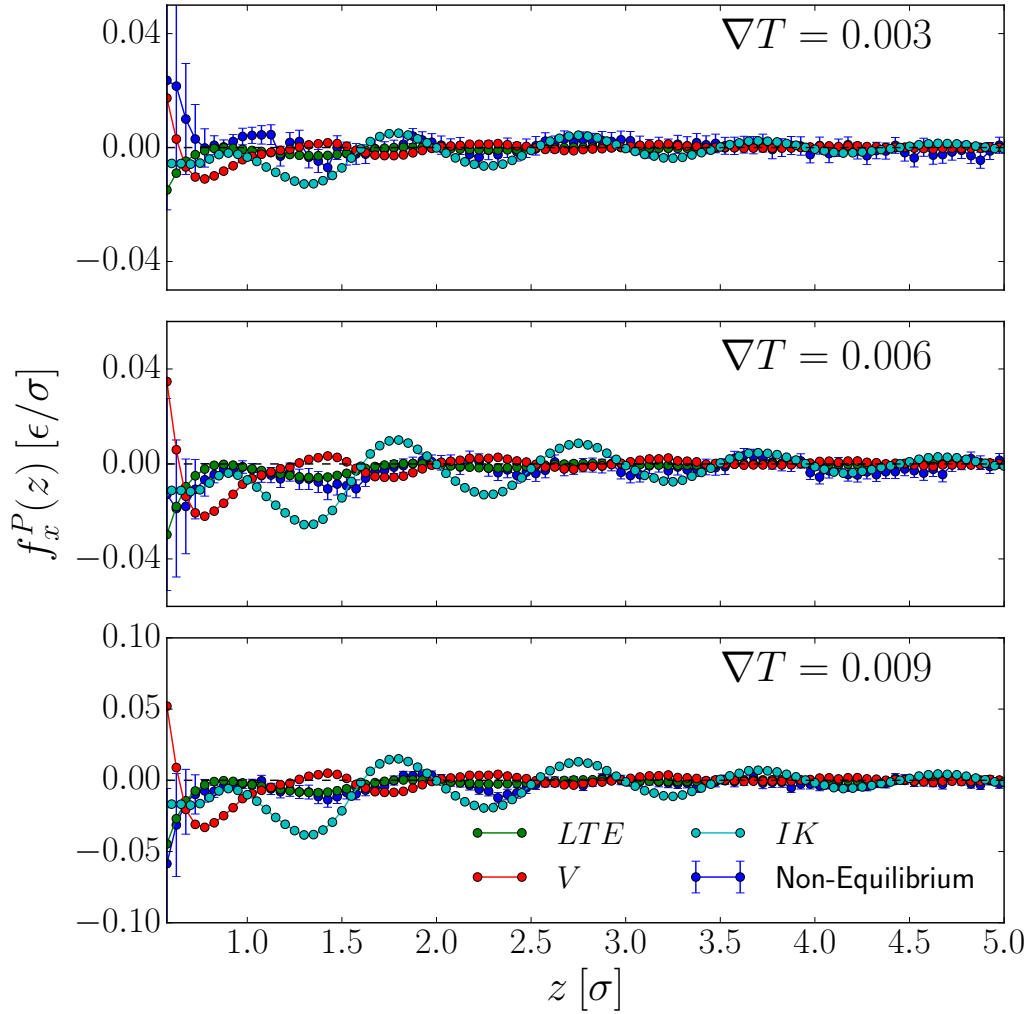


Figure 6.7: Comparison of non-equilibrium force measurement (blue) with ‘stress gradient’ approaches (cyan, red) and LTE approach (green) for the structured Lennard-Jones wall. Below $z = 0.575$, the fluid density is less than 10% of the bulk giving poor statistics.

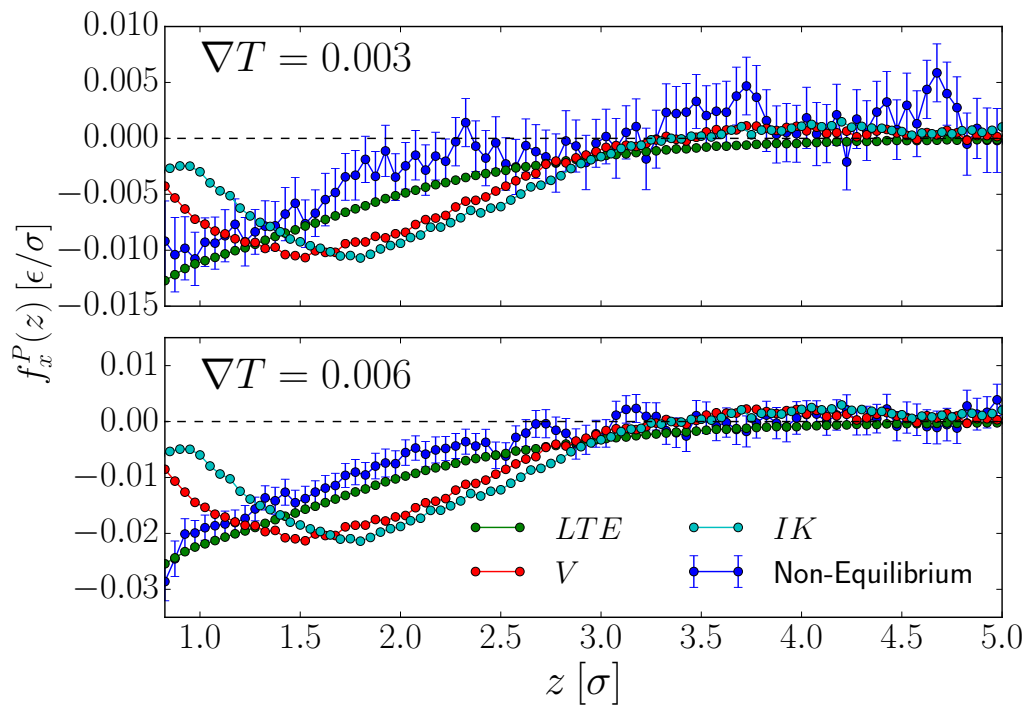


Figure 6.8: Comparison of non-equilibrium force measurement (blue) with ‘stress gradient’ approaches (cyan, red) and LTE approach (green) for the structured WCA wall. Below $z = 0.825$, the fluid density is less than 10% of the bulk giving poor statistics.

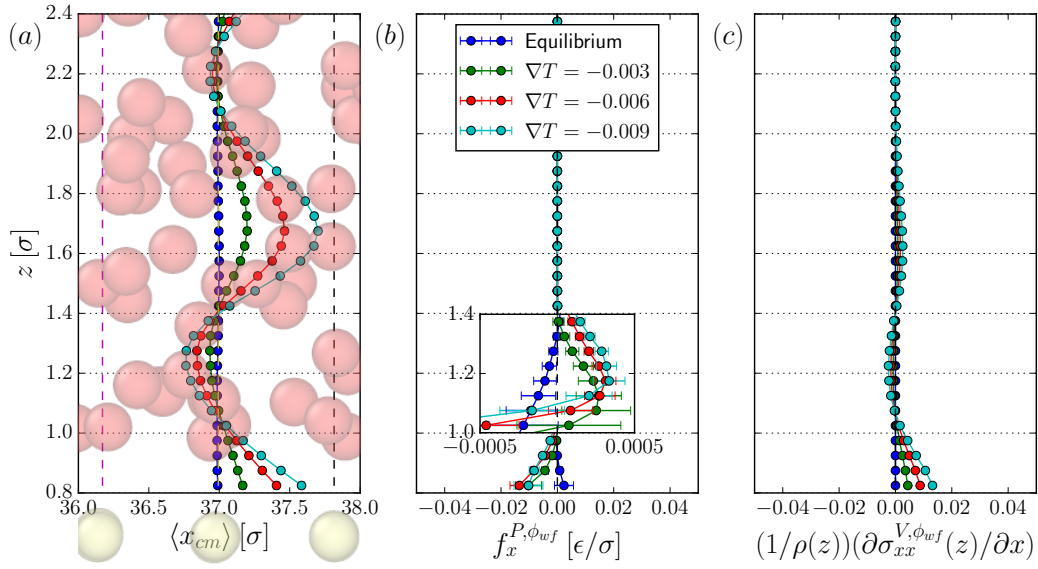


Figure 6.9: (a) shows the average center-of-mass $\langle x_{cm} \rangle$ position of fluid atoms (red spheres) in the Right region of Fig. 6.2 as a function of the height z from the surface located at $z = 0$. The temperature gradient causes the center of mass to shift away from the equilibrium position ($\langle x_{cm} \rangle = 36.99$, blue circles), which is symmetric with respect to the lattice positions of solid atoms (yellow spheres). The shift (green, red, cyan circles) is proportional to the magnitude of the gradient. (b) shows the non-equilibrium calculation of the wall force induced by the center of mass shift shown in (a). (c) shows the wall force predicted by the ‘stress gradient’ method.

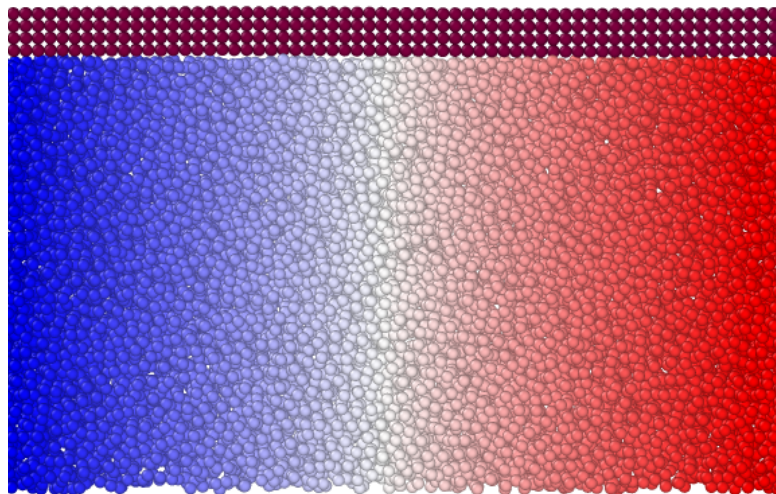


Figure 6.10: Simulation box used for non-equilibrium force calculation where fluid near the bottom interacts with a flat, reflective surface.

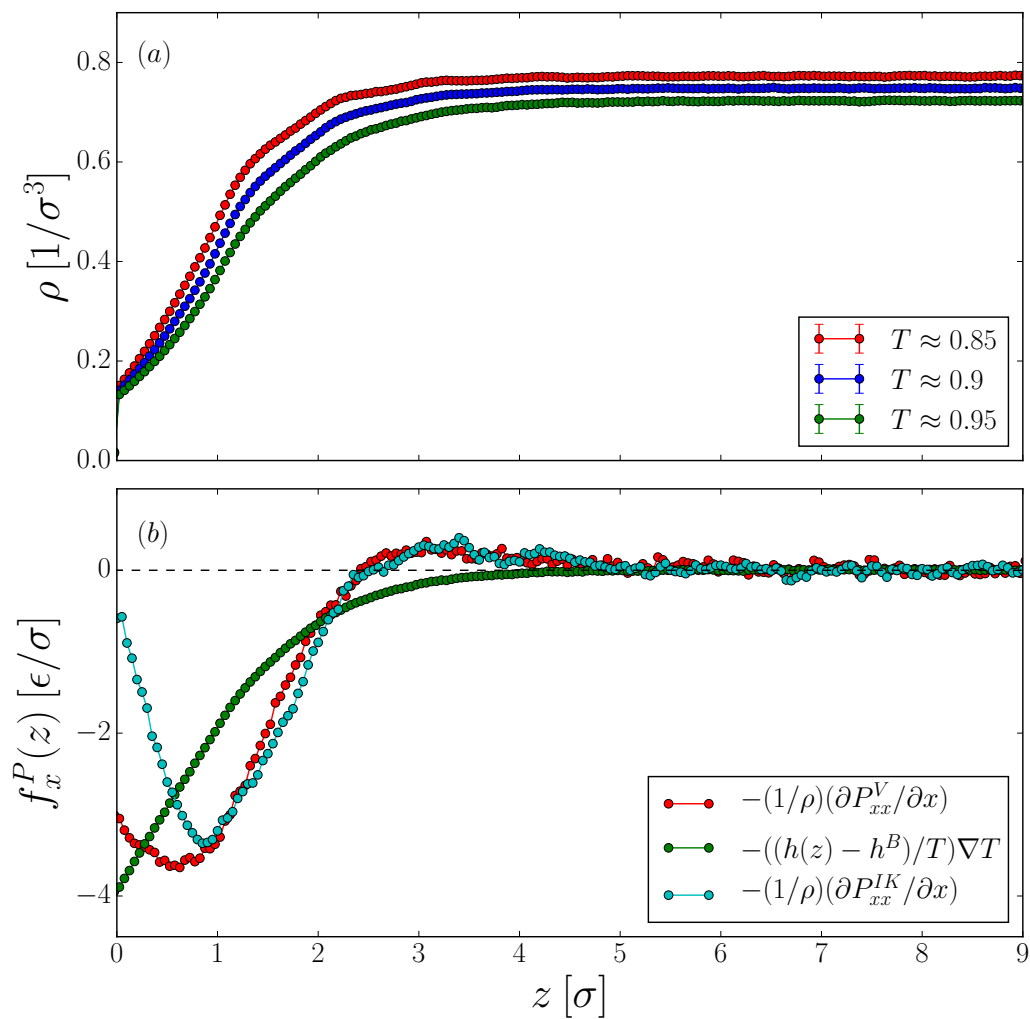


Figure 6.11: (a) Density profiles at different temperatures of fluid interacting with a flat, reflective wall. (b) The thermo-osmotic force per particle at $T = 0.9$ for $\nabla T = 1.0$. The stress gradient methods, computed via Eq. (5.5), predicts the force profile shown in red and cyan while the thermodynamic method Eq. (5.14) predicts the profile shown in green.

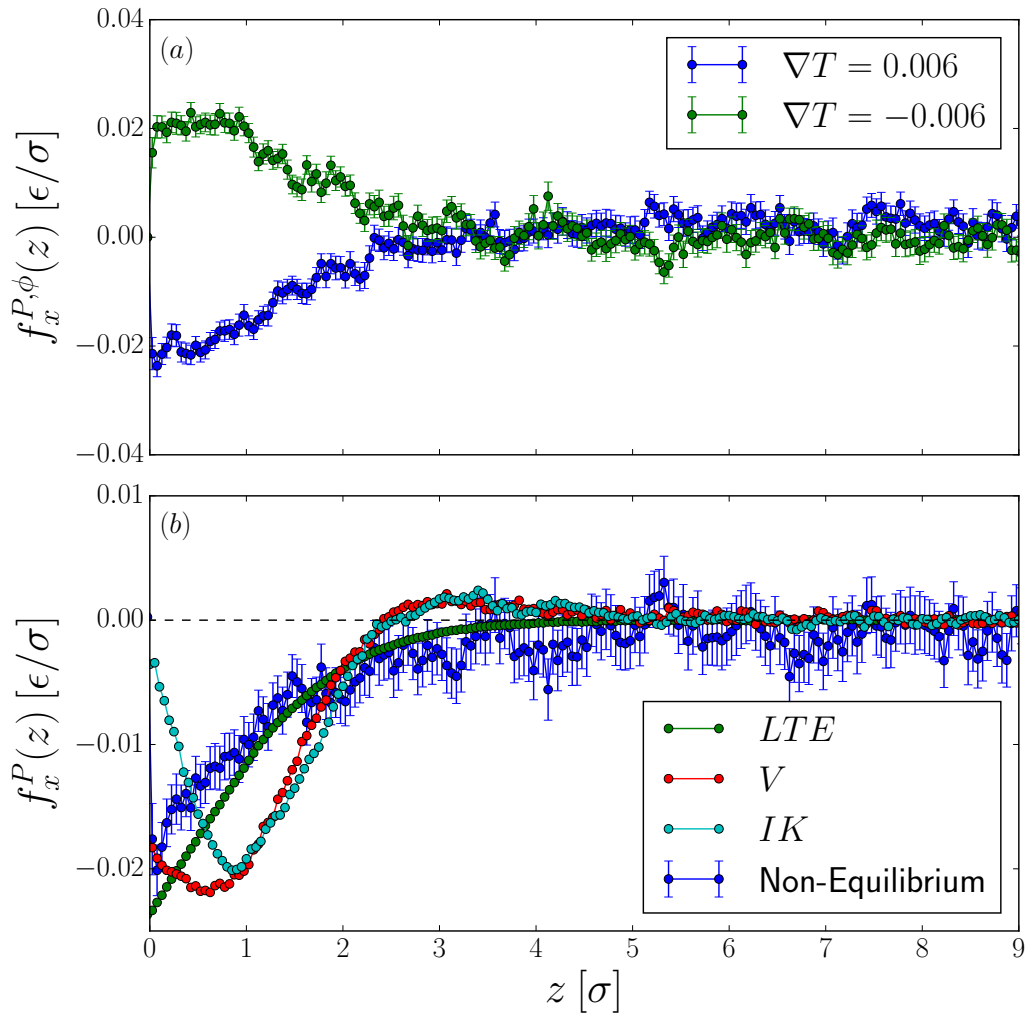


Figure 6.12: (a) Calculation of $f_x^{P,\phi}$ using the direct, non-equilibrium method for the setup shown in Fig. 6.10. (b) Comparison of the force profiles using the non-equilibrium (blue), LTE (green), and stress gradient (red, cyan) methods at $\nabla T = 0.006$.

Chapter 7

Surface Tension Gradients

In the previous chapter, we established for three distinct surfaces that pressure gradients derived from the virial and Irving-Kirkwood expressions fail to predict thermo-osmotic forces. Yet, in Fig. 5.18, especially in the case of a purely repulsive surface, all methods predict the same thermo-osmotic slip velocity. While pressure gradients clearly fail to predict the correct force and flow profile, in certain cases they manage to give an accurate estimate of the slip velocity. It is therefore possible that on a macroscopic scale, pressure gradients can predict the right answer.

7.1 Kirkwood & Buff

The limited success of the pressure gradient approach can be attributed to the fact that both mechanical and thermodynamic expressions predict the same surface tension gradient. We start by closely examining the mechanical definition of surface tension. Kirkwood and Buff [37] consider an interface dividing homogeneous phases α and β where the pressure tensor reduces to the hydrostatic pressure multiplied by the unit tensor in the bulk. Then,

they consider a strip of unit width in y extending from $-l/2$ to $l/2$ in z [51].

The total stress acting in the x direction across the strip is

$$\Delta\Sigma_x = - \int_{-l/2}^{l/2} P_T(z)dz. \quad (7.1)$$

In the absence of an interface, the stress acting across the strip would simply be $-Pl$ where P is the hydrostatic pressure. The excess stress due to the interface gives the surface tension

$$\gamma = - \int_{-l/2}^{l/2} P_T(z)dz + Pl = \int_{-l/2}^{l/2} P - P_T(z)dz. \quad (7.2)$$

The surface tension is independent of l provided that $P_T(z) = P$ at $z = -l/2$ and $z = l/2$. Furthermore, the Irving-Kirkwood normal pressure, P_N , is independent of z and equal to P . With these added considerations, Eq. (7.2) reduces to Eq. (3.52) (see Chapter 3.2). However, since P_N of the virial pressure does depend on z , we use Eq. (7.2) to avoid any ambiguity.

We should note that the stress integral given by Eq. (7.2) gives the surface tension if the bulk phases α and β are homogeneous. Yet, in the case of a structured solid surface interacting with the fluid, the transverse pressure will oscillate as a function of z due to the lattice spacing between solid atoms. These oscillations in the bulk solid phase would incorrectly contribute to the surface tension integral. Therefore, Eq. (7.2) does not give the surface tension across solid-fluid interfaces.

Differentiating Eq. (7.2) gives

$$\frac{\partial\gamma}{\partial x} = - \int_{-\infty}^{\infty} \frac{\partial P_{xx}(z)}{\partial x} dz. \quad (7.3)$$

Therefore, integrating the pressure gradient derived from microscopic ex-

Surface Tension Gradients

	Lennard-Jones	WCA	Specular
LTE	-0.57 ± 0.01	-1.78 ± 0.01	-1.71 ± 0.01
V	-1.15 ± 0.02	-1.74 ± 0.07	-1.72 ± 0.02
IK	-1.39 ± 0.04	-1.74 ± 0.07	-1.71 ± 0.01

Table 7.1: Predictions of the surface tension gradient by the mechanical and thermodynamic methods for the three surfaces described in Chapter 6.

pressions would give the total mechanical prediction of the surface tension gradient.

The thermodynamic definition of the surface tension gradient is given by differentiating the Gibbs-Adsorption relation (see Chapter 2.2):

$$\frac{\partial\gamma}{\partial x} = - \int_{-\infty}^{\infty} dz \left(\frac{\Delta h(z)}{T} \right) \left(\frac{\partial T}{\partial x} \right). \quad (7.4)$$

Eq. (7.4) can be numerically evaluated by integrating the volume force predicted by the LTE approach.

7.2 Results

We can numerically test whether Eq. (7.3) and Eq. (7.4) predict the same surface tension gradient. Fig. 7.1(a, b) show the force density predicted by the mechanical and thermodynamic expressions for Lennard-Jones and WCA walls, respectively. Integration of the *V* and *IK* force profiles gives mechanical predictions of the surface tension gradient (Eq. (7.3)) and integration of the *LTE* profile gives the thermodynamic prediction (Eq. (7.4)). Table 7.1 shows the surface tension gradient predicted by different methods.

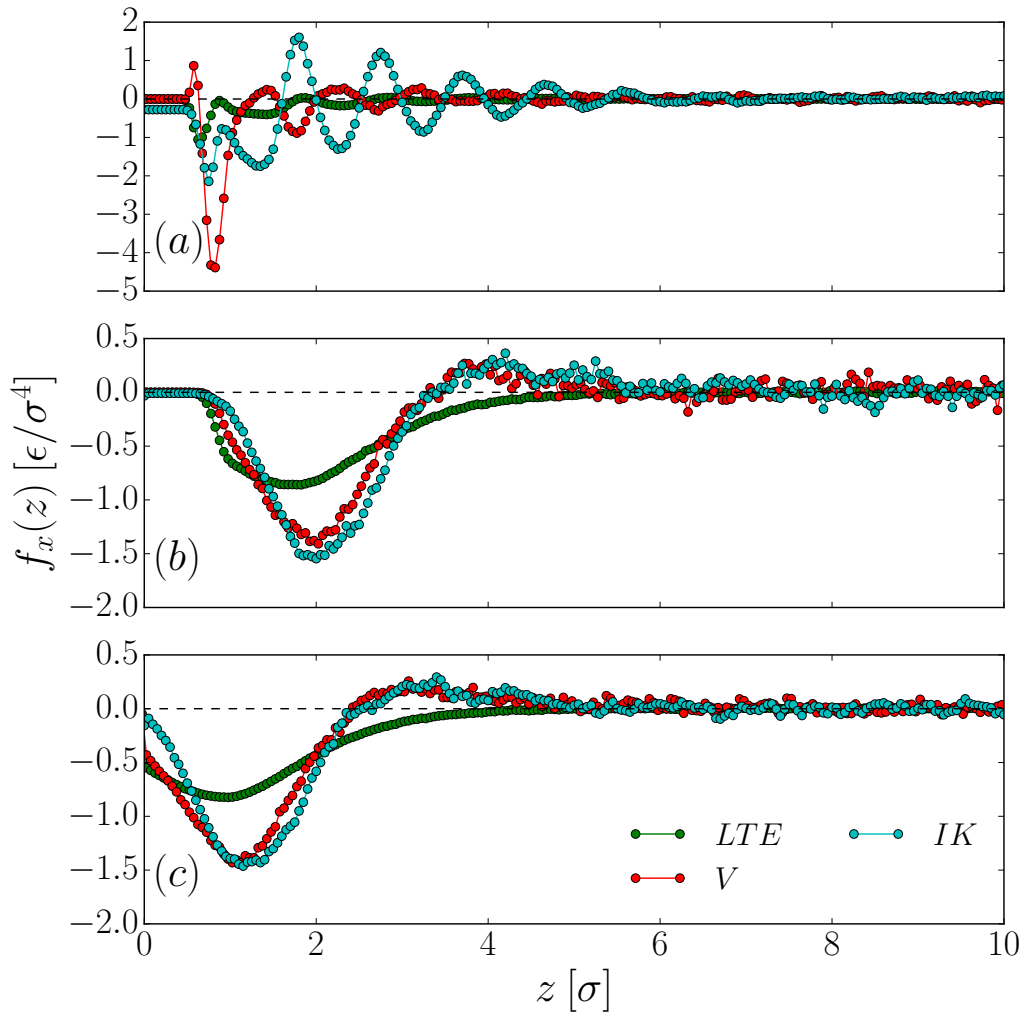


Figure 7.1: Calculation of the force density for $\nabla T = 1$ using the V (red) and IK (cyan) stress gradient, and LTE (green) approaches for (a) Lennard-Jones, (b) WCA, and (c) specular, reflective walls.

Surprisingly, for fluid interacting with the Lennard-Jones surface, the methods predict significantly different answers. To explain the discrepancy, we revisit the mechanical definition of surface tension (Eq. (7.2)). Eq. (7.2) assumes that P_T reduces to P in the bulk phases. This is true for the fluid phase, but not the case in the solid phase. Therefore, for fluid interacting with a structured, solid phase, the excess stress across the strip is not simply given by Eq. (7.2). The thermodynamic expression (Eq. (7.4)) as derived from the Gibbs-Adsorption relation is independent of phase information and should therefore give the correct answer.

Based on the preceding analysis, we expect that removing solid phase contributions to the surface tension gradient causes the discrepancy to vanish. Since Eq. (7.3) only depends on P_{xx} , we remove solid contributions to the surface tension gradient by considering fluid interacting with a specular, reflective wall. As shown in Table 7.1, all methods predict the same surface tension gradient when the wall no longer exerts any transverse stresses.

In related work on diffusio-osmotic and microscopic Marangoni flows (see Appendix 9.4), we found that mechanical and thermodynamic expressions predict the same surface tension gradient across a flat wall (Table 9.1) and liquid-liquid interface (Table 9.2). As Kirkwood and Buff theory is formulated for interacting, homogeneous bulk phases, the results for a liquid-liquid interface are unsurprising. Nevertheless, the agreement among the methods in these systems is consistent with what is presented in Table 7.1.

We may now explain why all methods can predict the same slip velocity in certain cases. If fluid is near a de-wetting transition, as it was with a WCA wall (see Fig. 5.7), solid contributions to the transverse pressure gradient are negligible and all methods roughly predict the same surface tension gradient (Table 7.1). If the integrated force density on the fluid does not differ sig-

nificantly among the methods, the slip velocity will likely be the same in all cases.

The failure of pressure expressions in predicting the surface tension gradient along a structured wall supports the argument that microscopic thermodynamic forces cannot be derived from pressure gradients. Independent of the chosen contour, any pressure tensor derived from momentum balance (see Chapter 3.1.2, Eq. (3.29))

$$P_{\alpha\beta}^{\phi}(\mathbf{r}) = -\frac{1}{2} \int d\mathbf{R} R^{\alpha} \frac{\phi'(R)}{R} \oint_{C_R} d\hat{l}^{\beta} \rho^{(2)}(\mathbf{r} - \hat{\mathbf{l}}, \mathbf{r} - \hat{\mathbf{l}} + \mathbf{R}) \quad (7.5)$$

will contain surface contributions. For a structured, solid that attracts the fluid, these contributions will cause incorrect predictions of the surface tension gradient. Therefore, even though we only explicitly tested the Irving-Kirkwood, virial, and Harasima stress tensors, it is likely that any other expression derived from Eq. (7.5) will also fail.

In short, Eq. (7.4), derived from the Gibbs-Adsorption relation, should always be used to compute surface tension gradients.

Chapter 8

Conclusion

In this work, we made significant advances towards a microscopic understanding of thermo-osmotic forces and flows. Using local thermal equilibrium approximations, we related the local pressure gradient to the product of the excess enthalpy density and temperature gradient. In doing so, we formulated the mechanical ‘stress gradient’ and thermodynamic ‘LTE’ approaches to compute the slip coefficient. For completeness, we also followed Derjaguin’s ‘LNET’ method by computing the excess heat flux due to a global pressure gradient giving the equivalent mechano-caloric coefficient. All methods yield reasonable agreement, but some are more noisy than others. The slip velocity serves as an inner boundary condition for mesoscopic hydrodynamic calculation of thermophoretic flows.

While calculation of the thermo-osmotic slip coefficient seemed invariant to the method of choice, we still needed to resolve which approach correctly predicts the thermo-osmotic force profile. By treating the mass of particles as a tensor in the Hamiltonian, we explored the limit where $M_{xx} \rightarrow \infty$, thereby eliminating the shear force induced by the thermal gradient. We could then compare the thermo-osmotic force that remains in the station-

ary system to those predicted by the stress gradient and LTE approaches. Surprisingly, both statistical mechanical and hydrodynamic formulations of pressure fail to accurately predict surface forces due to temperature gradients. Although the pressure tensor is useful for a hydrodynamic description of the problem [1], it does not match with what is measured microscopically. Fortunately, we find that the LTE expression for the thermo-osmotic force based on explicit calculation of the local enthalpy gets extremely close to the true result. The small discrepancy may be due to deviations from the local thermal equilibrium approximation.

In related work, we found that the same microscopic pressure expressions fail to predict diffusio-osmotic and solutal Marangoni flow profiles, whereas analogous LTE expressions make predictions that agree with direct, non-equilibrium calculations. These results bolster what we have found with thermal gradients.

In the penultimate chapter, we examine more deeply the failure of microscopic pressure expressions. From a macroscopic perspective, we expect all methods to predict the same surface tension gradient. Yet, in the case of a structured, solid wall that attracts the fluid, pressure expressions yield the wrong answer. We attribute the latter failure to the fact that the Kirkwood and Buff molecular theory of surface tension is not meant to be used for structured solid-fluid interfaces. Thus, removing solid phase contributions to the surface tension gradient by considering a flat, specular wall immediately resolves the problem. We conclude that on a macroscopic length scale, pressure expressions succeed in limiting cases.

To summarize the dissertation briefly, mechanical expressions of pressure fail to describe microscopic flows due to temperature and chemical potential gradients, whereas thermodynamic approaches almost succeed. Our simula-

tions suggest that there is a great need for a truly microscopic, statistical-mechanical theory of interfacial transport processes.

8.1 Future Work

In future work, we plan to use the Hamiltonian transformation described in Chapter 6.1 to definitively establish the microscopic force in thermal Marangoni and diffusio-osmotic transport. In the former case, it would be interesting to see how the presence of a membrane at the liquid-liquid interface changes the local viscosity and therefore the flow profile.

Furthermore, we plan to extend our simulation protocols to realistic systems so that we can compare slip calculations to existing experimental measurements. Using the slip velocities as inner boundary conditions in continuum simulations would allow us to connect the microscopic dynamics of thermo-osmosis to the macroscopic motion of colloids under the influence of thermal gradients.

Chapter 9

Appendix

9.1 Entropy Production from the Second Law

In this section, we shall closely follow De Groot and Mazur's derivation of the entropy production [11]. We start with the second law. The change in entropy within a system is given by

$$dS = d_e S + d_i S \quad (9.1)$$

where $d_e S$ is entropy supplied to the system from the surroundings and $d_i S$ is entropy produced within the system. In the presence of irreversible processes,

$$d_i S \geq 0. \quad (9.2)$$

For a closed system that can only exchange heat with its surroundings, the Clausius Theorem gives

$$d_e S = \frac{dQ}{T}. \quad (9.3)$$

Substitution of Eq. (9.2) and Eq. (9.3) into Eq. (9.1) recovers the conventional form of the second law

$$dS \geq \frac{dQ}{T}. \quad (9.4)$$

The total entropy within an arbitrary volume is given by

$$S = \int \rho s \, dV \quad (9.5)$$

where s is the specific entropy. In the presence of non-equilibrium processes, we must relate $d_i S$ to the irreversible fluxes within the system. The rate of change of the entropy supplied to the system is equivalent to the entropy flux across the surface area A that bounds the volume

$$\frac{d_e S}{dt} = - \int J_{s,tot}^\alpha \, dA^\alpha = - \int \nabla^\alpha J_{s,tot}^\alpha \, dV \quad (9.6)$$

where $J_{s,tot}^\alpha$ is the total entropy flow per unit area and time and Gauss' theorem is used in the second equality. The rate at which entropy is produced in the system is given by

$$\frac{d_i S}{dt} = \int \sigma \, dV \quad (9.7)$$

where σ is the entropy production per unit volume and time. Differentiating Eq. (9.1) with respect to time and substituting the above expressions gives

$$\int \frac{\partial \rho s}{\partial t} + \nabla^\alpha J_{s,tot}^\alpha - \sigma \, dV = 0. \quad (9.8)$$

Since Eq. (9.1) and Eq. (9.2) holds for an arbitrary volume,

$$\frac{\partial \rho s}{\partial t} = -\nabla^\alpha J_{s,tot}^\alpha + \sigma \quad (9.9)$$

$$\sigma \geq 0. \quad (9.10)$$

Eq. (9.9) is the entropy balance equation with a source term σ . Using a relation derived from mass balance (see Appendix 9.2), written here for clarity

$$\rho \frac{da}{dt} = \frac{\partial \rho a}{\partial t} + \nabla^\alpha \rho a v^\alpha \quad (9.11)$$

we can re-express Eq. (9.9) as

$$\rho \frac{ds}{dt} = -\nabla^\alpha J_s^\alpha + \sigma \quad (9.12)$$

where

$$J_s^\alpha = J_{s,tot}^\alpha - \rho s v^\alpha. \quad (9.13)$$

In the process of deriving Eq. (9.12), we have assumed that macroscopic laws hold for infinitesimally small volume elements of the system. These volumes still contain large numbers of particles and therefore, it is possible to discuss local values of entropy and entropy production.

We still have the crucial task of constructing explicit expressions for J_s and σ in Eq. (9.12). Using the Gibbs relation for an n -component mixture and dividing by the total number of atoms gives

$$T ds = du + p dv - \sum_{k=1}^n \mu_k dc_k \quad (9.14)$$

where s is the specific entropy, u is the internal energy, p is the equilibrium pressure, $v = 1/\rho$, μ_k is the chemical potential of species k , and c_k is the mass fraction of species k . While globally the system is out of equilibrium, there are still small volume elements in a state of local equilibrium. Therefore, we assume that the form of the Gibbs-relation holds even though the differentials in Eq. (9.14) are changing with time

$$T \frac{ds}{dt} = \frac{du}{dt} + p \frac{dv}{dt} - \sum_{k=1}^n \mu_k \frac{dc_k}{dt}. \quad (9.15)$$

All differentials here are material derivatives

$$\frac{d}{dt} = \frac{\partial}{\partial t} + v^\alpha \nabla^\alpha. \quad (9.16)$$

Using the relations derived from mass balance (see Chapter 2.2 in Ref [11]) written here for convenience

$$\frac{dc_k}{dt} = \left(\frac{1}{\rho} \right) \left(-\nabla^\alpha J_k^\alpha + \sum_{j=1}^r \nu_{kj} J_j \right) \quad (9.17)$$

and energy balance (see Chapter 2.4 in Ref [11])

$$\frac{du}{dt} + p \frac{dv}{dt} = \left(\frac{1}{\rho} \right) \left(-\nabla^\alpha J_q^\alpha - \Pi^{\alpha\beta} \nabla^\beta v^\alpha + \sum_{k=1}^n J_k^\alpha F_k^\alpha \right) \quad (9.18)$$

we can re-express Eq. (9.15) as

$$\rho \frac{ds}{dt} = \left(\frac{1}{T} \right) \left(-\nabla^\alpha J_q^\alpha - \Pi^{\alpha\beta} \nabla^\beta v^\alpha + \sum_{k=1}^n J_k^\alpha F_k^\alpha + \sum_{k=1}^n \mu_k \nabla^\alpha J_k^\alpha - \sum_{k=1}^n \sum_{j=1}^r \nu_{kj} \mu_k J_j \right). \quad (9.19)$$

We would now like to determine which contributions to the entropy production from the right-hand side are due to entropy flow into the system

from the surroundings and which are due to entropy production within the system. We can rearrange Eq. (9.19) into the form

$$\begin{aligned} \rho \frac{ds}{dt} = & -\nabla^\alpha \left(\frac{J_q^\alpha - \sum_{k=1}^n \mu_k J_k^\alpha}{T} \right) \\ & - \frac{1}{T} \left(J_q^\alpha \frac{\nabla^\alpha T}{T} + \sum_{k=1}^n J_k^\alpha \left(T \nabla^\alpha \left(\frac{\mu_k}{T} \right) - F_k^\alpha \right) + \Pi^{\alpha\beta} \nabla^\beta v^\alpha + \sum_{k=1}^n \sum_{j=1}^r \nu_{kj} \mu_k J_j \right). \end{aligned} \quad (9.20)$$

Comparing Eq. (9.20) with Eq. (9.12) gives the entropy flux from the surroundings

$$J_s^\alpha = \left(\frac{1}{T} \right) \left(J_q^\alpha - \sum_{k=1}^n \mu_k J_k^\alpha \right) \quad (9.21)$$

and the entropy production

$$\begin{aligned} \sigma = & -\frac{1}{T} \left(J_q^\alpha \frac{\nabla^\alpha T}{T} + \sum_{k=1}^n J_k^\alpha \left(T \nabla^\alpha \left(\frac{\mu_k}{T} \right) - F_k^\alpha \right) \right. \\ & \left. + \Pi^{\alpha\beta} \nabla^\beta v^\alpha + \sum_{k=1}^n \sum_{j=1}^r \nu_{kj} \mu_k J_j \right) \geq 0. \end{aligned} \quad (9.22)$$

While separation between the flow and source term may seem arbitrary, the form of Eq. (9.22) is fixed by the additional constraints that the entropy production is Galileian invariant and must vanish in equilibrium. It is clear that Eq. (9.22) satisfies these constraints. From Eq. (9.22), we can now clearly see all possible sources of entropy production. The first term is heat conduction, second is diffusion of different species, third is viscous flow, and fourth is chemical reactions. It is also worth noting that the entropy production is a sum of the products of fluxes and gradients of intensive state variables.

9.2 Mass Balance

In the process of deriving the entropy production, we made use of Eq. (9.11).

We derive the relation here using conservation of mass [11]

$$\frac{\partial \rho}{\partial t} = -\nabla^\alpha(\rho v^\alpha) \quad (9.23)$$

where ρ is the total density in the system. The material derivative is given by

$$\frac{d}{dt} = \frac{\partial}{\partial t} + v^\alpha \nabla^\alpha. \quad (9.24)$$

Suppose there is an arbitrary local property a , which can be a scalar, vectorial, or tensorial quantity. Taking the material derivative of a and multiplying through by ρ gives

$$\rho \frac{da}{dt} = \rho \frac{\partial a}{\partial t} + \rho v^\alpha \nabla^\alpha a \quad (9.25)$$

$$= \frac{\partial \rho a}{\partial t} - a \frac{\partial \rho}{\partial t} + \rho v^\alpha \nabla^\alpha a. \quad (9.26)$$

Using Eq. (9.23), this can be rearranged into the form

$$\rho \frac{da}{dt} = \frac{\partial \rho a}{\partial t} + a \nabla^\alpha \rho v^\alpha + \rho v^\alpha \nabla^\alpha a \quad (9.27)$$

$$= \frac{\partial \rho a}{\partial t} + \nabla^\alpha(\rho a v^\alpha). \quad (9.28)$$

9.3 Irving-Kirkwood Computational Expression

In Chapter 3.1.1, we derived the Irving-Kirkwood pressure tensor at a planar interface:

$$P_T(z) = \rho(z)k_B T - \frac{1}{2} \left\langle \sum_{i,j}^N \int \frac{x_{ij}^2}{r_{ij}} \phi'(r_{ij}) \times \int_0^1 \delta(z - \lambda Z - \mathbf{r}_i) \delta(z - \lambda Z + \mathbf{R} - \mathbf{r}_j) d\lambda d\mathbf{R} \right\rangle \quad (9.29)$$

$$P_N(z) = \rho(z)k_B T - \frac{1}{2} \left\langle \sum_{i,j}^N \int \frac{z_{ij}^2}{r_{ij}} \phi'(r_{ij}) \times \int_0^1 \delta(z - \lambda Z - \mathbf{r}_i) \delta(z - \lambda Z + \mathbf{R} - \mathbf{r}_j) d\lambda d\mathbf{R} \right\rangle. \quad (9.30)$$

We are interested in casting Eq. (9.29) and Eq. (9.30) into forms more suitable for calculation in simulation. To do so, we must express the pair distribution

function in a more tractable form

$$\begin{aligned}
& \left\langle \int \int_0^1 \delta(z - \lambda Z - \mathbf{r}_i) \delta(z - \lambda Z + \mathbf{R} - \mathbf{r}_j) d\lambda d\mathbf{R} \right\rangle \\
&= \left\langle \int \int_0^1 \delta(z - \lambda Z - \mathbf{r}_i) \delta(\mathbf{R} - \mathbf{r}_{ij}) d\lambda d\mathbf{R} \right\rangle \\
&= \left\langle \int_0^1 \delta(z - \lambda z_{ij} - \mathbf{r}_i) d\lambda \right\rangle \\
&= \frac{1}{A} \left\langle \int_0^1 \delta(z - \lambda z_{ij} - z_i) d\lambda \right\rangle \\
&= \frac{1}{A} \left\langle \int_0^1 \frac{\delta\left(\lambda - \frac{z - z_i}{z_{ij}}\right)}{|z_{ij}|} d\lambda \right\rangle \\
&= \frac{1}{A} \left\langle \int_0^1 \Theta(\lambda) \Theta(1 - \lambda) \frac{\delta\left(\lambda - \frac{z - z_i}{z_{ij}}\right)}{|z_{ij}|} d\lambda \right\rangle \\
&= \frac{1}{A} \left\langle \frac{\Theta\left(\frac{z - z_i}{z_{ij}}\right) \Theta\left(\frac{z_j - z}{z_{ij}}\right)}{|z_{ij}|} \right\rangle. \tag{9.31}
\end{aligned}$$

We can now substitute Eq. (9.31) into Eq. (9.29) and Eq. (9.30) to give

$$P_T(z) = \rho(z) k_B T - \frac{1}{2A} \left\langle \sum_{i,j}^N \frac{x_{ij}^2 \phi'(r_{ij})}{r_{ij} |z_{ij}|} \Theta\left(\frac{z - z_i}{z_{ij}}\right) \Theta\left(\frac{z_j - z}{z_{ij}}\right) \right\rangle \tag{9.32}$$

$$P_N(z) = \rho(z) k_B T - \frac{1}{2A} \left\langle \sum_{i,j}^N \frac{z_{ij}^2 \phi'(r_{ij})}{r_{ij} |z_{ij}|} \Theta\left(\frac{z - z_i}{z_{ij}}\right) \Theta\left(\frac{z_j - z}{z_{ij}}\right) \right\rangle. \tag{9.33}$$

9.4 Microscopic Flows due to Chemical Potential Gradients

In addition to exploring microscopic flows due to temperature gradients, the theoretical and computational methods described in Chapters 2 and 5 can be

applied towards understanding microscopic flows due to chemical potential gradients. We explore two cases: diffusio-osmotic flow induced at a liquid-solid interface and solutal Marangoni flow at a liquid-liquid interface. In the latter case, the flow is induced by a surface tension gradient. As was the case with thermo-osmosis and the thermo-capillary effect, Derjaguin formulated a picture of diffusio-osmosis using Linear Non-equilibrium Thermodynamics [14], while Levich offered a hydrodynamic treatment of the Marangoni effect [38]. In this section, we will show that the same theoretical treatment and molecular expressions developed in the main text can be exploited to formulate a microscopic understanding of interfacial flows induced by chemical potential gradients.

9.4.1 Diffusio-osmosis

The work presented in this section is part of a collaborative effort that is in preparation [41].

Consider a fluid mixture containing a majority of solvent (A) and a minority of solute (B) interacting via a Lennard-Jones potential (Eq. (5.18)) with an atomically structured wall as shown in Fig. 9.1(a). The only difference between the two species is in the strength with which they interact with the bottom wall ($\epsilon_{B,wall} = 2\epsilon_{A,wall} = 1.1\epsilon$). In the bulk, the Gibbs-Duhem relation is given by

$$VdP = N_A^{\text{bulk}}d\mu_A + N_B^{\text{bulk}}d\mu_B. \quad (9.34)$$

At constant pressure, a concentration gradient in either species leads to chem-

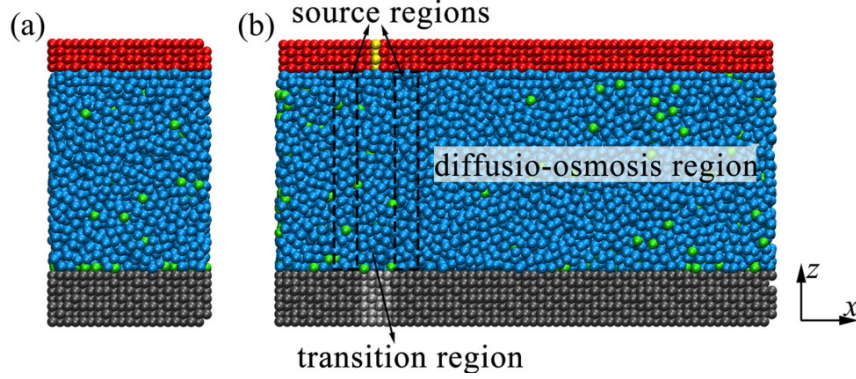


Figure 9.1: (a) Simulation box used to compute the diffusio-osmotic force and flow profiles using the stress gradient and LTE approaches. (b) Simulation box used in the non-equilibrium MD simulations with explicitly imposed concentration gradients. The blue particles represent the solvent (A), the green particles represent the solute (B), the red and yellow particles represent the solid particles in the top wall, and the black and silver particles represent the solid particles in the bottom wall.

ical potential gradients in both species. Eq. (9.34) therefore reduces to

$$0 = \rho_A^{\text{bulk}}(x) \left(\frac{\partial \mu_A}{\partial x} \right) + \rho_B^{\text{bulk}}(x) \left(\frac{\partial \mu_B}{\partial x} \right). \quad (9.35)$$

At a position z near the interface, an excess pressure gradient remains. Subtracting the Gibbs-Duhem relation at z from Eq. (9.35) gives the local pressure gradient that drives diffusio-osmotic flow:

$$f^V(z) = -\frac{\partial P_{xx}(x, z)}{\partial x} = - \left[(\rho_A(z, x) - \rho_A^{\text{bulk}}(x)) \left(\frac{\partial \mu_A}{\partial x} \right) + (\rho_B(z, x) - \rho_B^{\text{bulk}}(x)) \left(\frac{\partial \mu_B}{\partial x} \right) \right]. \quad (9.36)$$

Upon comparison with the derivation of thermo-osmosis from the Gibbs-Duhem relation (see Chapter 2.1), we see that the critical difference in diffusio-osmosis is that the local pressure gradient arises due to the inter-

facial coupling of the excess densities to the chemical potential gradients. The excess density of different species is unambiguously defined, whereas the excess enthalpy density suffers from ambiguities (see Chapter 5.2).

We can use a variation of the stress gradient method (see Chapter 5.1) to compute the left-hand side of Eq. (9.36):

$$\frac{\partial P_{xx}(z)}{\partial x} \approx \frac{P_{xx}(\rho_B + \Delta\rho_B, z) - P_{xx}(\rho_B, z)}{\Delta\rho_B} \left(\frac{\partial\rho_B}{\partial x} \right). \quad (9.37)$$

The local pressure gradient can be computed by evaluating the transverse pressure profiles in equilibrium simulations at ρ_B and $\rho_B + \Delta\rho_B$. As before, the non-uniqueness of the microscopic definition of pressure once again arises (see Chapter 3.1). We may use the virial or Irving-Kirkwood expression to evaluate $P_{xx}(z)$ and the pressure gradient will depend on the choice.

To bypass the ambiguities of mechanical expressions, we can formulate a Local Thermal Equilibrium (LTE) approach (see Chapter 5.2) to compute the right-hand side of Eq. (9.36). The chemical potential for a component i is given by

$$\mu_i = \mu_i^{\text{ref}} + k_B T \ln \rho_i^{\text{bulk}} + \mu_i^{\text{exc}} \quad (9.38)$$

where μ_i^{ref} is the reference chemical potential related to the deBroglie wavelength and μ_i^{exc} is the excess chemical potential. Assuming the bulk solution is ideal, that is, μ_i^{ref} and μ_i^{exc} are insensitive to a change in solute or solvent concentration, the chemical potential gradient of species i is given by

$$\frac{\partial\mu_i}{\partial x} = \left(\frac{k_B T}{\rho_i^{\text{bulk}}} \right) \frac{\partial\rho_i^{\text{bulk}}}{\partial x}. \quad (9.39)$$

For a given $\nabla\rho_B$ and ρ_B , $\partial\mu_B/\partial x$ can be computed using Eq. (9.39) and $\partial\mu_A/\partial x$ from rearrangement of Eq. (9.35). The excess density profiles $\rho_A(z)$ –

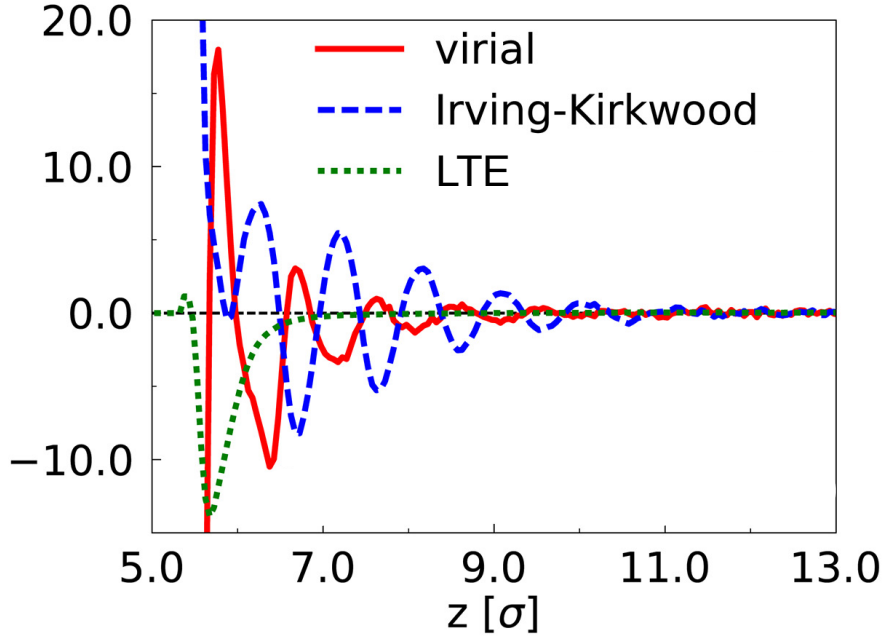


Figure 9.2: Average per-particle force profiles computed at $\rho_B = 0.02$ and $\nabla\rho_B = 1.0$ using the virial (red) and Irving-Kirkwood (blue) expressions in Eq. (9.37) and the LTE (green) approach (Eq. (9.36))

ρ_A^{bulk} and $\rho_B(z) - \rho_B^{\text{bulk}}$ can be calculated in an equilibrium simulation at the same ρ_B . Using the latter information, the right-hand side of Eq. (9.36) can be determined.

Fig. 9.2 shows the force per particle $f(z)/\rho(z)$ computed via the stress gradient and LTE approaches. As was the case with thermo-osmotic forces (Fig. 6.7), the methods give three different answers. Applying the force profiles as artificial body forces to systems at $\rho_B = 0.02$ gives three different flow velocity profiles as shown in Fig. 9.4(a).

To determine which, if any, give the true answer, a direct non-equilibrium approach was implemented. The non-equilibrium setup is shown in Fig. 9.1(b). A concentration gradient $\nabla\rho_B$ is imposed by changing the identities of fluid particles in the source regions every 500 steps. In the low concentration

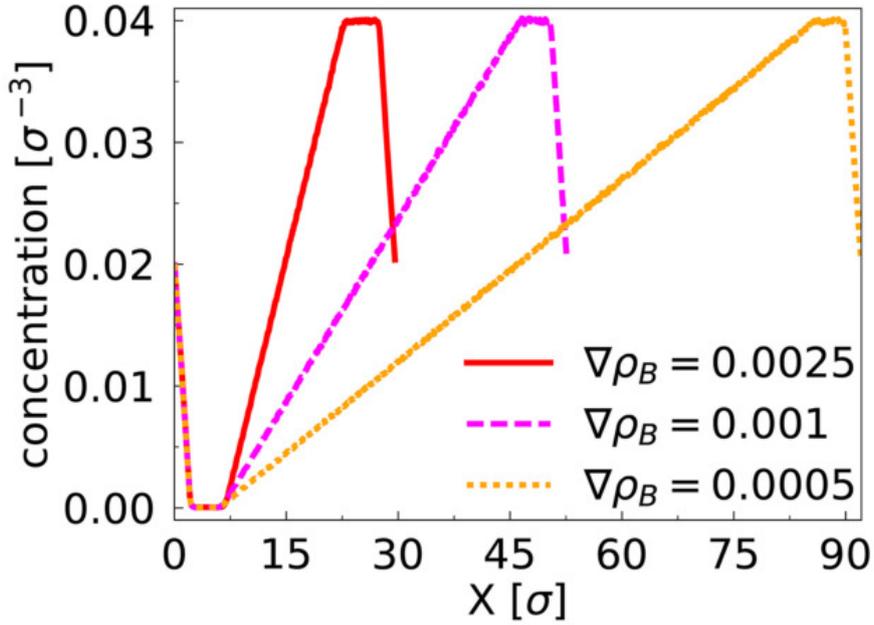


Figure 9.3: The bulk concentration profiles in the non-equilibrium simulations.

source region $\rho_B = 0$, that is, all particles are reset to type A , whereas $\rho_B = 0.04$ in the high concentration source region. To test different magnitudes of $\nabla\rho_B$, the simulation box size in x was varied as shown in Fig. 9.3. The flow profile in the diffusio-osmosis region is compared to the flow profiles predicted by the stress gradient and LTE methods in Fig. 9.4. It appears that the LTE predictions (Fig. 9.4(c)) agree with the non-equilibrium flow profiles (Fig. 9.4(b)) whereas those predicted by stress gradients fail. These calculations are consistent with Figs. 6.7 and 6.8, which show that stress gradients fail to predict thermo-osmotic forces.

Yet, it is worth noting that stress gradients also fail to predict the diffusio-osmotic slip velocity, that is, the velocity far away from the surface. As we did in Chapter 7, we contend that the discrepancy can be explained by the methods predicting different surface tension gradients. In the next section,

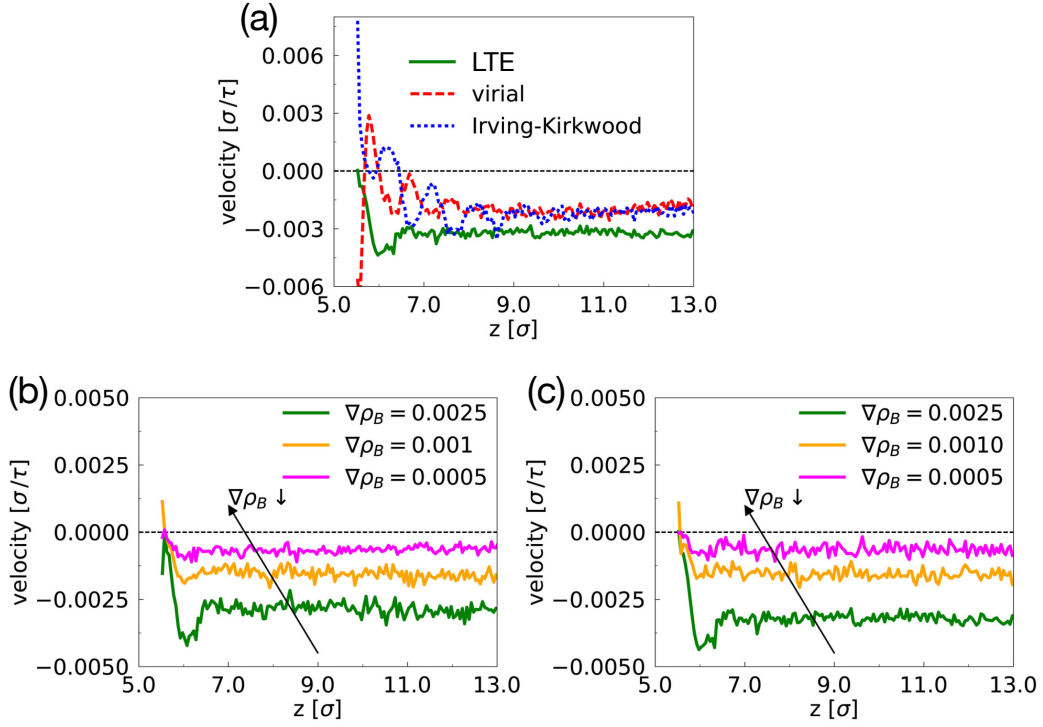


Figure 9.4: (a) Flow velocity profiles at $\rho_B = 0.02$ and $\nabla\rho_B = 0.0025$ predicted by the stress gradient and LTE methods. (b) Flow velocity profiles directly measured from the non-equilibrium simulations. (c) Flow velocity profiles at different concentration gradients using the LTE method.

we show that Eq. (9.36) can be related to the surface tension gradient via the Gibbs-Adsorption relation. Upon integration of the force density predicted by the different methods, we find indeed that the stress gradient and LTE methods give significantly different surface tension gradients as shown in Table 9.1. Following the same line of reasoning in Chapter 7, we considered that wall contributions to the transverse stress cause the latter discrepancy. To remove wall contributions, we replaced the surface with a specular wall that exerts a z -dependent Lennard-Jones potential on the fluid

$$U_{fluid-wall}(z) = 4\epsilon_{fw} \left[(\sigma/z)^{12} - (\sigma/z)^6 \right] \quad (9.40)$$

Surface Tension Gradients

	Lennard-Jones	Specular
LTE	-5.81 ± 0.1	-0.19 ± 0.01
V	1.07 ± 0.1	-0.2 ± 0.1
IK	1.07 ± 0.1	-0.26 ± 0.1

Table 9.1: Diffusio-osmotic surface tension gradient predictions by the mechanical and thermodynamic methods near Lennard-Jones and specular walls.

where $\epsilon_{B,w} = 2\epsilon_{A,w} = 1.1\epsilon$.

Once again, we measured the diffusio-osmotic force density via the stress gradient and LTE methods. Integration gives the surface tension gradients shown in Table 9.1. Consistent with our analysis in Chapter 7, stress gradients fail to predict the surface tension gradient for structured walls and succeed for flat walls that do not exert any transverse stress on the fluid.

9.4.2 Solutal Marangoni Effect

The non-equilibrium, stress gradient and thermodynamic methods discussed in the previous section are not limited to liquid-solid interfaces. At a liquid-liquid interface, external chemical potential gradients induce a local stress gradient leading to Marangoni flow. The difference in the latter case is that the interface also moves due to the gradient. Therefore, there is no balancing shear flow as was the case with a fixed solid surface. Clearly, the boundary conditions become significant if one wants to compute the Marangoni flow profile. In this section, we use the same computational methods to construct a microscopic picture of the solutal Marangoni effect. The work presented in this section was part of a collaborative effort published in Ref [40].

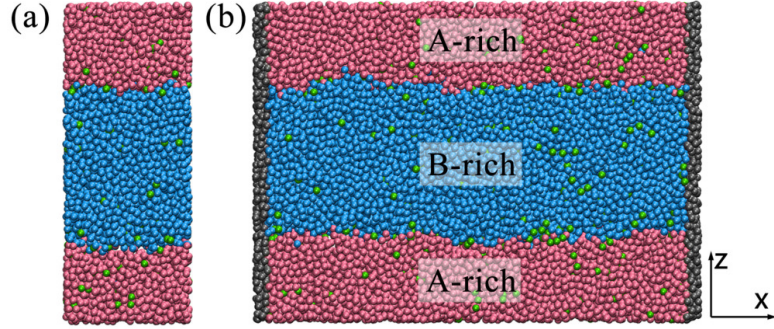


Figure 9.5: (a) Simulation box used to compute the solutal Marangoni force and flow profiles using stress gradient and local equilibrium techniques. (b) Simulation box used in the non-equilibrium MD simulations with explicitly imposed concentration gradients. The red and blue particles represent the two solvents (A and B), the green particles represent the solute (C), and the black particles represent the solid walls.

Consider a fluid mixture containing two immiscible solvents (A and B) and miscible solute (C) as shown in Fig. 9.5(a). A concentration gradient in species C induces a surface tension gradient at the interface

$$\frac{\partial \gamma}{\partial x} = \left(\frac{\partial \gamma}{\partial \rho_C} \right) \frac{\partial \rho_C}{\partial x}. \quad (9.41)$$

Using the Gibbs-Adsorption relation (Eq. (2.23)) at constant temperature, the surface tension gradient is given by

$$\frac{\partial \gamma}{\partial x} = \int_{-\infty}^{\infty} \sum_{i=1}^n (\rho_i(z, x) - \rho_i^{\text{bulk}}(x)) \left(-\frac{\partial \mu_i}{\partial x} \right) dz. \quad (9.42)$$

The right-hand side is an integration of Eq. (9.36) showing the connection to diffusio-osmosis. Using Eq. (7.3), we can relate the local pressure gradient to

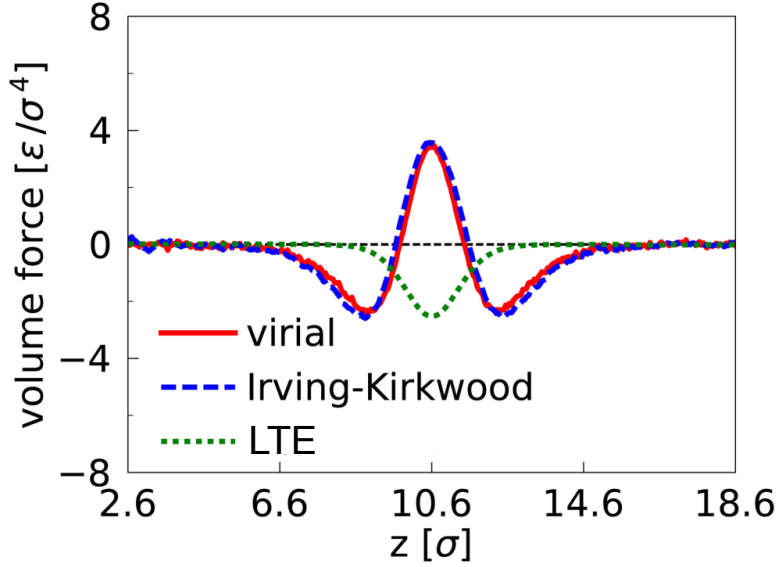


Figure 9.6: Force profiles per unit $\nabla\rho_C$ along z near one of the interfaces shown in Fig. 9.5(a) ($z = 10.6$) corresponding to a system at $\rho_C \sim 0.02$.

the excess densities and chemical potential gradients of the different species:

$$\begin{aligned}
 -\frac{\partial P_{xx}(x, z)}{\partial x} = & - \left[(\rho_A(z, x) - \rho_A^{\text{bulk}}(x)) \left(\frac{\partial \mu_A}{\partial x} \right) \right. & (9.43) \\
 & + (\rho_B(z, x) - \rho_B^{\text{bulk}}(x)) \left(\frac{\partial \mu_B}{\partial x} \right) \\
 & \left. + (\rho_C(z, x) - \rho_C^{\text{bulk}}(x)) \left(\frac{\partial \mu_C}{\partial x} \right) \right].
 \end{aligned}$$

We may now use the stress gradient (Eq. (9.37)) and LTE (Eq. (9.35), Eq. (9.36), Eq. (9.39)) approaches to calculate microscopic Marangoni forces in three different ways. The stress gradient method remains unchanged due to the presence of C . The LTE approach does change. However, Fig. 9.5(a) shows that apart from the interaction of A with B , the two species are identical in the bulk. Since $\rho_A^{\text{bulk}} = \rho_B^{\text{bulk}}$, $\nabla\mu_A = \nabla\mu_B$ due to force balance in the bulk.

Surface Tension Gradients

	Liquid-Liquid
LTE	-4.7 ± 0.1
V	-4.8 ± 0.1
IK	-4.8 ± 0.1

Table 9.2: Marangoni surface tension gradient predictions by the mechanical and thermodynamic methods at a liquid-liquid interface.

Fig. 9.6 shows the force profiles calculated using the stress gradient and LTE methods. As before, the LTE approach predicts an entirely different answer. Interestingly, the virial and Irving-Kirkwood expressions predict approximately the same stress gradient, deviating from what was observed with diffusio-osmotic forces (Fig. 9.2). This is consistent with Schofield and Henderson’s statement [65] that while the stress tensor cannot be uniquely defined, the stress gradient is indeed well-defined (see Chapter 3.1.2) though this may only be true for a liquid-liquid interface. Furthermore, integrating the force profiles in Fig. 9.6 gives the surface tension gradient (Eq. (9.42)). Interestingly, Table 9.2 shows that mechanical and thermodynamic expressions predict the same surface tension gradient.

Dividing the force densities in Fig. 9.6 by $\rho(z)$ gives the force per particle, which can be introduced as a body force to an equilibrium system at $\rho_C = 0.02$. As the virial and Irving-Kirkwood force profiles do not differ significantly, only the body force predicted by the virial is applied. Because there is no balancing shear flow, a constant opposing force must be applied to all fluid particles so that the integrated flow profile vanishes. The com-

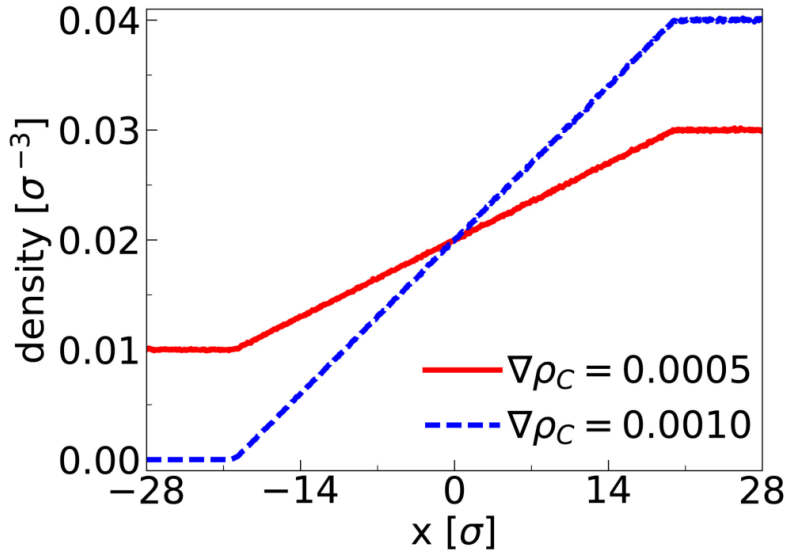


Figure 9.7: The bulk concentration profiles along x from the non-equilibrium simulations.

compensating force causes back-flow in the bulk as shown in Fig. 9.8.

Once again, a direct, non-equilibrium approach was explored as shown in Fig. 9.5(b). Near each solid wall, a source region is defined. Every 500 steps, the identities of fluid particles in the source regions are changed to maintain a constant concentration gradient as shown in Fig. 9.7. The presence of solid walls causes back-flow in the bulk such that the flow profile integrates to zero.

Consistent with the diffusio-osmotic picture, the flow profile predicted by the LTE approach appears to agree with the non-equilibrium measurement whereas the stress gradient approximation fails. However, because all methods predict the same surface tension gradient (Table 9.2), the bulk flow velocity is the same in all cases.

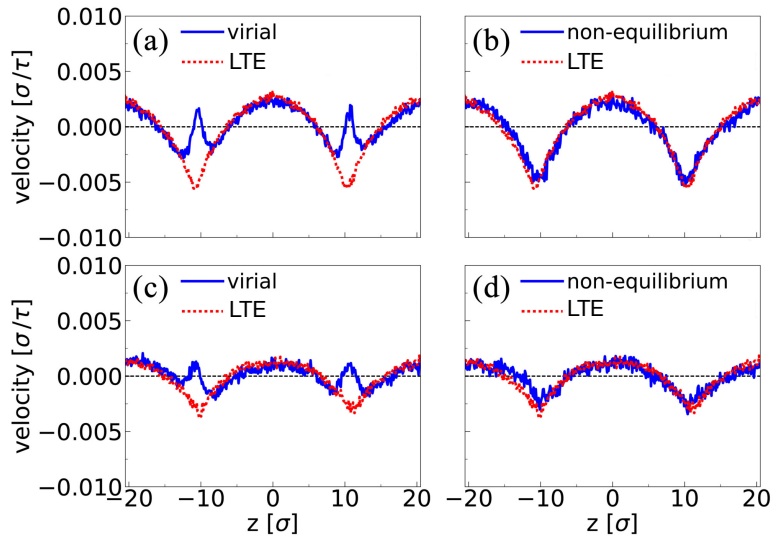


Figure 9.8: The velocity profiles along z from different methods at (a-b) $\nabla\rho_C = 0.0010$ and (c-d) $\nabla\rho_C = 0.0005$. The horizontal dashed line corresponds to the velocity of zero.

Bibliography

- [1] J. Anderson. Colloid transport by interfacial forces. *Annu. Rev. Fluid Mech.*, 21:61–99, 1989.
- [2] Aubert. *Ann. Chim. Phys.*, 26(145):551, 1912.
- [3] S. Aubry, E. B. Webb III, G. J. Wagner, P. A. Klein, R. E. Jones, J. A. Zimmerman, D. J. Bammann, J. J. Hoyt, and C. J. Kimmer. A robust, coupled approach for atomistic-continuum simulation. Technical report, Sandia National Laboratories, 2004.
- [4] D. Braun and A. Libchaber. Thermal force approach to molecular evolution. *Physical Biology*, 1(1):P1, 2004.
- [5] A. Bregulla, A. Würger, K. Günther, M. Mertig, and F. Cichos. Thermoosmotic flow in thin films. *Phys. Rev. Lett.*, 116(18):188303, 2016.
- [6] J. Burelbach, D. Frenkel, I. Pagonabarraga, and E. Eiser. A unified description of colloidal thermophoresis. *arXiv preprint arXiv:1708.02195*, 2017.
- [7] C. Carnahan. Thermal osmosis near a buried heat source. *International communications in heat and mass transfer*, 13(6):659–664, 1986.
- [8] D. Chretien, P. Benit, H.-H. Ha, S. Keipert, R. El-Khoury, Y.-T. Chang, M. Jastroch, H. Jacobs, P. Rustin, and M. Rak. Mitochondria are physiologically maintained at close to 50 c. *bioRxiv*, page 133223, 2017.
- [9] J. Cohen and R. Golestanian. Emergent cometlike swarming of optically driven thermally active colloids. *Phys. Rev. Lett.*, 112:068302, Feb 2014.
- [10] M. Dariel and O. Kedem. Thermoosmosis in semipermeable membranes. *The Journal of Physical Chemistry*, 79(4):336–342, 1975.
- [11] S. de Groot and P. Mazur. *Non-equilibrium Thermodynamics*. North Holland Publishing, Amsterdam, 1962.

- [12] K. Denbigh. Thermo-osmosis of gases through a membrane. *Nature*, 163:60, 1949.
- [13] K. Denbigh and G. Raumann. The thermo-osmosis of gases through a membrane. i. theoretical. In *Proceedings of the Royal Society of London A: Mathematical, Physical and Engineering Sciences*, volume 210, pages 377–387. The Royal Society, 1952.
- [14] B. Derjaguin, N. Churaev, and V. Muller. *Surface Forces*. Plenum, New York, 1987.
- [15] B. Derjaguin and G. Sidorenkov. Thermoosmosis at ordinary temperatures and its analogy with the thermomechanical effect in helium ii. *CR Acad. Sci*, 32:622–626, 1941.
- [16] J. Dhont, S. Wiegand, S. Duhr, and D. Braun. Thermodiffusion of charged colloids: Single-particle diffusion. *Langmuir*, 23:1674–1683, 2007.
- [17] C. Dirksen. Thermo-osmosis through compacted saturated clay membranes. *Soil Science Society of America Journal*, 33(6):821–826, 1969.
- [18] S. Duhr, S. Arduini, and D. Braun. Thermophoresis of dna determined by microfluidic fluorescence. *The European Physical Journal E: Soft Matter and Biological Physics*, 15(3):277–286, 2004.
- [19] S. Duhr and D. Braun. Thermophoretic depletion follows boltzmann distribution. *Physical review letters*, 96(16):168301, 2006.
- [20] S. Duhr and D. Braun. Why molecules move along a temperature gradient. *Proceedings of the National Academy of Sciences*, 103(52):19678–19682, 2006.
- [21] R. Eisenschitz. “virial theorem” for the flow of energy. *Physical Review*, 99(4):1059, 1955.
- [22] D. Frenkel and B. Smit. *Understanding molecular simulation: from algorithms to applications*, volume 1. Academic press, 2001.
- [23] R. Ganti, Y. Liu, and D. Frenkel. Hamiltonian transformation to compute thermo-osmotic forces. *arXiv preprint arXiv:1710.01657*, 2017.
- [24] R. Ganti, Y. Liu, and D. Frenkel. Molecular simulation of thermo-osmotic slip. *Phys. Rev. Lett.*, 119:038002, Jul 2017.

- [25] M. Giglio and A. Vendramini. Thermal-diffusion measurements near a consolute critical point. *Physical Review Letters*, 34(10):561, 1975.
- [26] R. Golestanian, T. Liverpool, and A. Ajdari. Designing phoretic micro- and nano-swimmers. *New J. Phys.*, 9:126, 2007.
- [27] J. Gonçalves, G. de Marsily, and J. Tremosa. Importance of thermo-osmosis for fluid flow and transport in clay formations hosting a nuclear waste repository. *Earth and Planetary Science Letters*, 339:1–10, 2012.
- [28] J. Gonçalves and J. Trémosa. Estimating thermo-osmotic coefficients in clay-rocks: I. theoretical insights. *Journal of colloid and interface science*, 342(1):166–174, 2010.
- [29] R. Haase and H. De Greiff. *Z. Naturforsch. A*, 26:1773, 1971.
- [30] M. Han. Thermophoresis in liquids: a molecular dynamics simulation study. *J. Colloid Interface Sci.*, 284:339–348, 2005.
- [31] J. Hansen and I. McDonald. *Theory of Simple Liquids*. Elsevier, 1990.
- [32] W. G. Hoover. Canonical dynamics: equilibrium phase-space distributions. *Physical review A*, 31(3):1695, 1985.
- [33] S. Iacopini and R. Piazza. Thermophoresis in protein solutions. *EPL (Europhysics Letters)*, 63(2):247, 2003.
- [34] S. Iacopini, R. Rusconi, and R. Piazza. The macromolecular tourist”: Universal temperature dependence of thermal diffusion in aqueous colloidal suspensions. *The European Physical Journal E: Soft Matter and Biological Physics*, 19(1):59–67, 2006.
- [35] T. Ikeshoji and B. Hafskjold. Non-equilibrium molecular dynamics calculation of heat conduction in liquid and through liquid-gas interface. *Molecular Physics*, 81(2):251–261, 1994.
- [36] J. Irving and J. Kirkwood. The statistical mechanical theory of transport processes. iv. the equations of hydrodynamics. *J. Chem. Phys*, 18:817–829, 1950.
- [37] J. G. Kirkwood and F. P. Buff. The statistical mechanical theory of surface tension. *The Journal of Chemical Physics*, 17(3):338–343, 1949.
- [38] V. G. Levich. *Physicochemical hydrodynamics*. Prentice hall, 1962.

- [39] Lippmann. *C.R. Acad. Sci.*, 145(104):105, 1907.
- [40] Y. Liu, R. Ganti, H. G. A. Burton, X. Zhang, W. Wang, and D. Frenkel. Microscopic marangoni flows cannot be predicted on the basis of pressure gradients. *Phys. Rev. Lett.*, 119:224502, Nov 2017.
- [41] Y. Liu, R. Ganti, and D. Frenkel. Pressure gradients fail to predict diffusio-osmosis. *In preparation*.
- [42] S. Maduar, A. Belyaev, V. Lobaskin, and O. Vinogradova. Electrohydrodynamics near hydrophobic surfaces. *Physical review letters*, 114(11):118301, 2015.
- [43] G. J. Martyna, M. L. Klein, and M. Tuckerman. Nosé–hoover chains: the canonical ensemble via continuous dynamics. *The Journal of chemical physics*, 97(4):2635–2643, 1992.
- [44] G. McNab and A. Meisen. Thermophoresis in liquids. *Journal of Colloid and Interface Science*, 44(2):339–346, 1973.
- [45] J. Mengual, J. Aguilar, and C. Fernandez-Pineda. Thermoosmosis of water through cellulose acetate membranes. *Journal of Membrane Science*, 4:209–219, 1978.
- [46] J. Mengual and F. Garcia-Lopez. Thermoosmosis of water, methanol, and ethanol through cellulose acetate membranes. *Journal of colloid and interface science*, 125(2):667–678, 1988.
- [47] F. Müller-Plathe. A simple nonequilibrium molecular dynamics method for calculating the thermal conductivity. *The Journal of chemical physics*, 106(14):6082–6085, 1997.
- [48] M. Nijmeijer, A. Bakker, C. Bruin, and J. Sikkenk. A molecular dynamics simulation of the lennard-jones liquid–vapor interface. *The Journal of chemical physics*, 89(6):3789–3792, 1988.
- [49] S. Nosé. A molecular dynamics method for simulations in the canonical ensemble. *Molecular physics*, 52(2):255–268, 1984.
- [50] D. Oliver. Effects of thermal osmosis near a buried isolated heat sphere. *International communications in heat and mass transfer*, 13(3):295–304, 1986.

- [51] S. Ono and S. Kondo. Molecular theory of surface tension in liquids. In *Structure of Liquids/Struktur der Flüssigkeiten*, pages 134–280. Springer, 1960.
- [52] R. Piazza. 'thermal forces': colloids in temperature gradients. *J. Phys. Condens. Matter*, 16(38):S4195, 2004.
- [53] R. Piazza and A. Guarino. Soret effect in interacting micellar solutions. *Physical review letters*, 88(20):208302, 2002.
- [54] R. Piazza and A. Parola. Thermophoresis in colloidal suspensions. *J. Phys. Condens. Matter*, 20:153102, 2008.
- [55] S. Plimpton. Fast parallel algorithms for short-range molecular dynamics. *J. Comput. Phys.*, 117:1–19, 1995.
- [56] S. A. Putnam and D. G. Cahill. Transport of nanoscale latex spheres in a temperature gradient. *Langmuir*, 21(12):5317–5323, 2005.
- [57] R. Rastogi, R. Blokhra, and R. Agarwal. Cross-phenomenological coefficients. part 1.studies on thermo-osmosis. *Transactions of the Faraday Society*, 60:1386–1390, 1964.
- [58] R. Rastogi and K. Singh. Cross-phenomenological coefficients. part 5.thermo-osmosis of liquids through cellophane membrane. *Transactions of the Faraday Society*, 62:1754–1761, 1966.
- [59] R. Rastogi, K. Singh, and B. Misra. Thermo-osmosis and electro-osmosis of water and electrophoresis of suspensions in water. *Desalination*, 3(1):32–36, 1967.
- [60] P. Reineck, C. J. Wienken, and D. Braun. Thermophoresis of single stranded dna. *Electrophoresis*, 31(2):279–286, 2010.
- [61] D. Reith and F. Müller-Plathe. On the nature of thermal diffusion in binary lennard-jones liquids. *J. Chem. Phys*, 112(5):2436–2443, 2000.
- [62] F. Römer, Z. Wang, S. Wiegand, and F. Bresme. Alkali halide solutions under thermal gradients: Soret coefficients and heat transfer mechanisms. *J. Phys. Chem. B*, 117(27):8209–8222, 2013.
- [63] J. Rowlinson and B. Widom. *Molecular Theory of Capillarity*. Dover Publications, 2003.

- [64] E. Ruckenstein. Can phoretic motions be treated as interfacial tension gradient driven phenomena? *Journal of Colloid and Interface Science*, 83(1):77–81, 1981.
- [65] P. Schofield and J. Henderson. Statistical mechanics of inhomogeneous fluids. *Proc. R. Soc. A*, 379:231–246, 1982.
- [66] R. Srivastava and P. Avasthi. Non-equilibrium thermodynamics of thermo-osmosis of water through kaolinite. *Journal of Hydrology*, 24(1-2):111–120, 1975.
- [67] J. Trémosa, J. Gonçalvès, J. Matray, and S. Violette. Estimating thermo-osmotic coefficients in clay-rocks: Ii. in situ experimental approach. *Journal of colloid and interface science*, 342(1):175–184, 2010.
- [68] M. Tuckerman. *Statistical mechanics: theory and molecular simulation*. Oxford University Press, 2010.
- [69] H. Vink and S. Chishti. Thermal osmosis in liquids. *Journal of Membrane Science*, 1:149–164, 1976.
- [70] J. Walton, D. Tildesley, J. Rowlinson, and J. Henderson. The pressure tensor at the planar surface of a liquid. *Mol. Phys.*, 48:1357–1368, 1983.
- [71] J. Weeks, D. Chandler, and H. Andersen. Role of repulsive forces in determining the equilibrium structure of simple liquids. *J. Chem. Phys*, 54:5237–5247, 1971.
- [72] S. Wiegand. Thermal diffusion in liquid mixtures and polymer solutions. *Journal of Physics: Condensed Matter*, 16(10):R357, 2004.
- [73] P. Wirnsberger, D. Frenkel, and C. Dellago. An enhanced version of the heat exchange algorithm with excellent energy conservation properties. *The Journal of chemical physics*, 143(12):124104, 2015.
- [74] A. Würger. Thermophoresis in colloidal suspensions driven by marangoni forces. *Physical review letters*, 98(13):138301, 2007.
- [75] A. Würger. Thermal non-equilibrium transport in colloids. *Rep. Prog. Phys.*, 73:126601, 2010.